FRACTURE FAILURE OF SOLID OXIDE FUEL CELLS

A Thesis

Presented to

The Academic Faculty

By

Janine B Johnson

In Partial Fulfillment

of the Requirements for the Degree

Master's of Science in the

School of Mechanical Engineering

Georgia Institute of Technology

November, 2004

FRACTURE FAILURE OF SOLID OXIDE FUEL CELLS

Approved by:

Dr. Jianmin Qu, Advisor

Dr. Andrei Fedorov

Dr. Samuel Graham

November 10, 2004

For Grandpa

ACKNOWLEDGEMENTS

I would like to thank Brian Gardner and Brian Koeppel for their help with curvilinear coordinates and FEM software, respectively.

In addition, my thanks goes to Dr. Mike Gosz in his kind correspondence and help.

The research could not have been done and would have much less interesting without all the students and researchers involved in the fuel cell design project.

Thanks for the constructive comments of my committee advisors, Dr. Andrei Fedorov and Dr. Samuel Graham. It is much appreciated.

Finally, I would like to acknowledge the support of my academic advisor, Dr. Jianmin Qu, without his help none of this would have materialized.

TABLE OF CONTENTS

LIST OF TABLES

LIST OF FIGURES

SUMMARY

A future solution to meet societies' growing energy needs is fuel cells. A fuel cell uses electrochemical interactions to produce electricity. Among all existing fuel cell technologies, the planar solid oxide fuel cell (SOFC) is the most promising one for high power density applications. A planar SOFC consists of two porous ceramic layers (the anode and cathode) through which flows the fuel and oxidant. These ceramic layers are bonded to a solid electrolyte layer to form a tri-layer structure called PEN (positive-electrolyte-negative) across which the electrochemical reactions take place to generate electricity.

Because SOFCs operate at a relatively high temperature, the cell components (e.g., PEN and seals) are subjected to harsh environments and severe thermomechanical residual stresses. It has been reported repeatedly by the SOFC industries that, under combined thermomechanical, electrical and chemical driving forces, catastrophic failure often occurs suddenly due to material fracture or loss of adhesion at the material interfaces. Unfortunately, there have been very few thermomechanical modeling techniques that can be used for assessing the reliability and durability of SOFCs. It is perceivable that for future SOFC systems, with high specific power and low weight, such thermomechanical failure can only be exuberated. Therefore, modeling techniques and simulation tools applicable to SOFC will need to be developed. Such techniques and tools enable us to analyze new cell designs, evaluate the performance of new materials, virtually simulate new stack configurations, as well as to assess the reliability and durability of stacks in operation.

As part of the overall effort in the development of modeling and simulation tools, this thesis research focuses on developing computational techniques for modeling

fracture failure in SOFCs. The objectives are (1) to investigate the failure modes and failure mechanisms due to fracture in SOFCs, and (2) to develop a finite element based computational method to analyze and simulate fracture and crack growth in SOFCs.

By using the commercial finite element software, ANSYS, as the basic computational tool, a MatLab based program has been developed. This MatLab program takes the displacement solutions from ANSYS as input to compute fracture mechanics parameters for a given crack. The individual stress intensity factors are obtained by using the domain (volume) integrals in conjunction with the interaction integral technique. The software code developed here is the first of its kind capable of calculating stress intensity factors for three-dimensional cracks of curved front experiencing both mechanical and non-uniform temperature loading conditions. It is believed that the results of this research provide us with new scientific and engineering knowledge on SOFC failure, and enable us to analyze the performance, operations, and life characteristics of SOFCs.

CHAPTER 1. INTRODUCTION

Fuel cells are a developing technology used to generate electrical energy from a chemical process. A fuel cell consists of an anode (positive electrode)-electrolyte-cathode (negative electrode) interface. Fuel flowing through the anode interacts with an oxidant, which is concurrently moving through the cathode, generating an electrochemical reaction. Several characteristics make fuel cells valuable, such as nearly zero emissions, zero dependence of size on efficiency, and fuel reformation which allows a variety of fuels to be used. The solid oxide fuel cell (SOFC) is a high temperature fuel cell and the term solid oxide refers to the solid laminate serving as the electrolyte.

Currently fuel cell technology is hindered by high cost and related manufacturing difficulties. This is compounded by uncertain mechanical reliability over the cell lifetime. SOFCs typically operate at temperatures above 600ºC and significant residual stresses are generated, due to thermal mismatch in cell materials. Such residual stresses become even more severe during start-ups and shut-downs where a cell transitions from room temperature to operating temperature or vice versa. Other sources of failure include gas leaks caused by the failure of external seals and the increased mismatch between layers as the cell is stacked. Thermal cycling and cell geometry also create nonuniform stress fields within the stack leading to further mechanical degradation. As a consequence, current SOFCs can encounter catastrophic failure during operation and lifetime prediction is difficult.

The research presented here developed methods to analyze the fracture process within SOFCs. The objective was to create tools that can be implemented by industry to facilitate design during the initial phases. This is done by study of failure modes and

failure mechanisms due to fracture in SOFCs, and the development of a finite element based computational method to analyze and simulate fracture and crack growth in SOFCs.

First, the manufacturing process of SOFCs was examined using analytical methods in one-dimensional models. Then, the analysis was extended to a two-dimensional finite element model to establish different design parameters. Lastly, three dimensional codes were developed to analyze fracture within the cell under non-uniform stresses. The thesis is organized as follows.

Chapter Two provides background information on fuel cells. The materials, operating parameters, and failure mechanisms of SOFCs are discussed. Chapter Three describes the theory of fracture mechanics used to study SOFCs. Fracture terminologies are introduced and a broad examination is made of general fracture properties, volume integrals used in finite element analysis, and interfacial fracture.

Chapters Four and Five specifically address the first objective, which is to investigate the failure modes and failure mechanisms due to fracture in SOFCs. Chapter Three introduces optimization techniques using a one-dimensional (1-D) model of the electrolyte and anode layers formed during manufacture. The analysis provides graphs and equations that can be used in design optimization of the electrolyte height. The differences between edge and blister delamination were also examined analytically. These analyses can be applied directly to PEN manufacture.

Chapter Five expands the 1-D model to a two-dimensional (2-D) fracture model which was used to study the behavior of edge delamination and cracks propagating in the anode. This chapter also introduces the use of finite element software to model fracture in SOFCs.

The next chapter focuses on three-dimensional (3-D) modeling of the behavior of the fuel cell and is part of both objectives. The first section introduces the global—local

modeling technique which could be used to simplify the process of modeling 3-D fractures. Methods to include the thermal behavior of the fuel cell in the determination of fracture parameters are discussed. Then, three dimensional fracture is analyzed using volume integrals that incorporate a path-independent energy balance. Finally, these techniques are applied to finite element models and numerical results are obtained for several fracture modes. Ultimately a post processing routine is developed and demonstrated that uses the finite element solution from existing FEM software to calculate fracture parameters. This meets the requirements of objective two to develop a computational method to study cracking in SOFCs.

The last chapter summarizes the importance and interdependence of all these methods presented in this study. It sites the results and conclusions that can be drawn from this work and relates them to useful conclusions about SOFC behavior. By fulfilling the two objectives outlined: (1) study of SOFC failure mechanisms and (2) development of computational methods to study cracking in SOFCs, the study of SOFC structural failure can be used to enhance future development of solid oxide fuel cells.

CHAPTER 2. FUEL CELL BACKGROUND

Technological companies are searching for fast, efficient, and environmentally friendly power sources to meet societies' growing demands. Solid oxide fuel cells (SOFCs), which use chemical reactions to generate electricity, are significant because of benefits like high efficiency and low environmental intrusion. However, these benefits are offset by disadvantages, such as high start up costs and unreliable long-term mechanical stability. To understand the impact of these issues a basic understanding of fuel cell operation is needed.

2.1. The Basic Fuel Cell

A fuel cell consists of an anode-electrolyte-cathode interface, in which fuels flow through a porous anode and react to an oxidant flowing through the cathode. A simple schematic of the electrochemical process is shown in Figure 2.1. The anode-electrolyte-cathode interface is often referred to as the positive-electrolyte-negative (PEN) layer. The reaction in the PEN generates the electrical energy harnessed for different applications. The lack of mechanical parts suggests that fuel cells are theoretically capable of producing energy as long as the necessary fuel and oxidants are present.

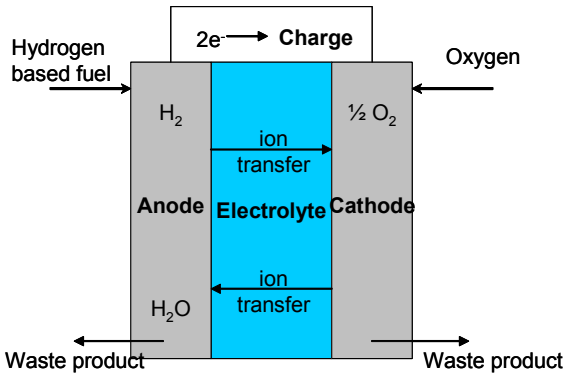

Figure 2.1: Fuel Cell Schematic

The “solid” in SOFCs refers to the solid electrolyte used to obtain the electrochemical reaction, rather than the liquid electrolyte used in some applications. Two configurations of SOFCs exist: tubular and planar. Tubular cells are more common in production, but due to inherent design limitations, upcoming research is shifting to planar cells. The planar fuel cell configuration has benefits such as simplified electrical connections, concealed electrodes, and high power density (EG&G Services 2000). The planar SOFC consists of repeated layers of the PEN alternating with electrical interconnects. The stacked configuration increases power output by creating a series connection between the repeated layers. A picture of the PEN and interconnect is shown Figure 2.2.

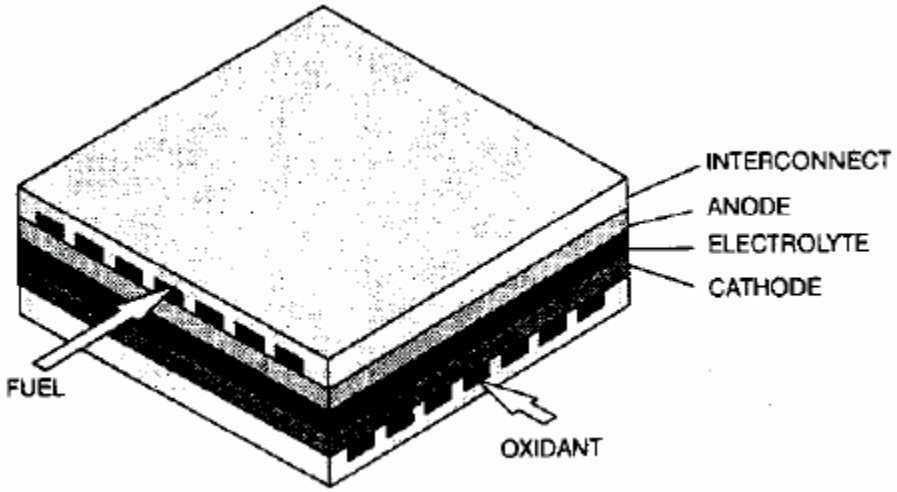

Figure 2.2: Planar SOFC Configuration (EG&G Services 2000)

Thin film technology has been applied to the cell components to reduce size and increase power performance. To counteract the extremely thin films now appearing in electrolytes, the PEN structure has shifted from electrolyte supported to anode-supported structures. Due to lowered resistance these cells can operate at

temperatures of 600˚C-800˚C. Cells with thicker electrolytes, and therefore higher resistance, typically operate at temperatures above 1000˚C (EG&G Services 2000).

Components of the planar configuration must be chemically stable in the fuel cell environment, they must exhibit high conductivity for increased power generation, and they must have thermomechanical compatibility to reduce structural stresses during operation. A typical problem is due to the differences in thermal expansion coefficients of the PEN materials. This problem is enhanced as the structural requirements of the cell increase due to multiple stacks and sealing requirements. Therefore improved SOFC performance requires understanding of thermal mismatch and the structural behavior under thermal loadings.

2.2. Electrodes

The electrodes (anode and cathode) are critical to fuel cell performance for several reasons. Not only do they provide a site where the electrochemical reactions can take place, but they also provide a conduction path away from the electrolyte (EG&G Services 2000).

The anode and cathode are porous ceramics, often composed of Ni-Y_2O_3 stabilized ZrO_2 skeleton and doped lanthanum manganite, respectively. Yttria stabilized zirconia (YSZ) is added to the anode composition to increase matching of the thermal expansion coefficient (TEC) to the electrolyte. Material porosity can vary from 20-40% to allow efficient mass transport. Several methods are used to manufacture the electrodes: slurry method, screen printing, or plasma spraying (EG&G Services 2000).

In anode-supported configurations the anode is significantly larger than the electrolyte layer and the two layers are often created by co-firing at 1400˚C -1500˚C. Due to the TEC mismatch large residual stresses can be produced after cooling, leading

to delamination failures or other cracking. Previous finite element research of fuel cells predicted residual stresses of up to 650 to 720 MPa (Yakabe, Baba et al. 2001).

The doped lanthanum manganite materials used in the cathode layers are also added to the electrolyte by co-firing at high temperatures. The cathode materials can be manufactured to a closer match to the TEC of the electrolytes, but problems still arise due to high temperatures and differences in strength.

2.3. Electrolytes

It is across the electrolyte that the conduction of oxygen ions will take place generating the electricity. The electrolyte is the least conductive material in the PEN structure; one reason why thin film technology is utilized to minimize ohmic losses thereby increasing power performance. These thin laminates must be free of porosity to prohibit gas from spreading to one side or the other. Additionally, each electrolyte must be capable of withstanding not only assembly stresses and structural stresses, but must also be mechanically stable during operation.

Electrolytes are commonly made from zirconia, because of the wide range of ionic conductivity for oxidants. A typical electrolyte composition consists of cubic zirconia stabilized with 8-10 mol% Y_2O_3 (EG&G Services 2000). In anode supported fuel cells typical electrolyte films range from 5μm to 50μm and are manufactured by tape casting and co-firing onto the anode layer.

The sintering of the cathode and anode layers onto the electrolyte directly influences cell performance. Residual stresses will be induced by thermal mismatch and material diffusion during the sintering process. Sintering time and temperature will also change interfacial fracture toughness and material defects such a microcracking caused by residual stresses (Kumar and Sorensen 2002).

2.4. Additional Components

The interconnect is a metal structure that separates each layer of the stack, while also connecting the PEN layers electrically (EG&G Services 2000). It also separates the fuels and oxidants in their adjacent cells. Typically lanthanum chromite is used, but research is also looking at metal alloys such as stainless steal or Inconnel 600.

Sealing between the stacks needs to be thermally and structurally stable. Seals between the stacks, serve several functions, such as preventing external gas leaks, and mixing between the oxidants and fuels, and they must also be electrically insulating. Common seal types are glass seals, brazed, and compressive types.

2.5. Operating Conditions

Operating conditions of solid oxide fuel cells consist of three stages: start-up, steady-state, and shut-down. Initially, during start-up the cell is heated from room temperature to the final operating temperature, many manufacturers send preheated air through the cathode during start up to reduce the chances of thermal shock. Steady state operation occurs after the cell reaches its operation temperature, ranging from approximately 800˚C-1000˚C for anode supported fuel cells. The operating temperature is influenced by several factors such as electrolyte size (thinner electrolytes can lead to lower operating temperatures) and the direction of fuel flow. During steady state operation stresses in the cell are due to the temperature gradient of the electrochemical reaction and to constraints of the structure. When the cell is cooled during shut-down TEC mismatch can once again be a significant cause of internal stresses between components.

2.6. Failure Mechanisms

Experiments by Cai, Green and Messing (1997) examined the effects of constrained densification on Al_2O_3/ZrO_2 laminates fabricated by tape casting and sintering. They found that three types of cracking occurred: channeling in the tensile layer, edge effect cracks, delamination or interface cracking, and cracks parallel to the interface in the compressive layer. These are also failure types that can be found in failed fuel cells.

A study specific to fuel cells found that for 8mol% yttria stabilized zirconia (YSZ) a room temperature flexure failure test was dependant on surface flaws with fracture initiating at porous defects. However, at higher temperatures fracture would also occur at featureless sites. Overall the increase in temperature caused a 23-30% reduction in flexural strength (Lowrie 2000). Experiments on ceramic layers (Ni/YSZ-YSZ-$LaMnO_3$) under thermal shock loading found the dominant failure modes to be transgranular fracture at locations of high thermal gradients and intergranular at high temperature regions. Actual failure was due to cracking normal to the planes but interfacial cracking was also present (Busso, Tkach et al. 2001).

Studies of production techniques found lower strengths for electrolyte-anode layers when sintered at higher temperatures and speculation attributed the cause was due to higher interfacial fracture toughness deflecting cracking through the layers (Sorensen and Primdahl 1998). In creating a constitutive model for co-sintering of fuel cell structures Busso predicts that at sintering temperatures above 1300˚C more stress relaxation will take place, but creep could become a factor at higher temperatures. Residual stresses are considered to be relaxed during sintering due to stress relaxation and microcracking (Busso, Travis et al. 1998). However, all of these SOFC studies

examined electrolyte supported structures featuring electrolytes ranging from 150μm to 200μm.

Limited studies have been done on the fracture toughness of fuel cell materials. Recently, a study found that the fracture toughness for crack initiation is increased in the electrolyte after sintering with electrodes. This study did not take into account stresses due to TEC mismatch but only changes brought about by diffusion processes during sintering (Kumar and Sorensen 2002).

2.7. Finite Element Modeling

In a 1997 article Selcuk noted that previous fuel cell development had focused on enhancement of the electrochemical process, while neglecting the mechanical properties of the materials. In past years steps have been taken to remedy this by increased effort to study individual components such as electrodes and seals; however development of the larger picture of fuel cell behavior is still limited.

Yakabe has done several finite element models to study SOFC behavior. A three dimensional model was created to examine the structural stresses caused by a predetermined thermal field and no mechanical loads. It was discovered that the center cell in a 10 stack model was thermally adiabatic (Yakabe 2001). The model included reformation and gas diffusion, but no constraint conditions were added to the model. Three dimensional simulations are difficult to create due to the complex stresses created by thermal mismatch and the rigidity introduced by the non-conducting seals (Yakabe 2001). Research at Pacific Northwest National Laboratory used coupled analyses of thermal/flow and stress to study solid oxide fuel cells (Recknagle, Williford et al. 2003).

CHAPTER 3. FRACTURE BACKGROUND

3.1. Fracture Types in PEN Layer

Figure 3.1 shows the various flaw types that can occur in the PEN structure. These cracks can be pre-existing defects formed during manufacture or could be initiated during operation. Traditional fracture mechanics is needed to understand substrate cracking such as type **H**, while interfacial mechanics is needed to understand failure types such as **C, F,** and **G.**

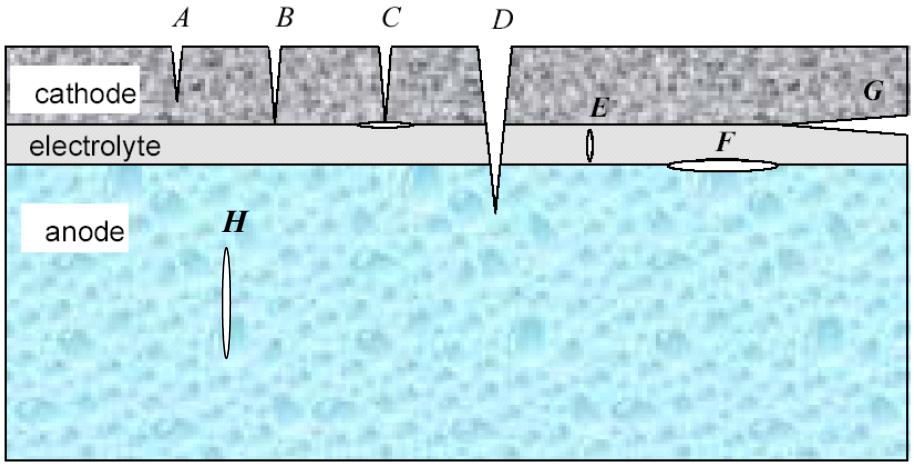

Figure 3.1: Various flaws within PEN structure

The effect of fracture on operation of the fuel cell will depend on the location and type of fracture. Delamination of the electrolyte, such as **F** and **G**, will decrease the active area of electrochemical reactions decreasing power output. While the crack **D**, can obviously cause intermixing of the fuel and the oxidant, other cracks can lead to this possibility. For instance, the anode fracture, **H**, could grow into and through the

electrolyte layer leading to fuel and oxidant mixing. Therefore fracture mechanics is fundamental to accurate study of fuel cells.

3.2. Fracture Mechanics

The study of crack growth in materials is characterized by two different fracture parameters; an energy based parameter and a stress intensity approach (Anderson 1995). For both methods, fracture is characterized by a crack length (a). Figure 3.2 defines the crack length for a crack fully within a body or at the body's edge. The fracture parameters will vary depending on the loading conditions and the body configuration. Once the fracture parameter is calculated it can be compared to the material's resistance to crack growth to determine if the crack will grow.

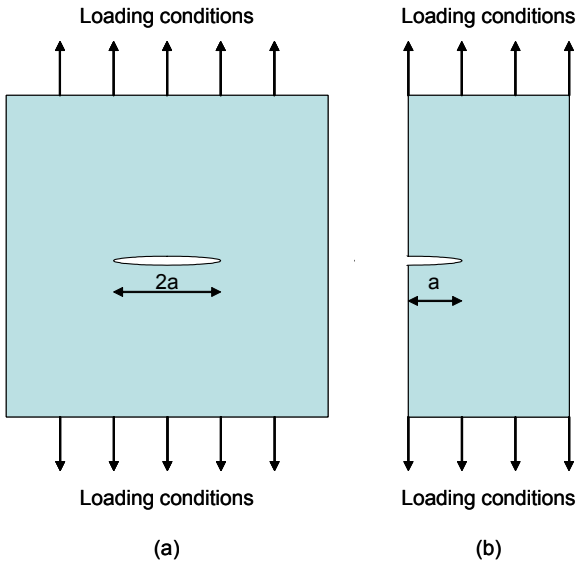

Figure 3.2: Examples of (a) fracture within a body and (b) fracture at the edge of a body

Section 3.2.1 will introduce the energy based parameter and describe the conditions required for crack growth. Section 3.2.2 covers the stress intensity approach. After these parameters are introduced, other fracture concepts will be reviewed; such as

interfacial fracture and the use of volume integrals to calculate fracture parameters. This fracture review will be confined to linear elastic materials.

3.2.1. Energy Release Rate

An energy based parameter, energy release rate (G), is defined as the energy required for crack growth. This parameter assumes that a crack increases when the energy available for crack extension overcomes the inherent resistance of the material. Equation (3.1) is a mathematical interpretation of this value, where $d\pi$ is the change of potential energy in the system with respect to the differential crack growth (da) (Anderson 1995).

$$G = -\frac{d\pi}{da} \tag{3.1}$$

A material's resistance to crack growth is an intrinsic material property termed fracture toughness (G_c). Determination of the fracture toughness requires experimental testing, but once it is characterized the following relationship is used to predict crack growth.

If $G \geq G_c$, then the crack will extend. (3.2)

3.2.2. Stress Intensity Factors

While the energy release rate can predict crack growth it does not allow for the definition of the stress fields near the crack tip. Stresses near the crack tip will be extremely high as shown in Figure 3.3, or mathematically a stress singularity will occur at the tip of the crack (Anderson 1995). Characterization of this stress intensity can be used to completely define the stresses occurring near the crack tip.

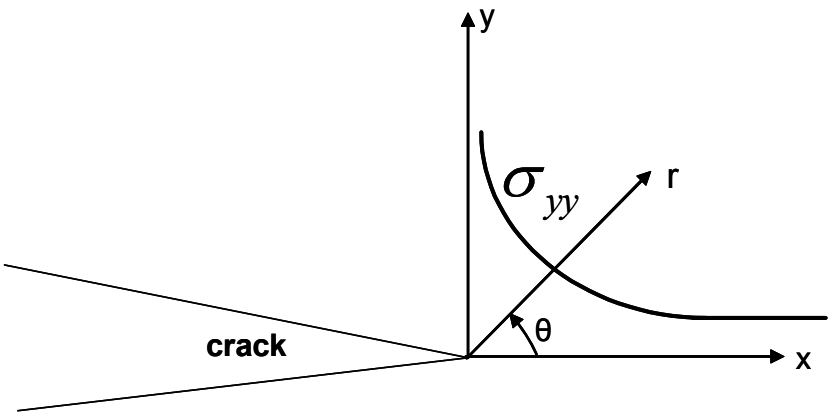

Figure 3.3: Stress Singularity at Crack Tip (General Example)

The stress intensity factor is a constant that is proportional to the stresses occurring near the crack tip. The parameter is important because it can be separated into loading modes designating opening (K_I), in-plane shear (K_{II}), and out of plane shear (K_{III}) (Anderson 1995). These different loading modes are shown below.

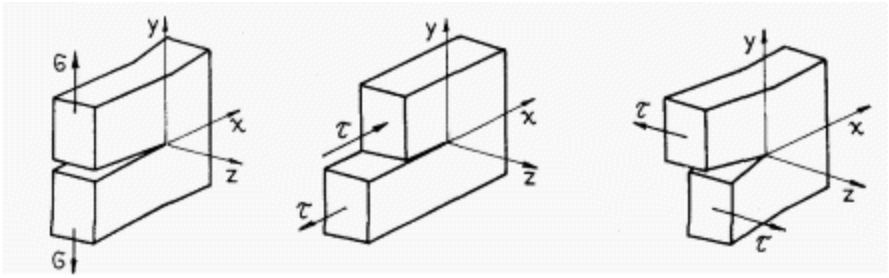

Figure 3.4: Different loading modes and the related the stress intensity parameters.

These parameters can be used to write the field equations for the stress and displacement fields for different loading configurations, but analytical solutions are not

easily available for complex configurations. Therefore the stress intensity factors often need to be calculated numerically for each set of given boundary conditions and applied loads. A general example of the relationship between stress and the stress intensity is shown in (3.3).

$$\sigma_{ij} = \frac{K_I}{\sqrt{2\pi r}} f_{ij}^{(I)}(\theta) + \frac{K_{II}}{\sqrt{2\pi r}} f_{ij}^{(II)}(\theta) + \frac{K_{III}}{\sqrt{2\pi r}} f_{ij}^{(III)}(\theta), \text{ where} \tag{3.3}$$

$$\begin{aligned} &\sigma_{ij} = \text{stress tensor} \\ &f_{ij}^{(Mode)} = \text{function corresponding to mode I, II, or III} \\ &r = \text{radius from cracktip} \\ &\theta = \text{angle from crack plane} \end{aligned} \tag{3.4}$$

Figure 3.3 shows the relationship between the polar coordinates (r, θ) and the crack tip coordinate system.

3.2.3. Relationship between Stress Intensity and Energy Release Rate

The energy release rate and the stress intensity factors are related to each other as shown below:

$$G = \frac{K_I^2 + K_{II}^2}{E'} + \frac{K_{III}^2}{2\mu} \tag{3.5}$$

The Young's modulus (E) and shear modulus (μ) are defined in (3.6).

$$\begin{aligned} &E' = E \text{ plane stress} \\ &E' = \frac{E}{1-\nu^2} \text{ for plane strain} \\ &\mu = \frac{E'}{2(1+\nu)} \end{aligned} \tag{3.6}$$

3.3. Interfacial Fracture

Cracking at the interface can be significant for several reasons and can directly affect performance of the fuel cell. For example, an area of delamination between the electrolyte and anode reduces the active area of the electrochemical reaction, decreasing power output. An example of interfacial cracking is shown in Figure 3.5.

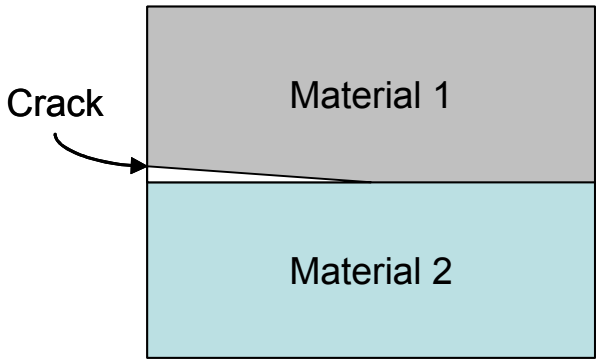

Figure 3.5: Example of interfacial cracking or a delamination at the interface

While interfacial cracking can also be characterized by energy release rate and the stress intensity factors, its study is complicated by the oscillatory behavior of the crack tip singularity. Rice et al., in 1990, successfully used complex stress intensity factors to parameterize interfacial fracture (Rice, Suo et al. 1990). And Hutchinson and Sou in a paper titled “Mixed Mode Cracking in Layered Materials” performed a detailed overview of interfacial fracture mechanics (1992). Properties of buckle driven delamination of thin films and the interfacial fracture of isotropic materials were also discussed.

Earlier studies of interface fracture had connected the phase angle of loading (ratio of shear to opening) to the crack path selection at interfaces (Evans, Drory et al. 1988). Additionally, He and Hutchinson examined interfacial fracture to determine if a crack will

continue to propagate through the interface or rather kink out and propagate through the substrates (He, Bartlett et al. 1991). In a following paper He introduced an approach that allowed the direction of crack growth to be determined by the ratio of the various energy release rates (2000). Finally, the delamination of thin films and the occurrence of buckling were studied by He and Evans (1998).

3.3.1. Bimaterial Constants

Elastic material parameters are needed to study bimaterial cracks. The Dunder's parameters (α, β) characterize elastic mismatch for isotropic solids, where $k_i = 3 - 4v_i$ for plane strain and $k_i = (3 - v_i)/(1 + v_i)$ for plane stress, where *i* designates the material number.

$$\alpha = \frac{\mu_1(\kappa_2 + 1) - \mu_2(\kappa_1 + 1)}{\mu_1(\kappa_2 + 1) + \mu_2(\kappa_1 + 1)}$$
$$\beta = \frac{\mu_1(\kappa_2 - 1) - \mu_2(\kappa_1 - 1)}{\mu_1(\kappa_2 + 1) + \mu_2(\kappa_1 + 1)} \tag{3.7}$$

The values of α and β approach zero as the difference between the moduli decrease. If one material is much stiffer the values of constants approach ±1 depending on the material labeling (Hutchinson and Suo 1992).

The bimaterial constant (ε) is based on the Dunder's constants as is defined in equation (3.7). The bimaterial constant is sometimes referred to as the oscillation index because the size relates to the behavior of the complex stress intensity factor ($\mathbf{K} = K_I + iK_{II}$) used by Rice and Sou (1990).

$$\varepsilon = \frac{1}{2\pi} \ln\left(\frac{1-\beta}{1+\beta}\right) \tag{3.8}$$

3.3.2. *Complex Stress Intensity Factor*

The stress fields at the crack tip can be written as a function of the intensity factors if the bimaterial constant is used as an oscillation index (Rice, Suo et al. 1990). If the bimaterial constant is zero, which occurs if material one and two are equivalent, the bimaterial stress field in equation (3.9) will reduce to the homogenous form shown in equation (3.3).

$$\sigma_{ij} = \frac{\mathrm{Re}\left[\mathbf{K}L^{i\varepsilon}\right]}{\sqrt{2\pi r}} f_{ij}^{(I)}(\theta,\varepsilon) + \frac{\mathrm{Im}\left[\mathbf{K}L^{i\varepsilon}\right]}{\sqrt{2\pi r}} f_{ij}^{(II)}(\theta,\varepsilon) + \frac{K_{III}}{\sqrt{2\pi r}} f_{ij}^{(III)}(\theta) \tag{3.9}$$

The primary difference between (3.9) and (3.3) is the use of the bimaterial constant and the complex stress intensity factor $(\mathbf{K})$. The complex stress intensity is a function of the K_I and K_{II} introduced in Section 3.2.2. To extract the real and imaginary parts from the complex $\mathbf{K}$ some characteristic length (L) is used.

The complex stress intensity factor is defined and related to a dimensional form in (3.10). The value F is a complex valued function and L is some characteristic length such as crack length (Hutchinson and Suo 1992).

$$\mathbf{K} = K_I + iK_{II} \equiv (\text{applied stress}) \times FL^{1/2-i\varepsilon} \tag{3.10}$$

The energy release rate for interfacial crack problems can now be expressed in the following equation:

$$G = \frac{1}{E^*} \frac{\mathbf{K}\overline{\mathbf{K}}}{\cosh^2(\pi\varepsilon)} + \frac{K_{III}^2}{2\mu^*} \text{ where,} \tag{3.11}$$

$$E^* = \frac{E_1' E_2'}{E_1' + E_2'} \tag{3.12}$$

3.3.3. *Phase Angle*

Even though K_I and K_{II} are now coupled together in a complex form, they can still be used to represent the mode of loading at the crack face. The phase angle of loading can be determined from the following equation.

$$\psi = \tan^{-1}\left[\frac{\mathrm{Im}[\mathbf{K}L^{i\varepsilon}]}{\mathrm{Re}[\mathbf{K}L^{i\varepsilon}]}\right] \tag{3.13}$$

For nonzero values of the bimaterial constant the phase angle is a function of the geometry of the problem, however as $\varepsilon \to 0$ the angle represents the strengths between the K_I and K_{II} stress intensity factors (Nakamura 1991).

3.4. Volume Integrals

The fracture parameters of fuel cells need to be studied using tools easily available to researchers of fuel cells. This leads to the development of finite element models to study both two dimensional and three dimensional fractures. Initially for the 2-D analysis the stress intensity factors and energy release rates were calculated by methods described in the ANSYS 7.1 Fracture Mechanics guide. However, effective analysis of three-dimensional fracture required the use of volume integrals to calculate the energy release rate and the stress intensity factors. The domain integral is used to calculate the energy release rate and the interaction integral is a special form of the domain integral that can be used to extract the stress intensity factors.

In 1985 Li et al. compared methods to calculate the energy release rate by evaluating energy variations within a domain. A method to convert the volume form of the j-integral to a pointwise value is detailed along with the steps to implement a finite element evaluation. The same year DeLorenzi arrived at comparable results and referred to the test function $\mathbf{q}$ as a mapping function to simulate crack growth. His

examination of axisymmetric cracks, such a penny shaped crack, discussed the importance of additional terms to account for hoop stresses (Delorenzi 1985). Shih added thermal strains in the derivation of the domain integral effectively adding a thermodynamic portion to the integral (1986).

In 1991 Nakamura used auxiliary fields to study three dimensional fractures in bimaterial cracks. The article discussed the significance of phase angles in bimaterial cracks and performed a detailed analysis of a 3-D straight bimaterial crack (Nakamura 1991). An emphasis is placed on the bimaterial constant as an oscillatory index and the two different phase angles are used to examine mode mixity. In 1993, Nahta and Moran used a cylindrical coordinate system to allow the interaction integral to be used in curvilinear crack configurations. Gosz, Dolbow, and Moran extended the work further with a curvilinear coordinate system to simplify the interaction integral computation (1998). A detailed postprocessing method is also recorded (Gosz 1998). In 2002, Gosz used the same techniques to study non-planar cracks in homogenous bodies.

3.4.1. Domain Integral (Energy Release Rate)

The domain integral is the volume form of the j-integral, which is a path independent line integral used to calculate the nonlinear energy release rate for elastic-plastic systems discovered by Rice (1968). For an isotropic elastic homogenous material the j-integral is equal to the energy release rate $\left(G\right)$ (Anderson 1995). This fracture parameter is calculated from the tractions, strains, and the strain energy density ($\mathbf{W}$) of the system normal to a path, Γ, as shown in Figure 3.6 and Equation (3.14).

$$J = -\int_{\Gamma}\left(W\delta_{1j} - \sigma_{ij}\frac{\partial u_i}{\partial x_1}\right)n_j d\Gamma \tag{3.14}$$

Equation (3.14) is written in indicial notation. The strain energy density (W) of the system is a scalar quantity that measures the total work per unit volume of the system and δ_{ij} is the Kronecker's delta. The second part of (3.14) consists of the stress fields (σ_{ij}) and the spatial derivatives of the displacement (u_i) surrounding the crack tip. n_j is the vector normal to the path and is illustrated in Figure 3.6.

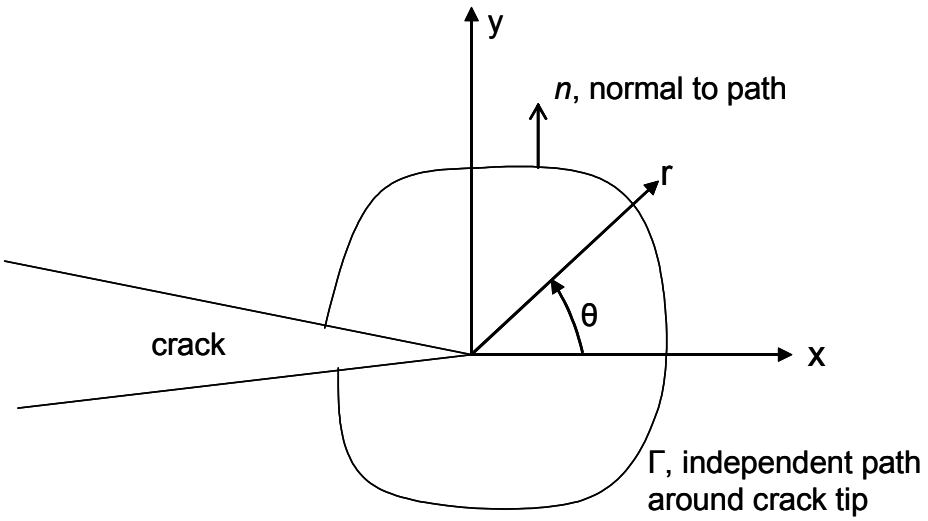

Figure 3.6: Independent path around crack tip

Use of the j-integral for finite element applications is preferred for several reasons. Firstly, it is based on the energy change of the system, and not strictly on calculation of stress or strain fields near the crack tip. This means that the difficult problem of accurately meshing the crack tip is greatly simplified. However, while equation (3.14) is accurate for two dimensional problems, difficulties arise in calculating fracture parameters for three dimensional models. For accurate determination of energy release rates of three dimensional models, it is necessary to convert the line integral to a

volume integral. A complete derivation is provided in reference Li et al. (1985) and is summarized below.

3.4.1.1. Line integral to volume integral

Initially equation (3.14) is rewritten such that a closed contour (S) surrounds the crack tip. This is a three dimensional volume in that the contour also includes a section of the crack length and the crack faces. Then an arbitrary test function $(\mathbf{q})$ is created such that

$$q_j = \begin{cases} l_j \text{ on the crack tip} \\ 0 \text{ on the boundary} \end{cases}, \tag{3.15}$$

where l_j is normal to the crack tip and the test function is continuous between the crack tip and boundary.

The j-integral can now be written as,

$$\overline{G} = -\oint_{\substack{\text{closed} \\ \text{contour}}} P_{jk} q_j n_k dS \tag{3.16}$$

P_{jk} = $\left(W\delta_{kj} - \sigma_{ik} \dfrac{\partial u_i}{\partial x_j} \right)$ is called the energy momentum tensor and consists of the same components in (3.14). The bar over the energy release rate (G) represents that this is the total energy decrease for the crack length surrounded by the contour S.

Application of the divergence theorem provides:

$$\overline{G} = -\int_V P_{jk} \frac{\partial q_j}{\partial x_k} dV \tag{3.17}$$

The V in the integral refers to the volume made by the closed contour. Also $\partial q_j / \partial x_k$ represents the spatial derivatives of the test function defined in (3.15).

The above calculation (3.17) assumes that the crack faces are traction-free, and thermal strains, body forces, and inertia forces are absent. For plane problems the integral is path independent, but for axisymmetric or curved fronts (3.17) is only locally path independent (Nahta 1993). A complete description of this is found in the Nahta 1993 article.

The test function $\left(q_j\right)$ is determined by its value on the boundary and is continuous within the volume. It could be considered as the virtual crack growth. As shown in Figure 3.7, when a crack undergoes growth at a point S, a continuous function can be used to represent the growth for some arc length on the crack tip.

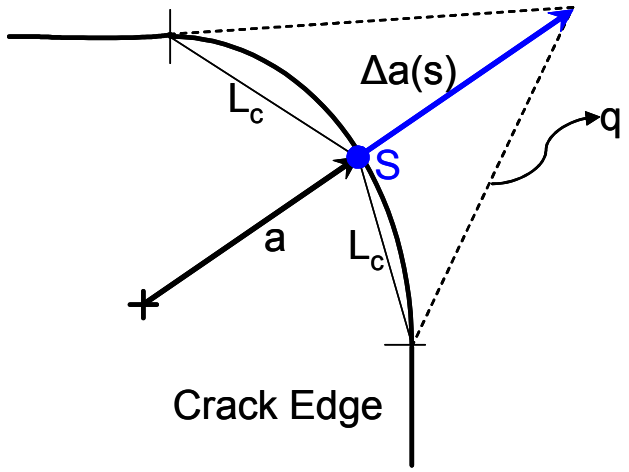

Figure 3.7: Continuous function $\mathbf{q}$ on crack tip

The pointwise value of the energy release rate assumes that for a small chord length (L_c) the integral is the total value for the segment. If the pointwise value is considered constant along the selected chord length then division by the chord length

results in the value at point S as shown in equation (3.18). The unit of the pointwise value of the energy release rate $(G(s))$ is energy over area, while $\overline{G}$ has dimension of energy per length.

$$G(s) = \frac{\overline{G}}{\int_{L_c} \Delta a(s) ds} \tag{3.18}$$

3.4.1.2. Thermal Derivation

When thermal effects are taken into account the domain integral is no longer divergence free. In addition to mechanical strain $\left(\varepsilon_{ij}^{mech}\right)$, a thermal strain $\left(\varepsilon_{ij}^{th}\right)$ will be created from the expansion or contraction of the materials. It is now necessary to introduce a total strain which is equal to the sum of the mechanical and thermal strains.

$$\varepsilon_{ij}^{tot} = \varepsilon_{ij}^{mech} + \varepsilon_{ij}^{th} \text{ , where} \tag{3.19}$$

$$\varepsilon_{ij}^{th} = \alpha\theta\delta_{ij} \tag{3.20}$$

In equation (3.20) α is the thermal expansion coefficient, and θ is the total change in temperature.

Calculation of the strain energy density is modified to specify only mechanical strains, such that

$$W = \int_{\varepsilon_{ij}^{mech}} \sigma_{ij} d\varepsilon_{ij}^{mech} \tag{3.21}$$

Now when the divergence of (3.16) is taken, the effect of thermal variations must be taken into account. The final form now includes a thermal part multiplied by the test function. A detailed derivation is in the 1986 paper by Shih.

$$\overline{G} = -\int_V \left(P_{jk} \frac{\partial q_j}{\partial x_k} + \frac{\partial P_{kj}}{\partial x_k} q_j \right) dV \text{ , where} \tag{3.22}$$

$$\frac{\partial P_{kj}}{\partial x_k} = \alpha \sigma_{ii} \frac{\partial \theta}{\partial x_j} \tag{3.23}$$

3.4.2. Interaction Integral (Stress Intensity Factors)

The interaction integral superimposes an auxiliary solution with a known result to extract the stress intensity factors from the volume integral (Shih and Asaro 1988). Initially, a total energy release rate is calculated that combines the auxiliary field values (usually a known 2-D plane strain solution) and the actual model.

$$G_{total} = -\int_{\Gamma} \left(\frac{1}{2} \left(\sigma_{mn} + \sigma_{mn}^{aux} \right) \left(\varepsilon_{mn} + \varepsilon_{mn}^{aux} \right) \delta_{jk} - \left(\sigma_{ik} + \sigma_{ik}^{aux} \right) \frac{\partial \left(u_i + u_i^{aux} \right)}{\partial x_j} \right) n_k d\Gamma \tag{3.24}$$

The aux subscripts denote the auxiliary stresses, strains, and displacements calculated from analytical equations. Appendix A lists the displacement equations used in calculation of plane strain interface cracks.

The interaction integral is calculated by subtracting the auxiliary and actual energy release rate. The remainder is the interaction of the actual and auxiliary components as shown in equation (3.25). The equation is simplified by using reciprocity which states $\sigma_{ij} \varepsilon_{ij}^{aux} = \sigma_{ij}^{aux} \varepsilon_{ij}$.

$$\begin{aligned} G_{\text{int}} &= G_{total} - G - G_{aux} \\ G_{\text{int}} &= -\int_{\Gamma} P_{jk}^{\text{int}} n_k d\Gamma \end{aligned} \quad \text{, where} \tag{3.25}$$

$$P_{jk}^{\text{int}} = \sigma_{mn} \varepsilon_{mn}^{aux} \delta_{jk} - \sigma_{ik} \frac{\partial u_i^{aux}}{\partial x_j} - \sigma_{ik}^{aux} \frac{\partial u_i}{\partial x_j} \tag{3.26}$$

Following the same procedure as in Section 3.4.1.1 the divergence theorem is applied to the previous equation to create a volumetric form of the interaction integral $\left(\overline{I} \right)$. However, the divergence portion of the momentum tensor cannot be neglected, even

asymptotically, for a curved crack front. The plane strain auxiliary field will violate compatibility for the volume and the integral will no longer be divergence free.

$$\overline{I} = \overline{G}_{\text{int}} = -\int_V \left(P_{jk}^{\text{int}} \frac{\partial q_j}{\partial x_k} + \frac{\partial P_{kj}^{\text{int}}}{\partial x_k} q_j \right) dV \text{ , where} \tag{3.27}$$

$$\frac{\partial P_{kj}^{\text{int}}}{\partial x_k} = \left[\sigma_{mn} \varepsilon_{mn,j}^{aux} - \sigma_{ik} u_{i,jk}^{aux} - \sigma_{ik,k}^{aux} u_{i,j} \right] \tag{3.28}$$

The commas in equation (3.28) indicate a partial derivative with respect to the subscript after the comma. Equation (3.27) and (3.28) do not account for thermal strains, crack face tractions, and inertia forces.

By rewriting the first line of equation (3.25) in terms of stress intensity factors the pointwise value of the interaction integral is used to calculate the unknown stress intensity factors using equation (3.29). The specific stress intensity can be found by setting the corresponding auxiliary value equal to one and letting the other values equal zero, for instance the calculation of K_I is done by setting $K_I = 1$ and $K_{II} = K_{III} = 0$ in equation (3.30).

$$I(s) = \frac{2}{E^* \cosh^2(\pi\varepsilon)} \left[K_I K_I^{aux} + K_{II} K_{II}^{aux} \right] + \frac{1}{\mu^*} K_{III} K_{III}^{aux} \tag{3.29}$$

$$K_I = \frac{I(s)}{2} E^* \cosh^2(\pi\varepsilon) \tag{3.30}$$

CHAPTER 4. ELECTROLYTE DELAMINATION DURING PROCESSING

Section 2.6 discussed the co-firing process in the creation of the anode-electrolyte-cathode layers and the residual stresses created during this process. This manufacturing process makes it necessary to understand the behavior of delamination cracks under a large temperature differential. For instance anode-supported SOFC's can be fabricated at temperatures up to 1500^{o}C (Singhal and Kendall 2002). During the cooling process the compressive stresses generated by thermal mismatch may cause delamination. An example of delamination at the anode-electrolyte interfaces is shown in Figure 3.1. The defect **F** is an example of a blister delamination, while defect **G** is an example of edge delamination.

4.1. Material Constants

Chapter Two briefly discussed material constants common in studying fracture mechanics. The values of these constants are shown in Table 4.1 for the general material properties relating to the PEN layers in SOFCs. The nonzero values of the Dunder's and bimaterial constants characterize the material difference between the two materials. The material properties used are listed in Table 4.2.

Table 4.1: Interfacial fracture properties of anode/electrolyte

Interface	$E^{'}$ **(GPa)**	E^{*} **(GPa)**	β	α	ε
Anode/Electrolyte	220, 106	143	0.10	0.35	0.0321

Table 4.2: Typical material properties of PEN materials

Material	Modulus E (GPa)	Poisson's Ratio v	TEC α (10^{-6}/ºC)
Cathode (LSM+YSZ)	96	0.3	10.56
Electrolyte (YSZ)	200	0.3	10.56
Anode (Ni+YSZ)	96	0.3	12.22

4.2. Blister Delamination

After processing, defects (flaws) may exist along the electrolyte/anode interface. When the flaw size is sufficiently small, local stress fields near the defect are not affected because the electrolyte layer above the flaw remains flat as shown below.

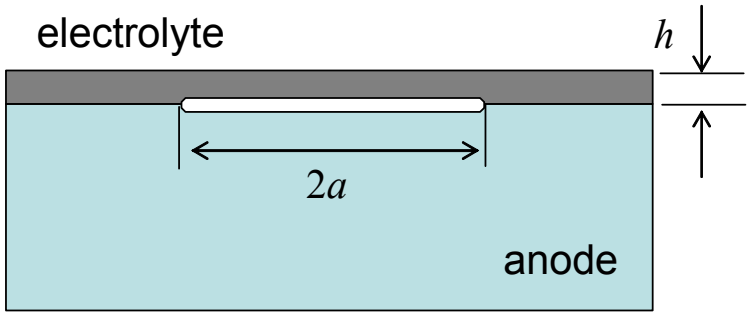

Figure 4.1: Blister Delamination

When the flaw size increases, it may reach a critical length such that the electrolyte layer above the flaw buckles under compressive stresses after sintering, as shown in Figure 4.2. The buckled electrolyte layer generates significant stresses near the edge of the flaw, which may induce further interfacial fracture.

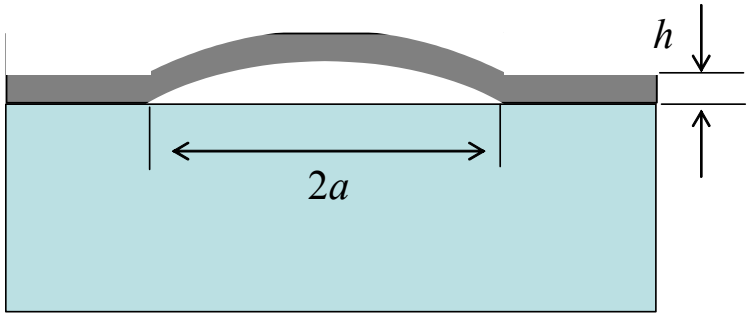

Figure 4.2: Blister crack with buckling

4.2.1. *Thermal Residual Stress*

Based on elasticity theories, the biaxial compressive stress in the electrolyte layer is given by

$$\sigma = \frac{E}{1-v}\Delta T \Delta\alpha \,, \tag{4.1}$$

where E and v are, respectively, the Young's modulus and Poisson's ratio of the electrolyte, ΔT is the temperature differential (in our case, it is the difference between processing and room temperature), $\Delta\alpha$ is the difference in the coefficient of thermal expansion between the electrolyte and anode materials (Shigley and Mischke 1989). It follows from Table 4.2 that

$$\Delta\alpha = 1.66\times 10^{-6}/^{\circ}C\,. \tag{4.2}$$

For processing temperature around 1400^0C, the resulting thermal residual stress, based on (4.1), is 664MPa. This is consistent with the experimental values reported in the literature (Yakabe, Baba et al. 2001).

4.2.2. *Buckling Calculations*

As discussed in “Mixed Mode Cracking of Layered Materials” by Hutchinson and Sou a relationship exists between electrolyte height and the flaw length at which

buckling occurred (1992). The first step to determine critical electrolyte height before buckling occurs requires determination of the flaw size that will initiate buckling. The critical flaw size for buckling can be predicted as follows: assume the initial flaw is a circular delamination of radius a between the electrolyte layer of thickness *h* and a thick anode substrate. The anode layer is treated as a semi-infinite space in order to simplify computations. This assumption introduces little error for anode-supported cells because the thickness of the anode is orders of magnitude larger.

Based on the von Karman nonlinear plate theory, as detailed in Hutchinson and Sou (1992), the critical in-plate compressive stress (σ_c) for buckling of a circular plate of radius a is

$$\sigma_c = 1.2235 \frac{E}{1-v^2}\left(\frac{h}{a}\right)^2, \tag{4.3}$$

where the edges of the circular plate are clamped. By equating (4.1) and (4.3) the dependence between the critical flaw size (a_c) to the processing temperature and the electrolyte layer thickness (h),

$$\Delta T \Delta\alpha = 1.2235 \frac{1}{1+v}\left(\frac{h}{a_c}\right)^2, \tag{4.4}$$

The critical stress and temperature were determined from (4.3) and (4.4) then plotted in Figure 4.3. The chart used top and bottom horizontal axes to plot the processing temperature and the corresponding compressive stress in the electrolyte layer. For example, a processing temperature of 1400^0C corresponds to ~660MPa compressive stress. It is seen from Figure 4.3 that the cells are fairly insensible to processing flaws. For an electrolyte layer of thickness 20μm, the sintered anode-electrolyte layer can tolerate initial flaws of ~700μm in diameter. This indicated that

buckling driven (blister) delamination is unlikely in SOFCs, or at least it may not be a dominant failure mode.

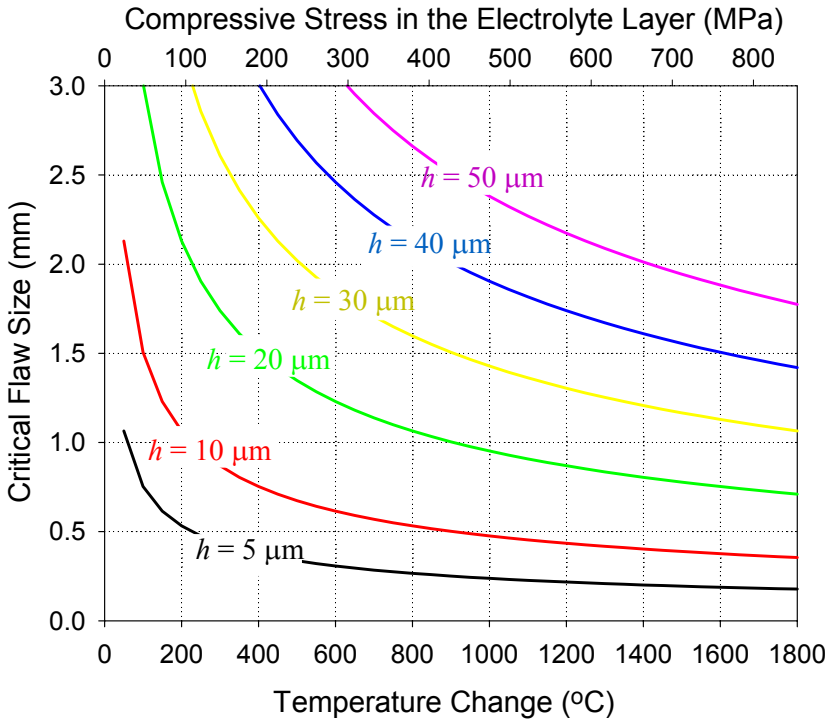

Figure 4.3: Relationship between compressive Stress, flaw size, and temperature change of blister delamination of various electrolyte heights

4.2.3. Energy Release Rate of Blister Delaminations

The propensity for crack growth is determined by calculation of the energy release rate. For the circular blister delamination, the energy release rate is given by

$$G = \frac{(\Delta T \Delta\alpha)^2 Eh}{(1-\upsilon)[1+0.9021(1-\upsilon)]}\left\{1-\left[\frac{1.2235}{\Delta T \Delta\alpha(1+\upsilon)}\left(\frac{h}{a}\right)^2\right]^2\right\} \qquad (4.5)$$

Equation (4.5) gives the relationship among four important parameters, the energy release rate (G), the processing temperature (ΔT), the electrolyte layer

thickness (*h*), and the diameter of the blister delamination (2*a*). Equation (4.5) was derived from (4.4) and information provided in Section 4 in Hutchinson and Sou (1992).

The energy release rate of circular blisters as a function of electrolyte thickness is plotted in Figure 4.4 for different delamination lengths. For a typical sintering temperature ($\Delta T = 1400^0 \mathrm{C}$) the initial flaw of 0.5mm has zero propensity for crack growth for electrolyte thicknesses greater than 25μm.

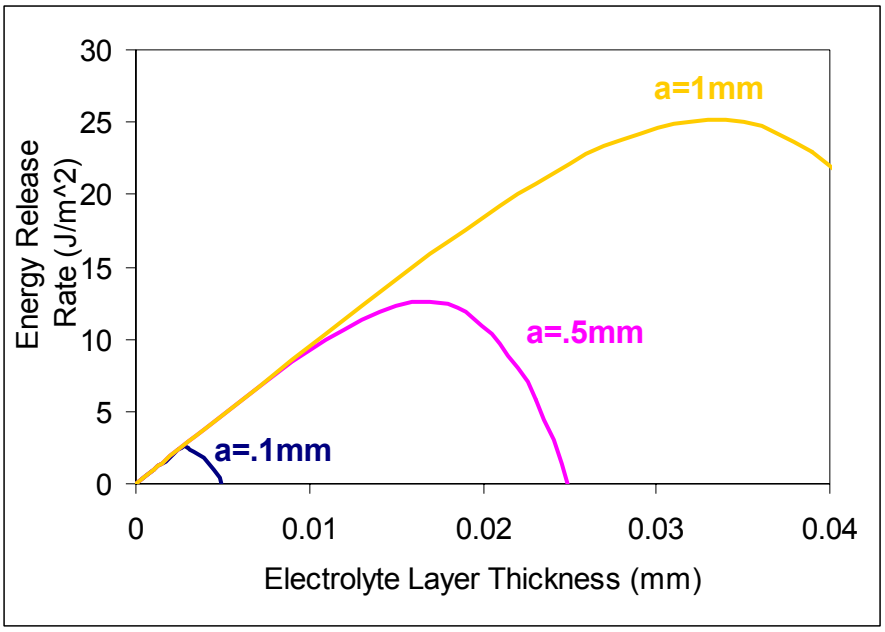

Figure 4.4: Energy release rate of a circular blister delamination vs. electrolyte layer thickness for various initial flaw sizes; Processing Temperature is ΔT =1400˚C

4.3. Edge Delamination

Edge delamination cracks differ from blister delamination in the behavior strain energy. As the tip peals away from the substrate it becomes stress free and releases the stored energy. Quantitatively, the energy release rate due to per unit delamination

growth will equal the strain energy stored in the layer per unit area. The elastic strain energy stored in the electrolyte layer per unit area is

$$\frac{1-v}{E}\sigma^2 h \tag{4.6}$$

Since the energy release rate can be considered equal to the strain energy stored per unit area it can now be calculated from:

$$G = 1.028\frac{1-v}{E}\sigma^2 h, \tag{4.7}$$

where 1.028 accounts for the biaxial stress effect. Substitution of (4.1) into (4.7) yields the energy release rate of the edge delamination when subjected to a temperature change of ΔT,

$$G = \frac{1.028}{(1-v)}(\nabla T \nabla \alpha)^2 Eh \tag{4.8}$$

Clearly, for a given material system and given temperature change, the driving force for delamination is proportional to the electrolyte layer thickness. Thus, thicker electrolyte layers have higher propensity for edge delamination. The critical thickness for delamination is derived from (4.8) by making use of the fracture criterion that for a crack to grow the energy release rate must be greater than the fracture toughness (G_{ic}),

$$h_c = \frac{G_{ic}(1-\upsilon)}{1.028E(\Delta T \Delta\alpha)^2}. \tag{4.9}$$

Recall that G_{ic} is the interfacial fracture toughness, which must be measured experimentally.

Now consider a typical case, where the electrolyte layer thickness is $h = 20\mu\mathrm{m}$, and the processing temperature change is 1400˚C. The corresponding energy release rate for an edge delamination calculated from (4.8) is $G = 31.73\,\mathrm{J/m^2}$. This must be

compared with the measured interfacial fracture toughness to assess the tendency for delamination.

4.4. Comparison between Edge and Blister Delamination

To investigate the propensity of edge delamination over blister delamination, the energy release rate for both failure modes are plotted in Figure 4.5 as a function of initial flaw size for various electrolyte layer thicknesses. The solid lines are for blister delamination and the dashed lines are for the edge delamination. The edge delamination is independent of the initial flaw size, but the energy release rate, or the driving force for fracture, is much higher than that for blister delamination. This further underlines the earlier conclusion that blister delamination is not very likely, or at least not a dominant failure mode.

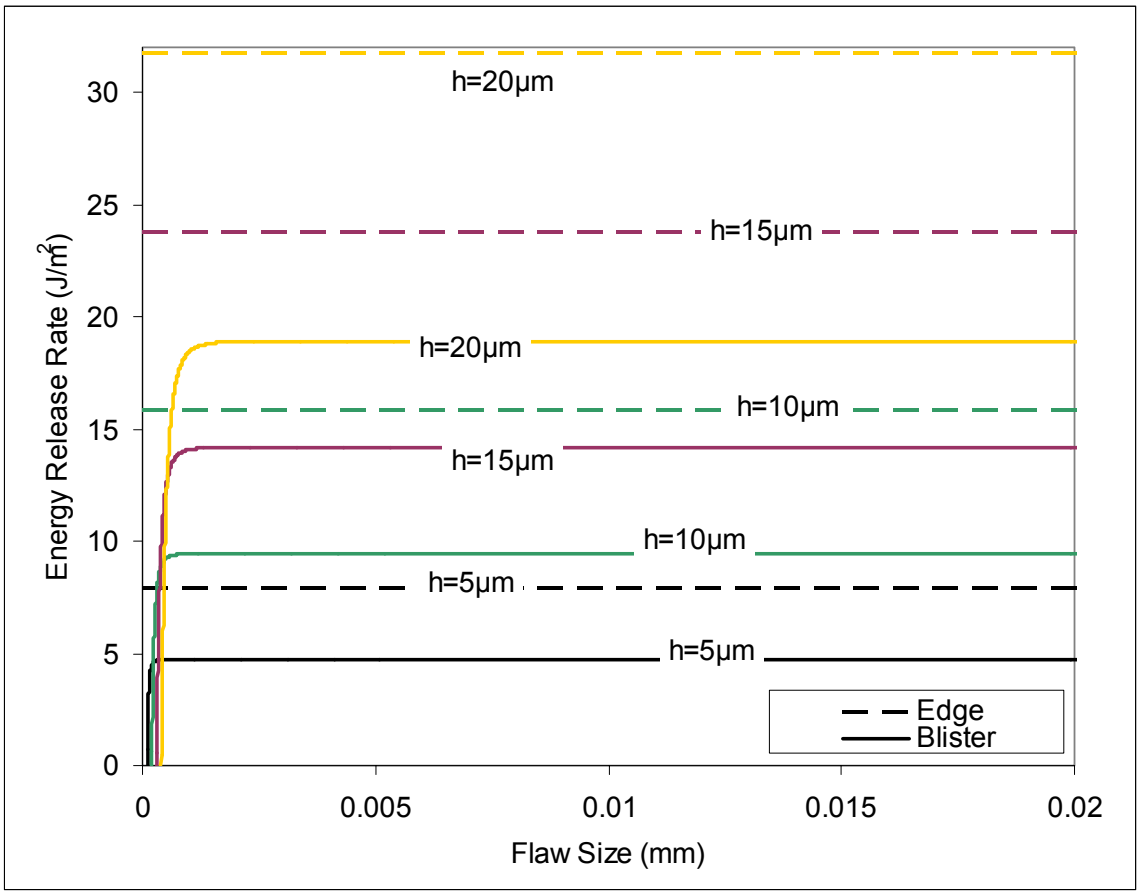

Figure 4.5: Comparison of energy release rate between edge and blister delamination

CHAPTER 5. 2-D FEM FRACTURE OF PEN

Next the PEN was examined under temperature loading without mechanical loading. Initially the stress behavior of the anode-electrolyte-cathode material is examined using a 2-D finite analysis in an unflawed body. Two cracking scenarios were also analyzed using finite element analysis. The first one examined the behavior of a crack placed fully within the anode. Then edge delamination is studied and a criterion to predict the direction of growth is developed.

5.1. Warpage and Stress Within the PEN

5.1.1. FEM Model

Shown in Figure 5.1 is a finite element model created using ANSYS 6.0 for a single cell. The element PLANE82 (6 node triangular and plane-strain) was used to mesh the geometry. The final mesh consisted of 21688 elements. The electrolyte was meshed with an element size of 5 μm extending two layers into both the anode and cathode after which the mesh increased in size. For the plots of stress along the *y*-axis the elements were refined at the electrolyte layer to approximately 1 μm element edge length. The material properties used in the computations are listed in Table 5.1. Numerical computation was carried out for $\Delta T = -1000^0 C$. In reference to the physical problem this means the stress free state is assumed at the maximum sintering temperature (1400ºC) the thermal stresses are examined at 400ºC. Due to symmetry, only one half of the cell was modeled. The line of symmetry (the center of the cell) is shown in Figure 5.1. No mechanical constraints were placed on the model.

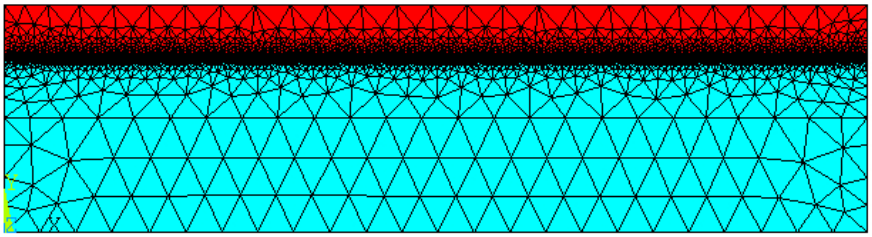

Figure 5.1: FEM mesh for half of single cell.

Table 5.1: Material properties and dimensions of the PEN used in 2-D analysis.

	d **(mm)**	***E*****(GPa)**	ν	α **(10^{-6}/ºC)**	***L*** **(mm)**
Cathode (LSM+YSZ)	0.3	96	0.3	10.56	5
Electrolyte (YSZ)	0.01	200	0.3	10.56	5
Anode (Ni+YSZ)	1.0	96	0.3	12.22	5

5.1.2. Numerical Results

The deformed shape of the half cell is shown in Figure 5.2. The stress contours are shown in Figure 5.3 and Figure 5.4. A feature observed from the FEM results is that the stress field is uniform throughout much of the cell, which is in agreement with work using beam theory (Chiu and Liou 1995). The non-uniformity occurs within approximately two cell thicknesses from the edge.

From Figure 5.3 it can be seen that compressive stresses form in the electrolyte and cathode, while the anode is in tension. The compressive stresses on the bottom half of the anode is due to the model deformation. If the temperature change was reversed (stress free at 400ºC and the final temperature is 1400ºC) then the compressive and tensile sections are reversed.

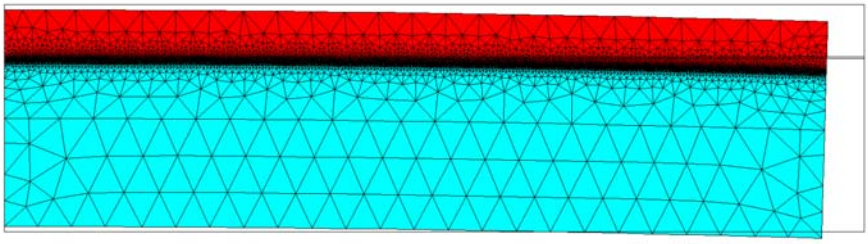

Figure 5.2: Deformed shape of a half cell (cell center is at the left).

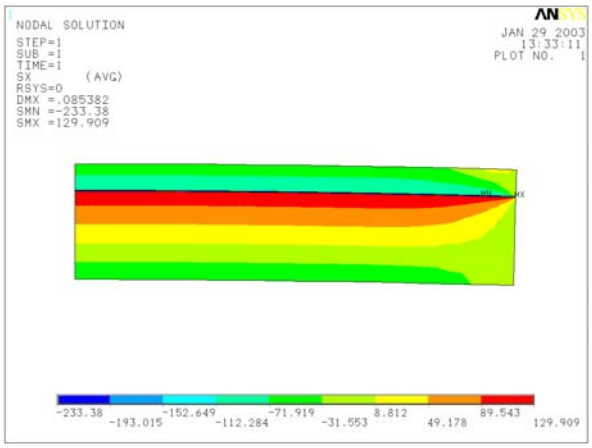

Figure 5.3: In-plane normal stress (σ_x-MPa)

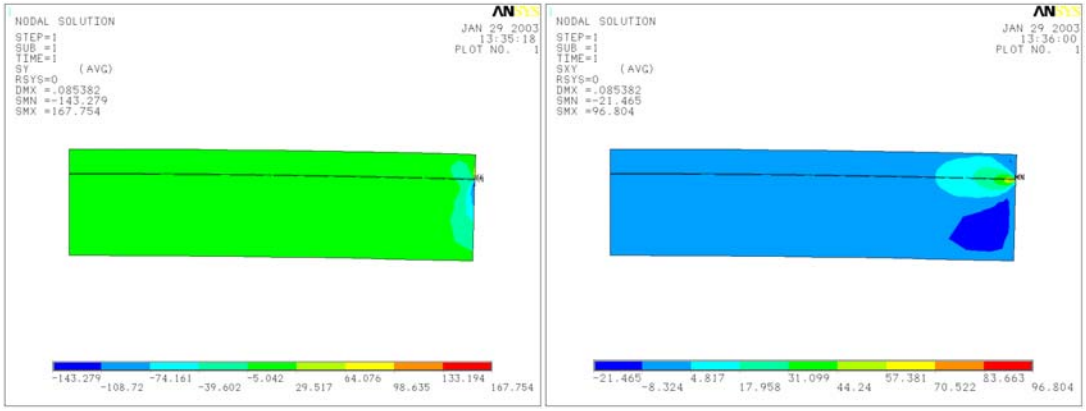

(a) (b)

Figure 5.4: (a) Out of plane normal stress (σ_y-MPa) and (b) shear stress(σ_{xy}-MPa)

5.2. Crack Growth in the Anode based on Stress Intensity Factor

5.2.1. FEM Model

A two dimensional single cell model was created using ANSYS. Due to symmetry, only one-half of the cell was meshed, as shown in Figure 5.5. The line of symmetry is simulated in the model by the "roller condition". The model was meshed with eight node quadrilateral elements and a vertical crack was embedded in the anode.

The ANSYS software provides for the calculation of the stress intensity factor by extrapolation of equations defining displacements at the crack tip. The use of singular elements at the crack tip increases the accuracy of the stress intensity calculation, but these singular elements can only be used for cracks away from the interface. The stress singularity at each crack tip was modeled with skewed quarter-point quadrilateral elements degenerated to triangular elements. Two rows of singular elements were created at the crack tip each with a radius of 1.25μm.

The initial crack was placed perpendicular to the electrode layers at a distance of 0.25mm from the cell center and 0.89mm from the bottom of the anode. The total length of the model was 1.5mm. The crack growth was manually extended toward the electrolyte. This was done since the compressive stresses at the bottom of the anode would halt crack growth, therefore it can be assumed only the top half of the crack would extend.

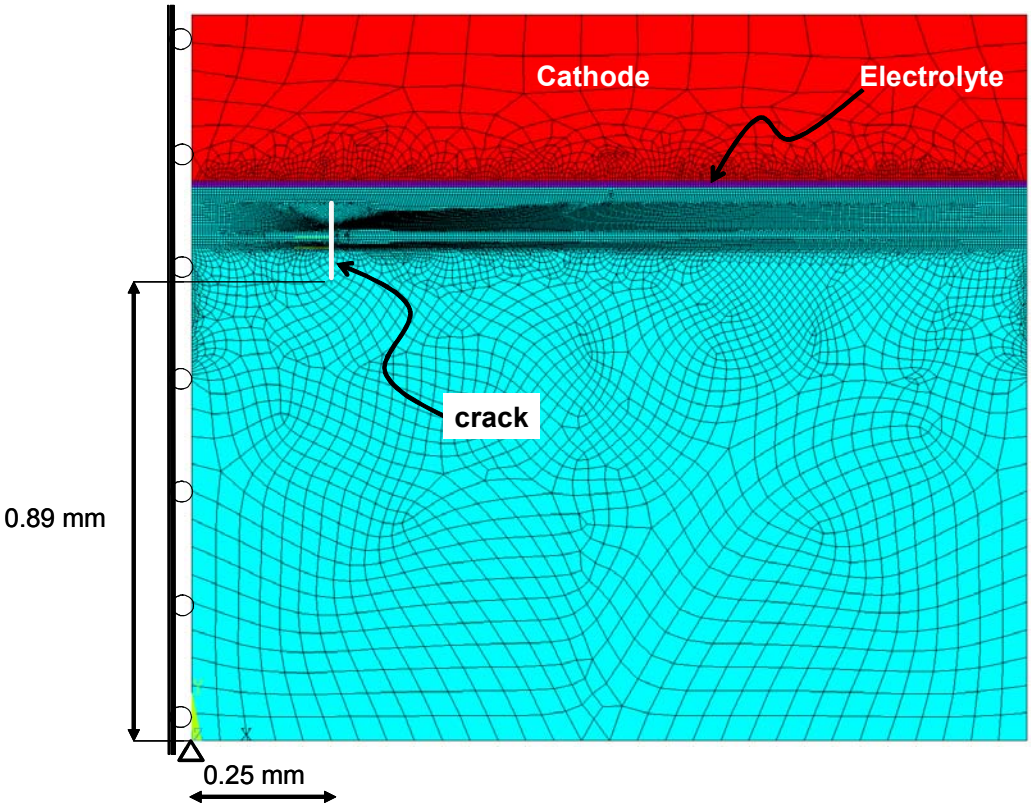

Figure 5.5: A crack embedded in the anode

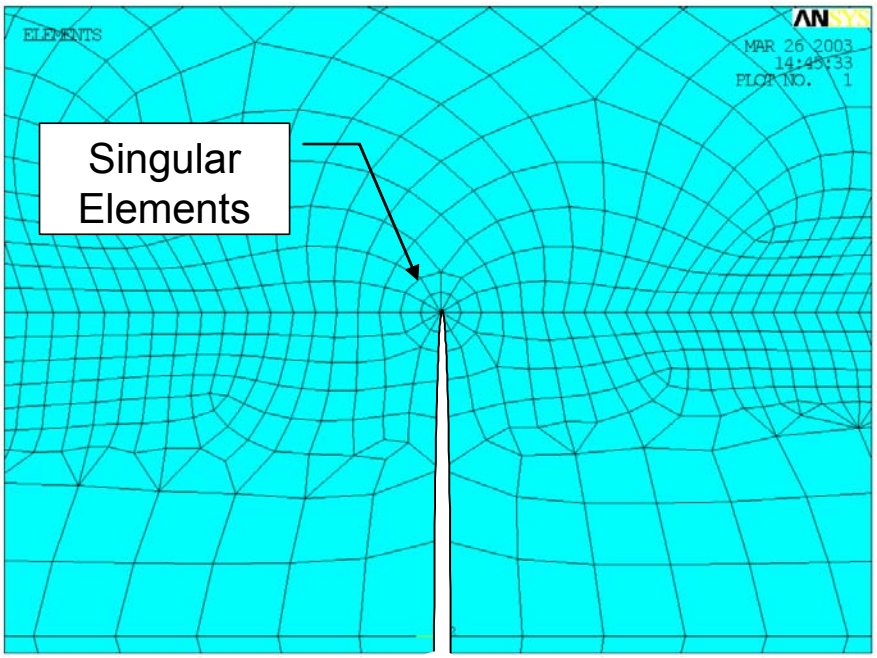

Figure 5.6: An enlarged view of the crack tip mesh shown above.

5.2.2. *Numerical Results*

It should be noted that although the stress field may vary significantly through the thickness of the cell, it is uniform along the cell; Figure 5.3: In-plane normal stress. The existence of a small crack is felt only by the immediate area surrounding the crack. Therefore, when studying crack behavior, it suffices to model a small region near the crack. For this reason, as well as in the future edge delamination analysis, only a small portion of the total cell length was modeled. Figure 5.7 is the comparison of the stresses with and without the crack.

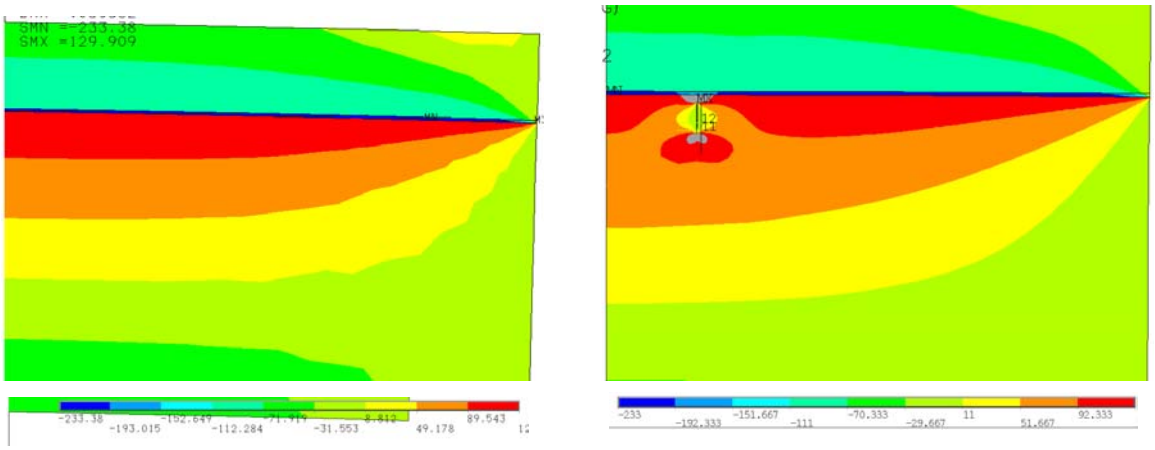

(a) (b)

Figure 5.7: Comparison of stress (σ_x MPa) between cell (a) without and existing crack and cell (b) with an existing crack.

The results for a temperature change of 1000^0C are given in Table 5.2. The energy release rate was calculated using eqn (3.5). The table lists the growing crack size and the corresponding decrease in distance from the electrolyte layer. For increasing crack lengths the Mode I and Mode II stress intensity factors and the energy release rate are listed.

Table 5.2: Crack tip stress intensity factors and energy release rate.

Crack Size (μm)	**Distance from Electrolyte (μm)**	K_I **(MPa√m)**	K_{II} **(MPa√m)**	G **(J/m^2)**
20	90	0.582	0.009	3.21
30	80	0.725	0.011	4.98
40	70	0.849	0.013	6.84
50	60	0.960	0.014	8.73
90	20	1.338	0.019	16.97
105	5	1.396	0.017	18.49

Based on the data shown in Table 5.2, two conclusions can be drawn. First, the maximum tolerable initial flaw size is around 50μm, if the toughness of the anode is 10 J/m^2, a typical value for Ni/YSZ . Crack lengths greater that than 50μm could result in failure. Secondly, once fracture occurs, the crack will grow toward the electrolyte layer in an unstable fashion, demonstrated by the increase in the energy release rate as the crack moves toward the electrolyte layer.

5.3. Edge Delamination and the Use of Energy Release Rate

Unlike cracks in the anode that most likely will lead to the fracture of electrolyte, an edge delamination has the propensity to continue along the interface, or be deflected into the electrolyte or the anode, as illustrated below.

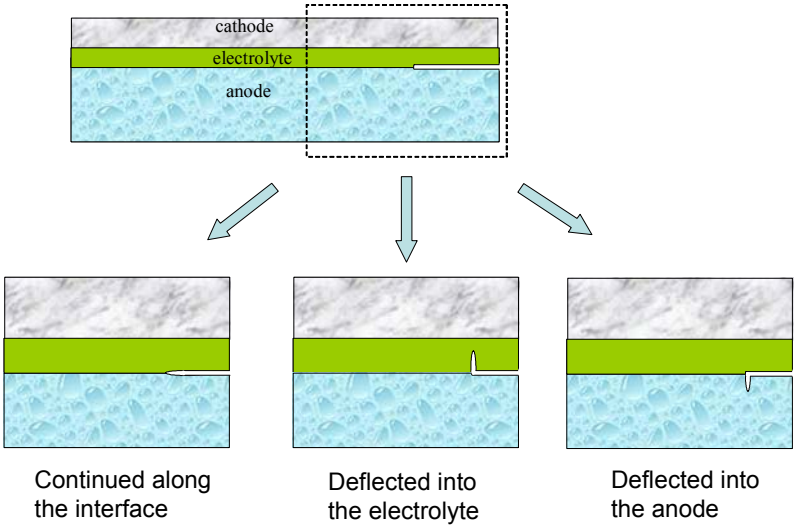

Figure 5.8: Possible cracking paths for an edge delamination

To determine the crack path, let the fracture toughness of the anode, electrolyte and their interface be denoted by G_c^a, G_c^e, and G_c^i, respectively. Although the exact values of these material properties need to be experimentally determined, literature data indicates that for typical Ni/YSZ anode and YSZ electrolyte,

$$G_c^i \le G_c^a \le G_c^e \quad .$$

Let the energy release rates for cracks deflected into the anode, electrolyte and continued along the interface be, respectively, G^a, G^e and G^i. Once these values are computed using the finite element method, possible cracking path can be determined based on the following criteria:

(1) between continuing along the interface and going into electrolyte

$$\frac{G^e}{G^i} > \frac{G_c^e}{G_c^i} \Rightarrow \text{ going into electrolyte}$$

(2) between continuing along the interface and going into anode

$$\frac{G^a}{G^i} > \frac{G_c^a}{G_c^i} \Rightarrow \text{ going into anode}$$

(3) between going into anode and going into electrolyte

$$\frac{G^e}{G^a} > \frac{G_c^e}{G_c^a} \Rightarrow \text{ going into electrolyte}$$

5.3.1. FEM Model.

The virtual crack extension method was used to calculate the energy release rate for edge delaminations. The virtual crack extension method simulates crack growth using a finite mesh extension at the crack tip and calculates the energy release rate using (3.5). At first calculations were carried out to obtain the total strain energy, $U(a)$, in a model with a given crack of length a. Next, the crack was extended by some increment (Δa) and the total strain energy ($U(a+\Delta a)$) was calculated. The crack tip energy release rate is thus given by

$$G = \frac{U(a+\Delta a) - U(a)}{\Delta a} \qquad (5.1)$$

The crack extension was realized by shifting (in the direction of crack growth) all the crack-tip nodes within a radius of one-half of the crack length by 1% of the crack length. Because of the large stress gradient, a very fine mesh must be used near the crack tip, especially for interfacial fracture. Singular elements were not used to model the interfacial crack but an extremely fine quadratic mesh was used. The mesh maintained a better aspect ratio after crack growth and was easier to implement for the different crack configurations.

To calculate the energy release rates G^a, G^e and G^i, ANSYS models were created for a single cell with an existing edge delamination of 50 μm along the anode/electrolyte interface. The mesh is shown in Figure 5.9.

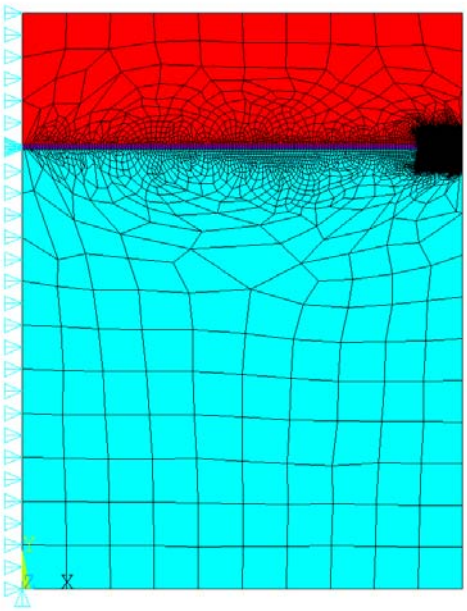

Figure 5.9: Finite element mesh for an edge delamination

5.3.2. Numerical Results

The energy release rate was calculated for a temperature loading of 1000^0C. This was done to ensure that the edge delamination would undergo an opening load. This would simulate a condition in the cell where the stress free state has changed to room temperature due to microcracking or stress relaxation in the PEN. When the cell is heated to an operating temperature of 1025ºC stresses are now induced.

The results are listed in Table 5.3: Energy release rate for various crack paths from an edge delamination, which lists the energy release rates for the different crack

paths of Figure 5.8. Making use of this data, in conjunction with the crack path selection criteria, one can conclude that the edge delamination will not cause fracture of the electrolyte unless the fracture toughness of the electrolyte is less than ~ 30% of that of the interface or that of the anode. This is typically not the case for Ni/YSZ anode and YSZ electrolyte. Therefore, for YSZ planar cells, edge delamination is likely to grow either along the interface or grow into the anode, both are less catastrophic than electrolyte fracture which leads to fuel leakage. The typical value of G_c for Ni/YSZ cermet is around 10 J/m^2, for YSZ it is about 30 J/m^2.

Table 5.3: Energy release rate for various crack paths from an edge delamination

Path	**Energy Release Rate (J/m^2)**
G^e	3.24
G^i	10.12
G^a	11.61

CHAPTER 6. THREE DIMENSIONSAL FRACTURE

The previous chapters used simplifying assumptions such as plane strain to study fracture in two dimensional finite element models. While valuable information was gathered, the complicated stress fields within SOFCs require the ability to analyze three dimensional fractures. Several difficulties arise in implementation of 3-D models. For instance in the anode-supported cell, the electrolyte can be as little as three percent of the total anode height. The extremely small size of the electrolyte requires an increased number of elements to accurately analyze the electrolyte's behavior during fracture. The addition of a flaw to the model can require element sizes at least one-eighth the length of the crack around the fracture region (Ansys 2003). When the model is expanded three dimensionally the elements required for analysis is multiplied by the width, making a detailed fracture analysis computationally difficult and time consuming.

Therefore future 3-D structural analysis needed to be portioned into three separate steps:

1. global cell model,
2. local fracture model,
3. and calculation of fracture parameters.

The global model would be created as determined by the requirements of the manufacturer and could incorporate implementation of temperature fields determined from a fluid thermal analyses. The global–local modeling technique can then be used to extrapolate the boundary displacements and temperature fields from a location in the full scale model to a smaller fracture model. The global–local modeling is acceptable because the occurrence of flaws within the stack has been shown to influence only those regions immediately surrounding the crack, while the rest of the model is unchanged

(refer Figure 5.7). Fracture parameters can then be determined from the local model using the volume integrals discussed in Section 3.4.

The following sections in this chapter will focus on the development of a three dimensional fracture model that can be used to calculate fracture parameters of fuel cells. For fracture analysis of fuel cells to be viable it is required that the stress intensity factors for curvilinear cracking, interfacial cracking, thermally stressed, and mechanically stressed bodies can be calculated.

6.1. Energy Release Rate Implementation

Since most commercial FEM packages have limited or no domain integral capabilites it is more convenient to create a program to calculate the fracture parameters during postprocessing. For the purposes of this study the finite element programs were performed using the software ANSYS 7.1 with the postprocessing of fracture parameters performed using the commercial programming language Matlab 6.5. Development of the postprocessing procedure was based on the procedures described from reference (Li 1985) and (Gosz 2002). Figure 6.2 is a flow chart representing the steps taken during postprocessing.

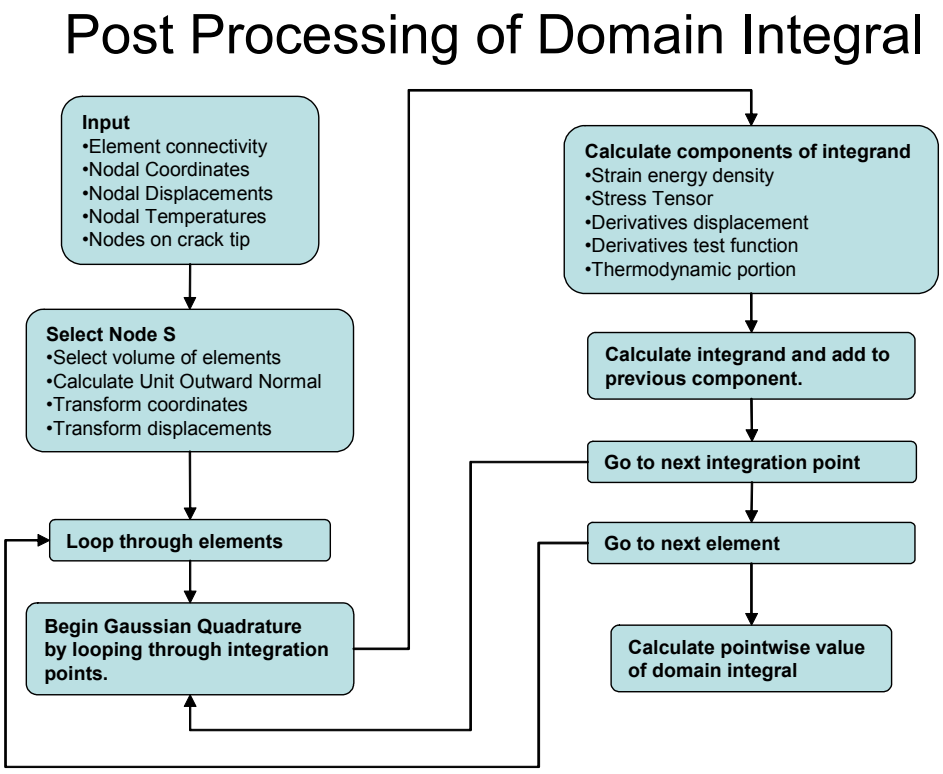

Figure 6.1: Flow chart of steps taken during postprocessing of domain integral

6.1.1. Finite Element Calculations

Calculation of the volume integrals in Section 3.4.1 can be done using several basic concepts and various constants concerning calculation of stress and strain from finite element methods. Gaussian quadrature is the numerical integration process used for the post processing code. The following paragraphs briefly discuss the steps taken to calculate the domain integral (3.17).

The strain energy density of each element is calculated by dividing the total strain energy of the element by the element's volume. The strain energy (U) is calculated from equation (6.1) where $\mathbf{E}$ is the elasticity matrix. The subscript (e) denotes the value for each element, while V is the volume of the selected element.

$$U^{(e)} = \int_V \frac{1}{2} \varepsilon^T \mathbf{E} \varepsilon dV \tag{6.1}$$

The second part of the momentum tensor $(\mathbf{P})$ looks at the stress and strain fields within the volume. Using the chain rule the derivatives of the displacements (u_i) can be calculated using equation (6.2), where N_I is the shape functions for the element and r_J represents the natural coordinates.

$$\frac{\partial u_i}{\partial x_j} = \sum_{I=1}^{node} \sum_{J=1}^{3} \frac{\partial N_I}{\partial r_J} \frac{\partial r_J}{\partial x_j} u_{iI} \tag{6.2}$$

Lastly the test function ($\mathbf{q}$) needs to be fully defined. If the node of interest (S), is taken to be the new origin and the nodal coordinates and transformations are translated as shown in Figure 6.2 the definition of $\mathbf{q}$ is simplified. The nodal values of $\mathbf{q}$ is defined by a piecewise function. Nodal values on the outer boundary are equal to zero while the nodal values within the volume are represented by any continuous vector. Therefore the nodal (Q) value at each node can be defined below:

$$Q_I = \begin{cases} [1\ 0\ 0] \text{ within volume} \\ 0 \text{ on outer boundaries} \end{cases} \tag{6.3}$$

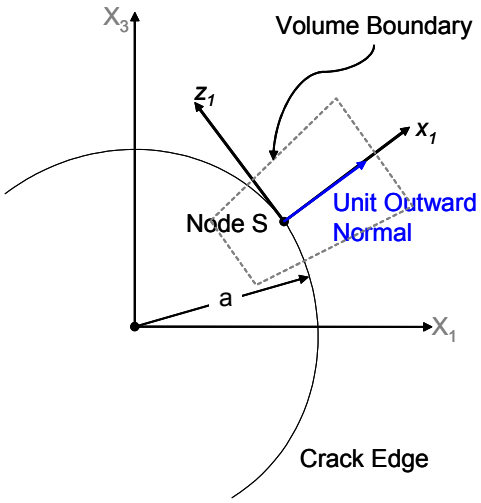

Figure 6.2: Transformation to new coordinate system and nodal Q values

By defining the test function at each node, the isoparametric formulation can be used to calculate the derivatives at each integration point.

$$\frac{\partial q_i}{\partial x_j} = \sum_{I=1}^{node} \sum_{J=1}^{3} \frac{\partial N_I}{\partial r_J} \frac{\partial r_J}{\partial x_j} Q_{iI} \tag{6.4}$$

It is now possible to calculate the average domain integral and the energy release rate at node S using the Gaussian Quadrature as shown below.

$$\overline{G} = -\sum_{e-V} \left\{ \sum_{k=1}^{n} \sum_{l=1}^{n} \sum_{m=1}^{n} \left(tr\left[W\mathbf{I} - \nabla \mathbf{u} \bullet \sigma \right] \nabla \mathbf{q} - \left(\alpha\theta\mathbf{I} \right) \mathbf{q} \right) \det \mathbf{J} w_k w_l w_m \right\} \tag{6.5}$$

Equation (6.5) sums all the elements (e) that appear within the selected volume (V) and is written in tensorial notation. The number of Gaussian points used is designated by n and the Gaussian weighting values are designated by w. The differential volume (dV) is represented by the determinant of the Jacobian matrix $(\mathbf{J})$. The Jacobian matrix and is defined below.

$$dV = \det\left(J\right) = \det\left(\frac{\partial x_i}{\partial x_j}\right) \tag{6.6}$$

Before calculating the pointwise value the chord lengths between nodes S and the nodes S+1 and S-1 on the crack tip need to be defined as L_1 and L_2 (refer to Figure 3.7). If the values are know then:

$$G(s) = \frac{2\overline{G}}{L_1 + L_2} \tag{6.7}$$

6.2. Interaction Integral

The interaction integral as described in Section 3.4.2 is used to calculate the stress intensity factors for bimaterial and homogenous cracks. The same finite element techniques as described in the previous section are used in the post processing calculation. However, before the interaction integral can be used in thermal conditions the integral derivation must take into account the effect of non-isothermal temperature conditions.

6.2.1. Formulations to Account for Thermal Strains

Previously, the stress intensity factor was calculated using the interaction integral as described in the 1998 Gosz paper. While that form of the integral can analyze curvilinear bimaterial cracks the integral does not account for thermal strains. The interaction integral was reexamined to include thermal effects in the derivation. The newly derived equation is shown below.

$$\overline{I} = \overline{G}_{\text{int}} = -\int_V \left(P_{jk}^{\text{int}} \frac{\partial q_j}{\partial x_k} + \frac{\partial P_{kj}^{\text{int}}}{\partial x_j} q_k \right) dV \tag{6.8}$$

$$P_{jk}^{\text{int}} = \sigma_{mn} \varepsilon_{mn}^{aux} \delta_{jk} - \sigma_{ik} \frac{\partial u_i^{aux}}{\partial x_j} - \sigma_{ik}^{aux} \frac{\partial u_i}{\partial x_j} \tag{6.9}$$

$$\frac{P_{kj}^{\text{int}}}{\partial x_j} = \sigma_{ij}\varepsilon_{ij,k}^{aux} - \sigma_{ij}u_{j,ik}^{aux} - \sigma_{ij,i}^{aux}u_{j,k} - \alpha\sigma_{ii}^{aux}\theta_{,k} \tag{6.10}$$

The last term in equation (6.10) is the only new term in the interaction integral, and multiplies the thermal expansion coefficient and the trace of the stress by the spatial derivatives of the temperature. The integral assumes zero body forces and crack face tractions, but can be used for curvilinear cracks. The material is also isotropic.

6.2.2. Postprocessing Implementation

The calculation of the interaction integral can be performed concurrently with the calculation of the energy release rate, but several additional calculations are required. In his 1998 paper Gosz describes the creation of a curvilinear coordinate system to eliminate the derivatives with respect to the out of plane component of the auxiliary plane strain solution. A new coordinate system is created for each integration point, which greatly simplifies calculation of the higher order gradients. A detailed description of this process is included in Appendix B. The appendix includes the steps necessary to calculate the higher order gradients that occur in the interaction integral. The additional steps necessary to calculate the interaction integral are listed Table 6.1 and start at the first Gaussian integration point (refer Figure 6.1):

Table 6.1: Additional postprocessing steps for computation of interaction integral

1.	Calculate Point S on the crack tip closet to the integration point.
2.	Set Point S as the new origin and transform coordinates, displacements, and test function to new system. (The crack plane unit vectors will be normal and tangent to the crack curve at Point S.)
3.	Calculate the radius of curvature of the crack edge at point S.
4.	Calculate auxiliary values of interaction integral using methods described in appendix A.
5.	Input auxiliary values and finite element values into equation (3.27).
6.	Continue to next integration point.

6.3. Program Summary

For this method of calculation the meshing and volume selection for the domain integral have requirements set by code limitations. A mapped mesh was used to insure that selected nodes were always normal to the crack plane and to simplify definition of the test function $(\mathbf{q})$. Secondly, while the size of the volume is flexible perpendicular and normal to the crack only one row of elements can be included on either side of node S. This is necessary for more accurate calculation of the pointwise value.

Table 6.2 summarizes the capabilities of the post processing MatLab code created. It incorporates the thermal and curvilinear coordinates in the interaction integral to allow for a flexible postprocessing routine.

Table 6.2: Summary of post-processing capabilities.

Model Types	-In-plane curvilinear 3d cracks -Homogenous cracks -Bimaterial Interface cracks -Thermally Stressed
Programming Limitations	-20 Node brick elements -Mesh normal from crack edge -Zero body forces -Zero crack face tractions
Outputs	-Energy Release Rate (G) -Mode I, II, and III stress intensity factors $(K_I, K_{II}, \text{ and } K_{III})$ -Phase Angle (ψ)

6.4. Verification: Axisymmetric Bimaterial and Thermally Stressed Cracks

If the domain and interaction integrals are to be of significance it is necessary to look at fracture parameters at all points on the crack edge. This is especially important with regard to fracture within fuel cells where the electrochemical reactions cause varied stress fields. Initially a standard model of a penny shaped crack was created. This model was used to verify the accuracy of the domain integral calculations under a known solution. Eventually, this same model will be used to analyze fracture in a fuel cell using the global—local modeling techniques.

Contour plots of the three dimensional models are not included in the main text to conserve space; however, Appendix C includes plots of deformation and stress near the crack tip for each model.

6.4.1. Bimaterial Penny Shaped Crack

A crack was considered to occur between the anode and electrolyte; refer to Table 4.2: Typical material properties of PEN materials for the material constants used.

The solution for the problem is in equation (6.11) and was taken from (Kassir and Bregman 1972).

$$K_I + iK_{II} = 2\sigma_o\sqrt{a}\,\frac{\Gamma(2+i\varepsilon)}{\Gamma(.5+i\varepsilon)}(2a)^{-i\varepsilon} \tag{6.11}$$

σ_o is the remote stress applied to the model. The gamma function (Γ) can be defined from the power series as shown below (Tada, Paris et al. 2000).

$$\Gamma(x) = \lim_{n\to\infty}\frac{n!\,n^{x-1}}{x(x+1)(x+2)\ldots(x+n-1)}\text{, for any real or complex } x. \tag{6.12}$$

6.4.1.1. Fem Model

The fracture model was developed and analyzed with Ansys 7.0 software and used the 20 node brick element. The crack tip mesh used only brick elements to reduce computation and to simplify meshing of future crack configurations. For a circular mesh the element size (e) along the crack tip is held at a constant ratio with respect to the crack length (a). This element size was held constant for nine layers extending in all four normal directions from the crack tip and crack plane. Outside the layers around the crack tip the element size is allowed to increase as shown in Figure 6.3. Since one-quarter symmetry was used the planar sides were considered to be on rollers. A remote pressure was applied to the top and bottom, while the model was held fixed in the vertical direction at the bottom.

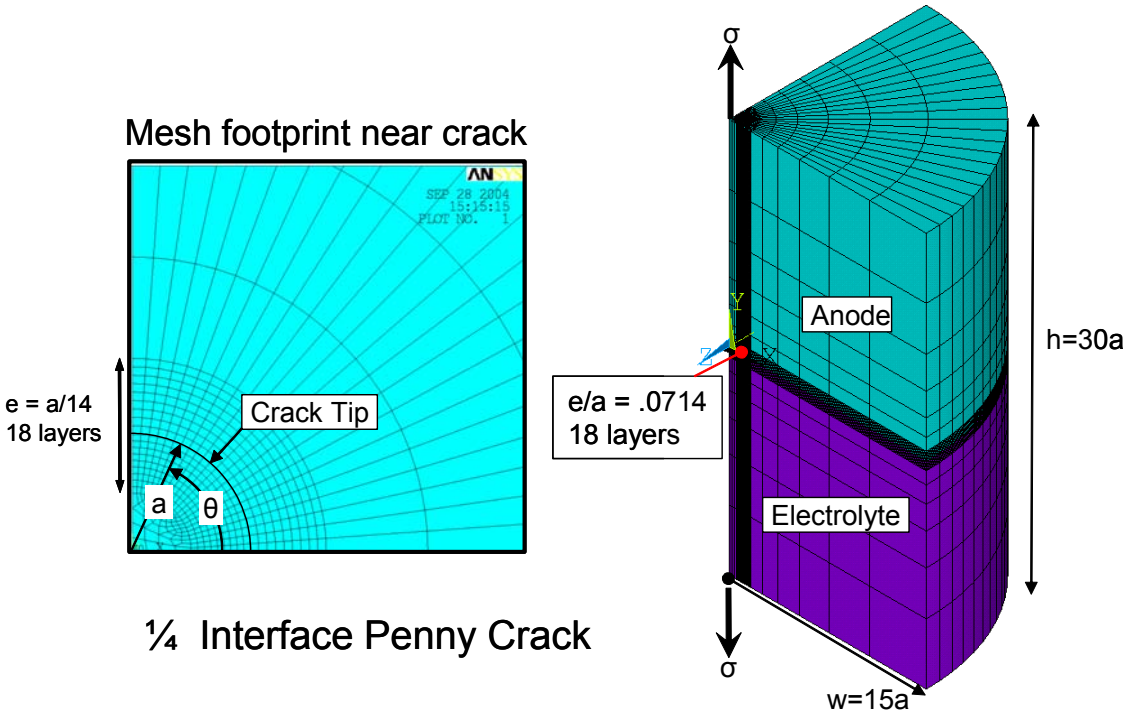

Figure 6.3: Model configuration and boundary conditions for bimaterial penny crack

6.4.1.2. Numerical Results

Several sets of data were calculated from the crack model. The values of the complex stress intensity factors, the energy release rate calculated by both the domain integral and from equation (3.11) using the stress intensity factors, and finally the value the phase angle.

In Table 6.3 normalized values of the fracture parameters are compared between the analytical result (6.11) and the numerical results obtained in this thesis. The table lists values taken at the maximum location of error. It can be seen that although there is error in both KI and KII, the larger error in KII dominants the results of the phase angle. It can also be seen that the energy release rate when calculated from the numerical stress intensity factors is much more accurate than the energy release rate from the

domain integral. This is reasonable since the domain integral calculation does not account for the nonzero divergence of the curvilinear crack (refer to section 3.2.1).

Table 6.3: Normalized Fracture Parameters at Theta ~ 90º (Location of Max Error)

Crack Size (μm)	$\frac{\sqrt{\pi}\,\mathrm{Re}\left[\mathbf{K}(2a)^{i\varepsilon}\right]}{2\sigma_o\sqrt{a}}$	$\frac{\sqrt{\pi}\,\mathrm{Im}\left[\mathbf{K}(2a)^{i\varepsilon}\right]}{2\sigma_o\sqrt{a}}$	$\frac{\pi E^* \cosh^2(\pi\varepsilon) G}{4\sigma_o a}$	$\frac{\pi}{4\sigma_o a}\mathbf{K}\overline{\mathbf{K}}$	**ψ (º)**
Numerical	0.992	0.074	1.077	0.989	3.00
Analytical	0.986	0.077	0.996	0.996	3.12
% Error	-.629	3.390	-8.166	0.990	3.71

For prediction of crack growth in fuel cell models an understanding of error magnitude with respect to mesh location also needs to be developed. Figure 6.4 shows the angle for each point along the crack tip. A plot of the normalized values of KI and KII at each node of the crack tip and a plot of the magnitude of error for KI, KII and the phase angle are shown in Figure 6.5 through Figure 6.7 with respect to the angle of Figure 6.4. In the case of Figure 6.7 it can be seen how the error of KI and KII help magnify error for the phase angle calculation. Contour plots of the stress fields and deformation of the penny shaped crack can be found in Appendix C.

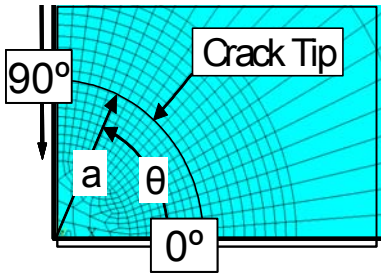

Figure 6.4: Angle coordinates along crack tip

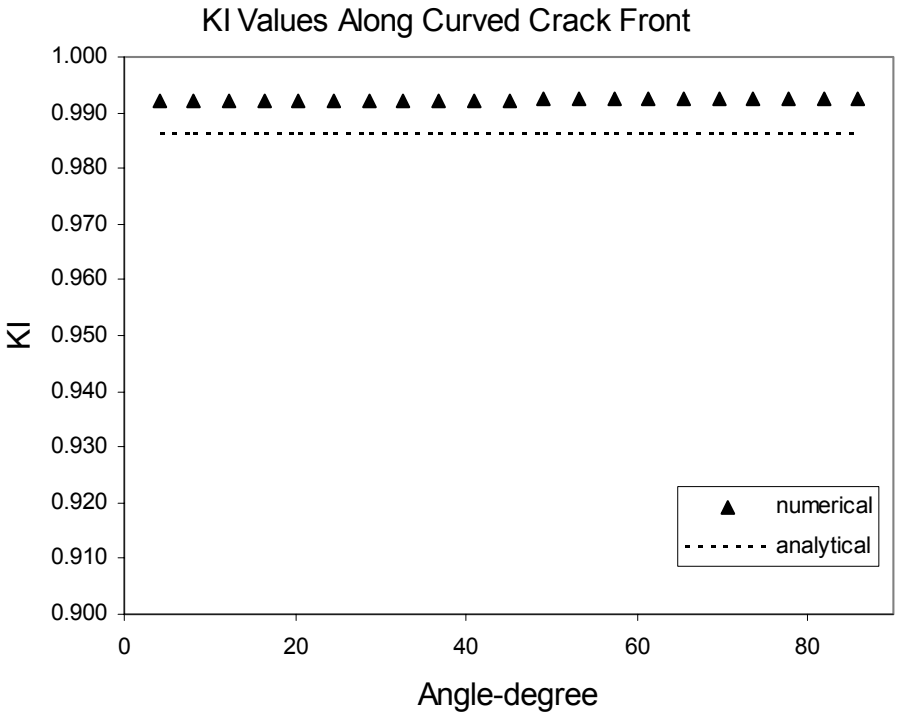

Figure 6.5: Normalized Values of KI with respect to angle

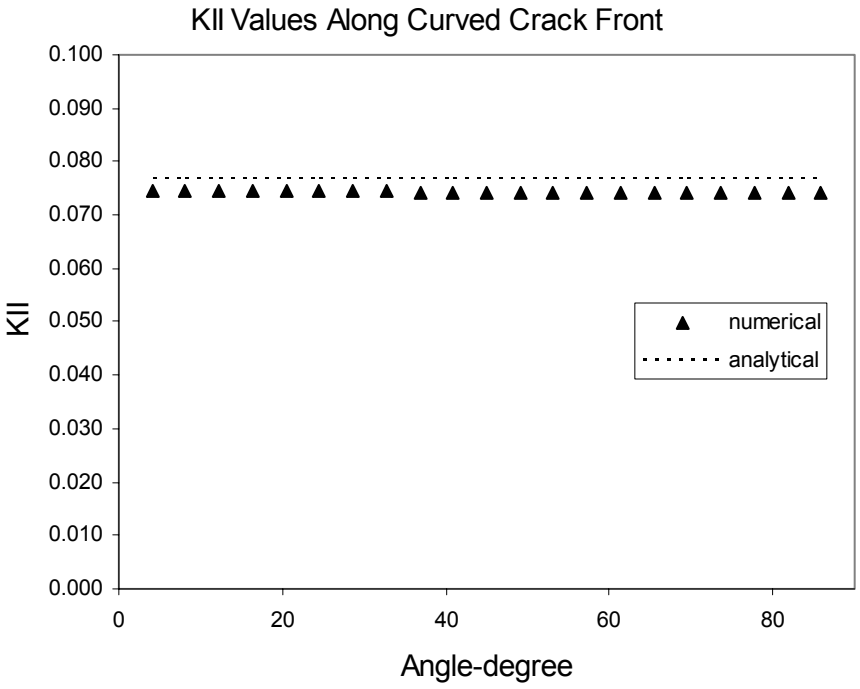

Figure 6.6: Normalized Values of KII with respect to angle

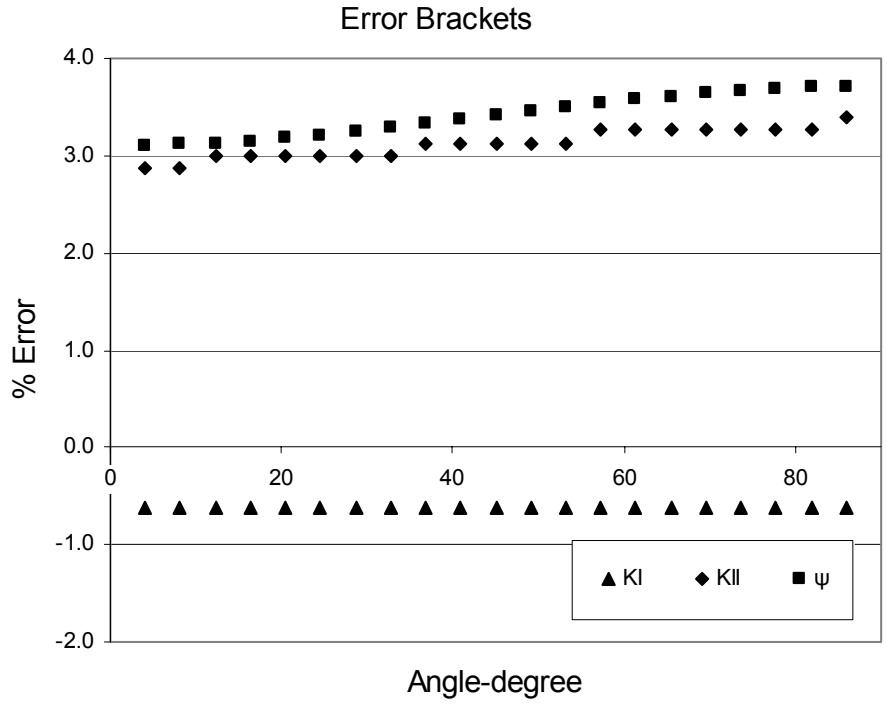

Figure 6.7: % Error along curved crack front

6.4.2. Thermally Stressed Straight Crack

A straight crack was used to examine the accuracy of the interaction integral because of the availability of a known solution. The fracture parameters of this model can be compared to an isothermal model in which the crack face is loaded by tractions equal to those that appear on a non-cracked model under the same thermal load (Wilson and Yu 1979).

The solution was verified by two different methods. First it was compared to the FEM solution of the 2-D plane strain crack loaded with crack face tractions. An analytical solution for the crack traction loading in an infinite body is also examined, refer to Tada's The Stress Analysis of Cracks Handbook (2000). The analytical solution of a crack face under a linear stress distribution is shown in equation (6.13). The pressure

(p) is the maximum traction on the crack face and is calculated from the maximum temperature (θ_f) and thermal expansion coefficient (α) in equation (6.14).

$$K_I = \left(1 - \frac{2}{\pi}\right) p\sqrt{\pi a} \tag{6.13}$$

$$p = \frac{E\alpha\theta_f}{1 - v} \tag{6.14}$$

6.4.2.1. FEM Model

Figure 6.8 shows the material properties used and the model configuration. One-quarter symmetry is applied such that the symmetry planes lie on the crack plane and along the xy-plane. Finite element boundary conditions placed these planes on rollers. The external displacement conditions placed the top edge on rollers with one corner fixed. The crack length to width ratio (a/w) is set to 0.5, while the height to width ratio (h/w) is 2.0. The model thickness is equal to one-half the width. The entire model was meshed with 20 node brick elements with a 1:1 aspect ratio and a characteristic length of $a/10$.

The final boundary condition applied is the temperature variation. The stress free temperature was set to zero degrees. The linear temperature condition is proportional to the x-coordinate and equals zero at the origin. The maximum and minimum temperatures occurred at the outer edges.

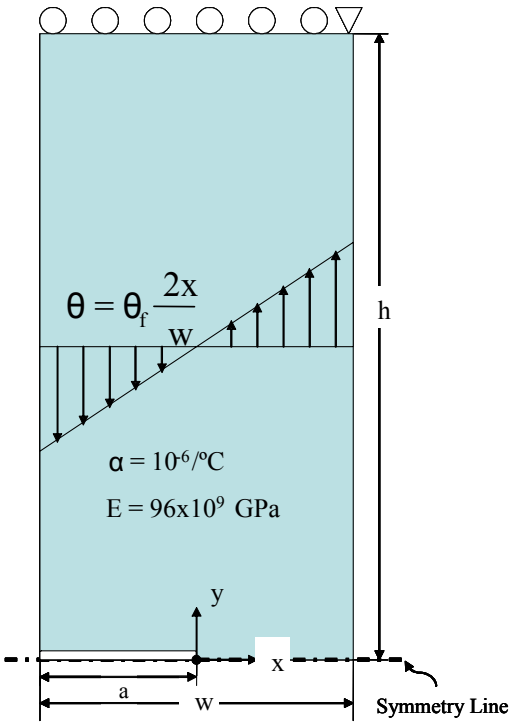

Figure 6.8: Thermally stressed crack model

6.4.2.2. Numerical Results

The stress intensity factors should be independent of the domain of the volume integral. To verify this, the stress intensity factors were calculated for increasing integration volumes using equation (6.8). Only one point along the width of the crack was examined; at the center of the body (the mid-width symmetry line). The values were calculated at this point to maximize plane strain conditions for comparison to the two dimensional analytical solution. The normalized values for each volume are shown in Table 6.4. Each volume is designated by the number of elements selected for analysis and the stress intensity values are normalized by the maximum pressure seen in the body.

Contour plots of the stress fields and deformation of the crack model can be found in Appendix C.

Table 6.4: Normalized values of KI stress intensity

# Elements in domain	$\frac{K_I}{p(\pi a)^{1/2}}$ from FEM	$\frac{K_I}{p(\pi a)^{1/2}}$ from eqn. (6.13)
4	.3615	.3630
16	.3651	
36	.3651	
70	.3651	

6.5. Penny Shaped Crack under Thermal Loading

6.5.1. Temperature Gradient Orthogonal to Crack Plane

The next model takes the penny shaped model from Figure 6.3 and applies a thermal temperature with zero applied stress. At the bottom of the anode layer the temperature is at the stress free state and increases linearly in the y-direction to a maximum temperature difference $(\theta_{\max})$.

There is no existing analytical solution for this case. Therefore the accuracy of the stress intensity factors convergence will be examined in two different ways: the crack tip mesh size will be changed for three different models, and for each model the convergence of the integral calculation will be examined for increasing integration volumes.

The values in the following tables are normalized by the thermally induced stress as functions of the change in the thermal expansion coefficient and the maximum temperature difference. The maximum stress calculation for normalization is shown in equation (6.15).

$$A = \frac{E^{'}\left(\alpha_2 - \alpha_1\right)\theta_{\max}}{\left(1-v\right)} \tag{6.15}$$

Table 6.5 shows the stress intensity, the energy release rate calculated from the stress intensity factors, and the phase angle for three different mesh sizes. Table 6.6 shows the convergence for different domains in a particular mesh. The complex stress intensity factors were listed for increasing volumes to show convergence of the volume integrals.

Table 6.5: Stress intensity factors for thermally stressed bimaterial crack

Element Size Normalized by Crack Length	$\frac{\sqrt{\pi}\,\mathrm{Re}\left[\mathbf{K}\left(2a\right)^{i\varepsilon}\right]}{2A\sqrt{a}}$	$\frac{\sqrt{\pi}\,\mathrm{Im}\left[\mathbf{K}\left(2a\right)^{i\varepsilon}\right]}{2A\sqrt{a}}$	$\frac{\pi}{4Aa}\mathbf{K}\overline{\mathbf{K}}$	**ψ(º)**
.1000	.0709	.0100	.3790(10^{-6})	6.77
.0833	.0696	.0099	.3658(10^{-6})	6.82
.0714	.0696	.0099	.3658(10^{-6})	6.82

Table 6.6: Convergence of KI and KII for mesh size of (e/a) = .0714

# Elements in domain	$\frac{\sqrt{\pi}\,\mathrm{Re}\left[\mathbf{K}(2a)^{i\varepsilon}\right]}{2A\sqrt{a}}$	$\frac{\sqrt{\pi}\,\mathrm{Im}\left[\mathbf{K}(2a)^{i\varepsilon}\right]}{2A\sqrt{a}}$
32	.0741	.0081
72	.0696	.0098
120	.0696	.0098
176	.0696	.0099
240	.0696	.0099
312	.0696	.0099

It can be seen from the tables above that the solution converges under both conditions. If the model had been a homogenous body under thermal loading conditions the stress intensity factors of the model would have been zero. This is born out in the extremely small values of the complex stress intensity factors as compared to those seen in Table 6.3: Normalized Fracture Parameters at Theta ~ 90º (Location of Max Error). However, since they are still present it is fundamental to predict thermal stress intensities during fuel cell operation. Contour plots of the stress fields and deformation of the thermally stressed crack can be found in Appendix C.

6.5.2. Temperature Gradient Parallel to Crack Plane

The final finite element model examined, applies a linear temperature gradient parallel to the crack plane. Referring to Figure 6.3: Model configuration and boundary conditions for bimaterial penny crack the model is at a stress free state at the origin of

the model. The temperature will increase linearly as a function of z and is constant in the y and x directions. The temperature seen along the crack edge will vary depending on its location in the model.

The effect of this temperature variation can be seen in Figure 6.9 which plots the normalized values of KI and KII along the crack front. The shear loading mode (KII) shows little variation along the crack length. This is reasonable because KII corresponds to the difference in the two materials. However, KI slowly increases as the maximum temperature at the crack edge increases ($\theta = 90^{o}$, z = a, x = y = 0).

Figure 6.10 plots the relationship between KI and KII along the crack front. This is done using the phase angle, which since it is very close to zero. Due to the small size of this angle this type of fracture will not deflect significantly during crack growth.

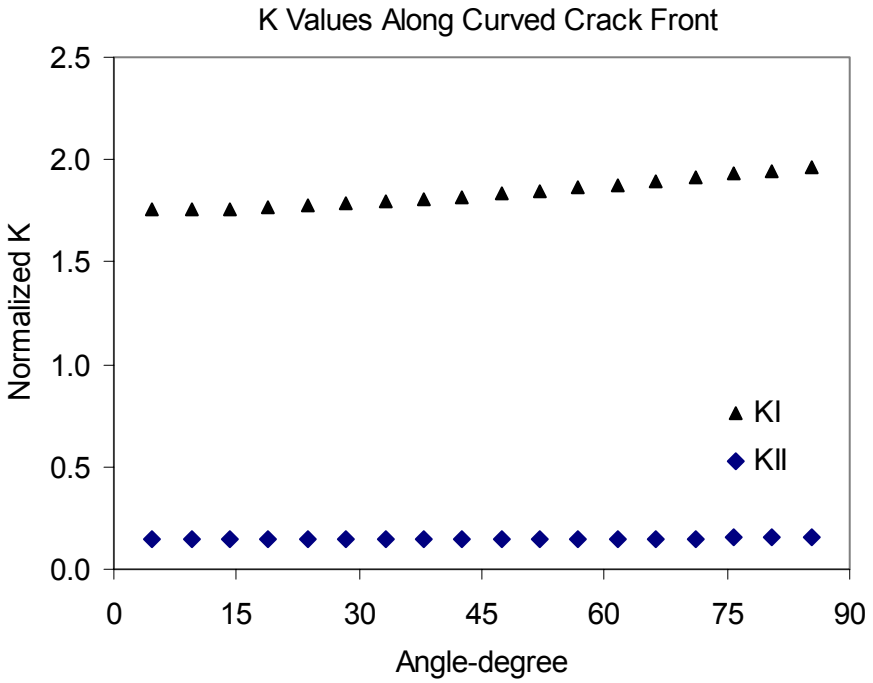

Figure 6.9: The K values along crack for temperature gradient parallel to crack plane

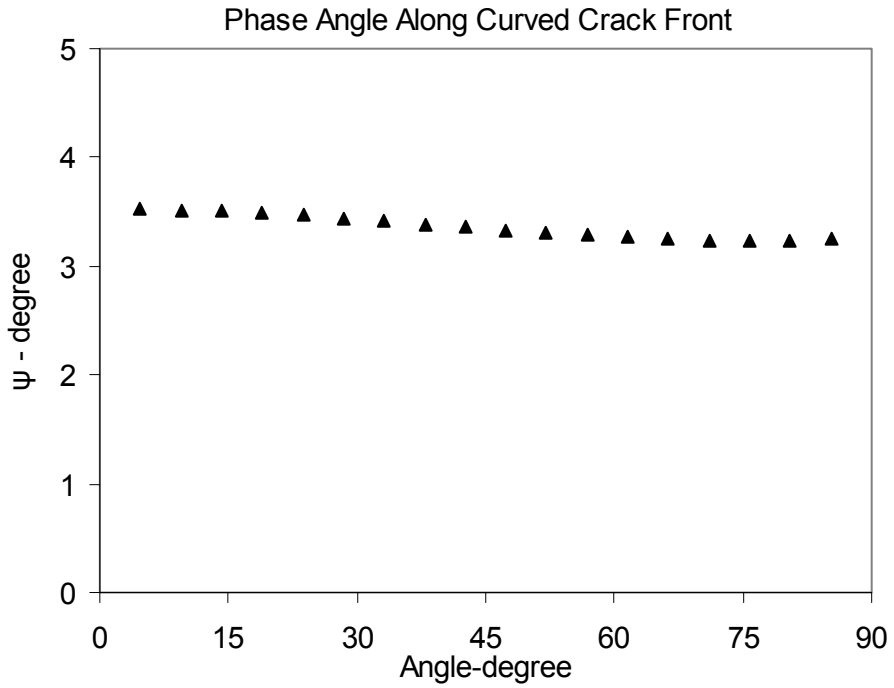

Figure 6.10: The Phase angle for temperature gradient parallel to crack plane

6.6. Model Results and the Link to Fuel Cells

While the penny crack models described in sections 6.4.1 (applied stress), 6.5.1 (orthogonal temperature gradient), and 6.5.2 (parallel temperature gradient) do not specifically describe a fuel cell model, much can be interpreted from the results. This can be done because the normalization of the stress intensity factors allows the impact of the different loading conditions to be compared. Figure 6.11 is a bar graph of the maximum stress intensity factors seen in each penny shaped model and there is also a comparison of the phase angle loading for each model.

The loading condition on the mechanically stressed crack, with no thermal loading, would induce only KI or Mode I loadings in a homogenous model. While the KII is significantly smaller than KI it is still a significant factor of any interfacial crack. Next

examination of the charts shows that temperature gradients orthogonal to the interfacial cracking plane have little or no impact of the crack. In fact the stress intensity that occurs is a direct result of the difference between the two materials, if the crack occurred in a homogenous body there would be no stress intensity. The most significant impact appears to come from the parallel temperature crack plane to the gradient. This is reasonable since the loading temperature conditions compare to a opening traction placed on the crack front.

Although the chances of deflection are minimal as shown by the very small phase angles (Figure 6.11 (b)) each value is positive, meaning deflection would occur into the anode. However, this can only be predicted by comparisons to the energy release rates and the material's fracture toughness such as demonstrated in section 5.3.

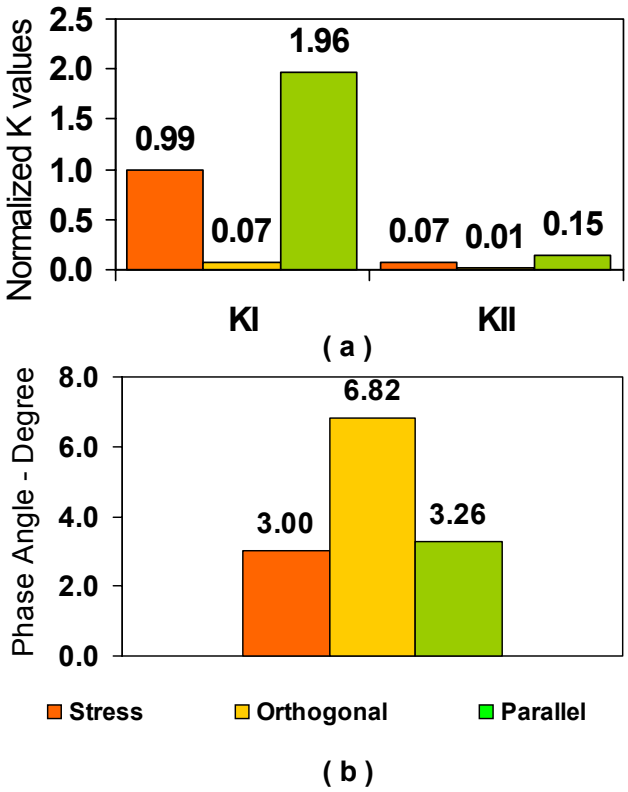

Figure 6.11: Comparison of (a) K values and (b) phase angles

CHAPTER 7. SUMMARY AND MAJOR CONCLUSIONS

7.1. Summary

SOFCs operate at relatively high temperature and over the cell lifetime the stack components (e.g., PEN and seals) are subjected to harsh environments. It has been reported repeatedly by the SOFC industries that, under combined thermomechanical, electrical and chemical driving forces, catastrophic failure often occurs suddenly due to material fracture or loss of adhesion at the material interfaces. Unfortunately, there have been very few thermomechanical modeling techniques that can be used for assessing the reliability and durability of SOFCs. It is perceivable that for future SOFC systems with high specific power and low weight, such thermomechanical failure can only be exuberated. Therefore, modeling techniques and simulation tools applicable to SOFCs are needed. Such techniques and tools enable us to analyze new cell designs, evaluate the performance of new materials, virtually simulate new stack configurations, as well as to assess the reliability and durability of stacks in operation. The major objective of this thesis research is to develop a fracture mechanics tool that can be used to analyze and model fracture failure in SOFCs and to identify failure mechanisms in SOFCs via fracture mechanics.

Toward this goal, several aspects of fracture induced material failure in SOFCs have been studied. Certain possible failure mechanisms were investigated and recommendations on how to mitigate such failure were also provided. Specifically, the propensity of edge delamination versus blistering at the electrolyte-anode interface was examined and the maximum tolerable processing interfacial defects were estimated. Stress intensity factors for cracks in the anode and on the anode-electrolyte interface

were obtained under various loading conditions including thermal residual stress using two dimensional finite element models. Furthermore, a computer software tool was developed for performing fracture mechanics analysis in SOFCs.

7.2. Significant Results

Each level of analysis provided further information about fracture occurring in SOFCs. Major findings of this research are summarized below:

- A comparison between edge and blister delaminations found the edge delaminations have inherently higher energy release rates than blister defects. Therefore edge delaminations are most likely to occur during manufacture of the electrolyte-anode layer. The likelihood of a blister delamination growing increased with the initial defect size and were dependent on the thickness of the electrolyte layer.
- Tension generated in the anode during cooling will cause the crack to grow unstable towards the electrolyte layer. If this crack impinges into the electrolyte then failure of the cell could occur from mixing of the oxidant and fuel.
- For cooling conditions it was found that edge delaminations can grow along the interface, impinge into the anode, or deflect into the electrolyte. However, from Section 5.3.2 it is found that the energy release rate is a minimum for crackings impinging into the electrolyte. Therefore electrolyte failure is least likely to occur, which avoids the catastrophic failure mode of fuel leakage into the cathode.
- Examination of the normalized values for a penny shaped crack under thermal and mechanical conditions leads to the conclusion that the primary driving force for fracture in the cell will be mechanical loading, such as residual stresses, or temperature gradients parallel to the crack plane. This can be compared to the following conditions in fuel cells:

- Interfacial or homogenous cracking under mechanical loading would apply to the impact of stresses induced by external constraints and by material residual stresses.
- The low impact of orthogonal temperature gradients implies that variation through the heights of the PEN layer will have little impact on cracks parallel to the interfaces.
- The high impact of the parallel temperature gradient implies the temperature variation along the length of the cell (corresponding to fuel flow) could have a significant impact on the cell operation. Especially near fuel or air inlets where a high temperature gradient occurs during operation.

7.3. Conclusion

Study of fuel cells is complicated because of the wide range of operating parameters and the unknown impact of fracture on fuel cell operation. Therefore techniques to optimize fuel cell performance should include several different levels of complexity. The one dimensional analysis can be used in the optimization of design variables during the manufacturing process. A specific example of this is correlation of electrolyte height to the maximum acceptable processing defects. The information can be incorporated with experimental data to help predict and understand processing defects. The two dimensional analysis demonstrated, provided an efficient method too determine areas of interest in the fuel cell. Both the 1-D and 2-D analysis can be used as a first step in a three dimensional fracture model and were a fundamental part of objective one, the study of failure mechanisms in SOFCs.

A significant contribution of the presented research is the post processing analysis of fracture parameters, the goal of objective two for this research. As it stands

there is not an easily accessible way for industries to predict fracture in three dimensional situations. Existing commercial software while sometimes capable of predicting 3-D energy release rates under mechanical loading cannot predict either the stress intensity factors or the direction of the crack growth under thermal loading conditions.

Accomplishment of numerical methods to study three dimensional fractures allowed examination of four different models: a bimaterial penny crack, thermally stressed plane strain crack, and finally a two penny shaped cracks under thermal loading. The post processing code used to examine these cracks can be combined with easily implemented global—local model routines available in many commercially available types of software. Designers can use industry-specific models in combination with the post processing routine to predict fracture behavior at specific locations. This could even be extended to a transient analysis, by performing a global transient analysis and taking a snapshot of different times and analyzing the resulting fracture. Knowledge of specific fracture behavior in the cell can help in the determination of acceptable thermal gradients during operation and allowable structural loading caused by the seals and the stack configuration. In conclusion, a combination of analytical and computational methods can be used to determine design parameters, to predict crack growth, and to provide detailed fracture analyses of realistic fuel cell models.

APPENDIX A. AUXILIARY FIELDS

The following equations describe the displacement fields for cracking at the interface. The displacements are functions of the polar coordinates, the bimaterial constant, and the shear modulus. The equations are based on those found in the Gosz, 1998 paper. The constants in A.6 differed from the published 1998 version which featured typesetting areas.

1. Calculation of the polar coordinates is shown in equation (A.1) a figure of the polar coordinates is in Figure 3.3.

$$
\begin{aligned}
&r = \sqrt{x^2 + y^2} \\
&\theta = \tan^{-1}\left(\frac{y}{x}\right) \\
&\text{For } x < 0 \\
&\theta = \begin{cases} \theta + \pi \text{ for } y > 0 \\ \theta - \pi \text{ for } y < 0 \end{cases}
\end{aligned}
\tag{A.1}
$$

2. Displacements for extraction of Mode I and Mode II stress intensity factors

$$u_i^{aux} = \frac{1}{4\mu\cosh(\pi\varepsilon)}\sqrt{\frac{r}{2\pi}} f_i(r,\theta,\varepsilon,\mu_k)\text{, where} \tag{A.2}$$

i = 1 or 2 such that $u_1 = u_x$ and $u_2 = u_y$, and

k = material number .

The KI is extracted using

$$
\begin{aligned}
f_1(r,\theta,\varepsilon,\mu_k) &= D + 2\delta\sin\theta\sin\phi \\
f_2(r,\theta,\varepsilon,\mu_k) &= -C - 2\delta\sin\theta\cos\phi
\end{aligned}
\text{ and KII requires} \tag{A.3}
$$

$$
\begin{aligned}
f_1(r,\theta,\varepsilon,\mu_k) &= -C + 2\delta\sin\theta\cos\phi \\
f_2(r,\theta,\varepsilon,\mu_k) &= -D + 2\delta\sin\theta\sin\phi
\end{aligned}
. \tag{A.4}
$$

3. Displacements for extraction of Mode III.

$$u_z^{aux} = \frac{2}{\mu_i}\left(\frac{r}{2\pi}\right)^{1/2} \sin\frac{\theta}{2} \tag{A.5}$$

4. The constants are calculated as shown below.

$$\delta = \begin{cases} e^{-(\pi-\theta)\varepsilon} & \text{for } x > 0 \\ e^{(\pi+\theta)\varepsilon} & \text{for } x < 0 \end{cases}$$

$$\phi = \varepsilon \ln(r) + \frac{\theta}{2}$$

$$C = \overline{\beta}\gamma \cos\frac{\theta}{2} - \beta\overline{\gamma} \sin\frac{\theta}{2}$$

$$D = \beta\gamma \cos\frac{\theta}{2} + \overline{\beta}\overline{\gamma} \sin\frac{\theta}{2}$$

$$\beta = \frac{0.5\cos(\varepsilon \ln r) + \varepsilon \sin(\varepsilon \ln r)}{.25 + \varepsilon^2} \tag{A.6}$$

$$\overline{\beta} = \frac{0.5\sin(\varepsilon \ln r) - \varepsilon \cos(\varepsilon \ln r)}{.25 + \varepsilon^2}$$

$$\gamma = \kappa\delta - \frac{1}{\delta}$$

$$\overline{\gamma} = \kappa\delta + \frac{1}{\delta}$$

$$\kappa = 3 - 4\nu$$

APPENDIX B. AUXILIARY GRADIENTS

The following is a detailed description of the curvilinear coordinate transformation used in calculation of the interaction integral. This appendix introduces the coordinate systems used and then starting at the auxiliary displacements calculates the gradients of the auxiliary displacements, stresses, and strains appearing in the main components of the interaction integral. The components are listed below:

$$P_{jk}^{\text{int}} = \sigma_{mn}\varepsilon_{mn}^{aux}\delta_{jk} - \sigma_{ik}\frac{\partial u_i^{aux}}{\partial x_j} - \sigma_{ik}^{aux}\frac{\partial u_i}{\partial x_j} \tag{B.1}$$

$$\frac{\partial P_{kj}^{\text{int}}}{\partial x_k} = \left[\sigma_{mn}\varepsilon_{mn,j}^{aux} - \sigma_{ik}u_{i,jk}^{aux} - \sigma_{ik,k}^{aux}u_{i,j}\right] \tag{B.2}$$

The following sections are listed as below along with relevant equation numbers:

1. Coordinate systems used (Figure B-1).
2. Calculation of the arc length (s) (Figure B-2 and eqn B.3)
3. Scaling Factors used in coordinate transformation (B.4).
4. Derivatives of physical components (B.5).
5. Derivatives of tensor components (B.6).
6. Calculation of $\left(u_{i,j}^{aux}\right)$ (B.7-B.10).
7. Calculation of $\left(u_{i,jk}^{aux}\right)$ (B.11-B.24).
8. Calculation of $\left(\varepsilon_{ij}^{aux}\right)$ (B.24-B.25).
9. Calculation of gradient strain $\left(\varepsilon_{mn,j}^{aux}\right)$ (B.26-B.37).
10. Calculation of $\left(\sigma_{ik}^{aux}\right)$ (B.38).
11. Calculation of $\left(\sigma_{ik,k}^{aux}\right)$ (B.39-B.41).

Complete Derivation of Curvilinear Coordinates

1. Coordinate systems used in calculation of stress intensities (based on Figure 5, pg 1770 from (Gosz, 1998)).

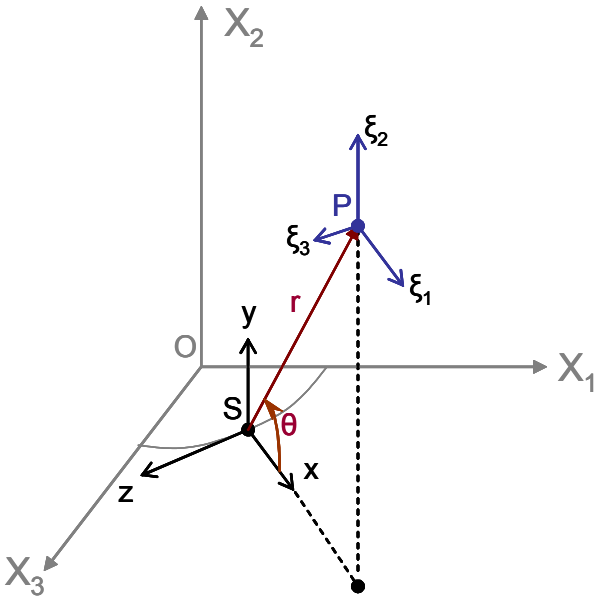

Figure B-1: The global, crack tip, and curvilinear system used.

2. Calculation of the arc length (s) introduced by the **S** Coordinate system. Equation B.3 relates the coordinates of the **S** system to the **P** system. This relation is shown graphically in Figure B.2,

$$s = (\rho + x_1)\varphi \tag{B.3}$$

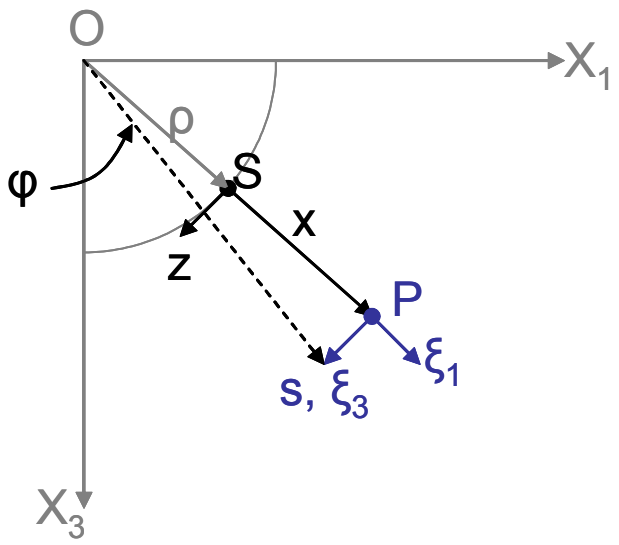

Figure B-2: Relation between **S** and **P** coordinate systems.

3. Scaling Factors used.

$$h_1 = 1$$
$$h_2 = 1$$
$$h_3 = 1 + \frac{x}{\rho} \tag{B.4}$$

where $\xi_1 = x, \xi_2 = y,$ and $\xi_3 = s$ and $\rho = a$ curvature of the crack

4. Derivatives of physical components are calculated with respect to x and y are calculated with the chain rule:

$$\frac{du}{d\xi_1}=\frac{du}{dx}=\frac{du}{dr}\frac{dr}{dx}+\frac{du}{d\theta}\frac{d\theta}{dx}$$
$$\frac{du}{d\xi_2}=\frac{du}{dy}=\frac{du}{dr}\frac{dr}{dy}+\frac{du}{d\theta}\frac{d\theta}{dy} \tag{B.5}$$
$$\frac{du}{d\xi_3}=0$$

5. Derivatives of tensor components include calculation of unit vector derivatives w.r.t. ξ_1, ξ_2, and ξ_3.

$$\frac{\partial\hat{e}_1}{\partial\xi_3}=\frac{1}{h_1}\frac{\partial h_3}{\partial\xi_1}\hat{e}_3=\frac{\partial h_3}{\partial\xi_1}\hat{e}_3$$
$$\frac{\partial\hat{e}_2}{\partial\xi_3}=\frac{1}{h_2}\frac{\partial h_3}{\partial\xi_2}\hat{e}_3=0 \tag{B.6}$$
$$\frac{\partial\hat{e}_3}{\partial\xi_3}=\frac{1}{h_3}\frac{\partial h_3}{\partial\xi_3}\hat{e}_3=-\frac{1}{h_1}\frac{\partial h_3}{\partial\xi_1}\hat{e}_1-\frac{1}{h_2}\frac{\partial h_2}{\partial\xi_2}\hat{e}_2=-\frac{\partial h_3}{\partial\xi_1}\hat{e}_1$$

6. Calculation of the components in the auxiliary displacement gradient $\left(u^{aux}_{i,j}\right)$.

$$\left(\hat{e}_1\frac{1}{h_1}\frac{\partial}{\partial\xi_1}\right)\otimes\left(u_1^{aux}\hat{e}_1\right)=u^{aux}_{1,1}\hat{e}_1\hat{e}_1+\hat{e}_1u_1^{aux}\frac{\partial\hat{e}_1}{\partial\xi_1}=u^{aux}_{1,1}\hat{e}_1\hat{e}_1$$
$$\left(\hat{e}_2\frac{1}{h_2}\frac{\partial}{\partial\xi_2}\right)\otimes\left(u_1^{aux}\hat{e}_1\right)=u^{aux}_{1,2}\hat{e}_2\hat{e}_1+\hat{e}_2u_1^{aux}\frac{\partial\hat{e}_1}{\partial\xi_2}=u^{aux}_{1,2}\hat{e}_2\hat{e}_1$$
$$\left(\hat{e}_3\frac{1}{h_3}\frac{\partial}{\partial\xi_3}\right)\otimes\left(u_1^{aux}\hat{e}_1\right)=\frac{1}{h_3}\left(u^{aux}_{1,3}\hat{e}_3\hat{e}_1+\hat{e}_3u_1^{aux}\frac{\partial\hat{e}_1}{\partial\xi_3}\right)=\frac{1}{h_3}\left(u^{aux}_{1,3}\hat{e}_3\hat{e}_1+\hat{e}_3u_1^{aux}\frac{\partial h_3}{\partial\xi_1}\hat{e}_3\hat{e}_3\right) \tag{B.7}$$
$$\left(\hat{e}_3\frac{1}{h_3}\frac{\partial}{\partial\xi_3}\right)\otimes\left(u_1^{aux}\hat{e}_1\right)=\frac{u_1^{aux}}{h_3}\frac{\partial h_3}{\partial\xi_1}\hat{e}_3\hat{e}_3\hat{e}_3$$

$$\left(\hat{e}_1\frac{1}{h_1}\frac{\partial}{\partial\xi_1}\right)\otimes\left(u_2^{aux}\hat{e}_2\right)=u^{aux}_{2,1}\hat{e}_1\hat{e}_2+\hat{e}_1u_2^{aux}\frac{\partial\hat{e}_2}{\partial\xi_1}=u^{aux}_{2,1}\hat{e}_1\hat{e}_2$$
$$\left(\hat{e}_2\frac{1}{h_2}\frac{\partial}{\partial\xi_2}\right)\otimes\left(u_2^{aux}\hat{e}_2\right)=u^{aux}_{2,2}\hat{e}_2\hat{e}_2+\hat{e}_2u_2^{aux}\frac{\partial\hat{e}_2}{\partial\xi_2}=u^{aux}_{2,2}\hat{e}_2\hat{e}_2 \tag{B.8}$$
$$\left(\hat{e}_3\frac{1}{h_3}\frac{\partial}{\partial\xi_3}\right)\otimes\left(u_2^{aux}\hat{e}_2\right)=\frac{1}{h_3}\left(u^{aux}_{2,3}\hat{e}_3\hat{e}_2+\hat{e}_3u_2^{aux}\frac{\partial\hat{e}_2}{\partial\xi_3}\right)=0$$

$$\left(\hat{e}_1\frac{1}{h_1}\frac{\partial}{\partial\xi_1}\right)\otimes\left(u_3^{aux}\hat{e}_3\right)=\hat{e}_1\frac{1}{h_1}\left(\frac{\partial u_3^{aux}}{\partial\xi_1}\hat{e}_3+u_3^{aux}\frac{\partial\hat{e}_3}{\partial\xi_1}\right)=\frac{\partial u_3^{aux}}{\partial\xi_1}\hat{e}_1\hat{e}_3$$

$$\left(\hat{e}_2\frac{1}{h_2}\frac{\partial}{\partial\xi_2}\right)\otimes\left(u_3^{aux}\hat{e}_3\right)=\hat{e}_2\frac{1}{h_2}\left(\frac{\partial u_3^{aux}}{\partial\xi_2}\hat{e}_3+u_3^{aux}\frac{\partial\hat{e}_3}{\partial\xi_2}\right)=\frac{\partial u_3^{aux}}{\partial\xi_2}\hat{e}_2\hat{e}_3 \tag{B.9}$$

$$\left(\hat{e}_3\frac{1}{h_3}\frac{\partial}{\partial\xi_3}\right)\otimes\left(u_3^{aux}\hat{e}_3\right)=\hat{e}_3\frac{1}{h_3}\left(\frac{\partial u_3^{aux}}{\partial\xi_3}\hat{e}_3+u_3^{aux}\frac{\partial\hat{e}_3}{\partial\xi_3}\right)=-\frac{u_3^{aux}}{h_3}\frac{\partial h_3}{\partial\xi_1}\hat{e}_3\hat{e}_1$$

$$\left[\vec{\nabla}u^{aux}\right]=\begin{bmatrix} u_{1,1}^{aux} & u_{2,1}^{aux} & u_{3,1}^{aux} \\ u_{1,2}^{aux} & u_{2,2}^{aux} & u_{3,2}^{aux} \\ -\dfrac{u_3^{aux}h_{3,1}}{h_3} & 0 & \dfrac{u_1^{aux}h_{3,1}}{h_3} \end{bmatrix} \tag{B.10}$$

7. Calculation of the components in the gradients of the auxiliary displacement gradient $\left(u_{i,jk}^{aux}\right)$.

$$\left(\vec{\nabla}u^{aux}\right)\vec{\nabla}=(T_{ij}\hat{e}_i\hat{e}_j)\otimes\left(\frac{\partial}{\partial\xi_1}\frac{1}{h_1}\hat{e}_1+\frac{\partial}{\partial\xi_2}\frac{1}{h_2}\hat{e}_2+\frac{\partial}{\partial\xi_3}\frac{1}{h_3}\hat{e}_3\right) \tag{B.11}$$

$$\vec{\nabla}\left(T_{11}\hat{e}_1\hat{e}_1\right)=\vec{\nabla}\left(u_{1,1}^{aux}\hat{e}_1\hat{e}_1\right)$$

$$\left(u_{1,1}^{aux}\hat{e}_1\hat{e}_1\right)\otimes\left(\frac{\partial}{\partial\xi_1}\hat{e}_1\right)=u_{1,11}^{aux}\hat{e}_1\hat{e}_1\hat{e}_1+2u_{1,1}^{aux}\hat{e}_1\left(\frac{\partial\hat{e}_1}{\partial\xi_1}\right)=u_{1,11}^{aux}\hat{e}_1\hat{e}_1\hat{e}_1$$

$$\left(u_{1,1}^{aux}\hat{e}_1\hat{e}_1\right)\otimes\left(\frac{\partial}{\partial\xi_2}\hat{e}_2\right)=u_{1,12}^{aux}\hat{e}_1\hat{e}_1\hat{e}_2+u_{1,1}^{aux}\frac{\partial\hat{e}_1}{\partial\xi_2}\hat{e}_1\hat{e}_2+u_{1,1}^{aux}\hat{e}_1\frac{\partial\hat{e}_1}{\partial\xi_2}\hat{e}_2=u_{1,12}^{aux}\hat{e}_1\hat{e}_1\hat{e}_2$$

$$\left(u_{1,1}^{aux}\hat{e}_1\hat{e}_1\right)\otimes\left(\frac{\partial}{\partial\xi_3}\frac{1}{h_3}\hat{e}_3\right)=\frac{1}{h_3}u_{1,13}^{aux}\hat{e}_1\hat{e}_1\hat{e}_3+\frac{1}{h_3}u_{1,1}^{aux}\left[\frac{\partial\hat{e}_1}{\partial\xi_3}\hat{e}_1+\hat{e}_1\frac{\partial\hat{e}_1}{\partial\xi_3}\right]\hat{e}_3 \tag{B.12}$$

$$\left(u_{1,1}^{aux}\hat{e}_1\hat{e}_1\right)\otimes\left(\frac{\partial}{\partial\xi_3}\frac{1}{h_3}\hat{e}_3\right)=\frac{1}{h_3}u_{1,1}^{aux}\left[\frac{\partial h_3}{\partial\xi_1}\hat{e}_3\hat{e}_1+\frac{\partial h_3}{\partial\xi_1}\hat{e}_1\hat{e}_3\right]\hat{e}_3$$

$$\left(u_{1,1}^{aux}\hat{e}_1\hat{e}_1\right)\otimes\left(\frac{\partial}{\partial\xi_3}\frac{1}{h_3}\hat{e}_3\right)=\frac{u_{1,1}^{aux}h_{3,1}}{h_3}\hat{e}_3\hat{e}_1\hat{e}_3+\frac{u_{1,1}^{aux}h_{3,1}}{h_3}\hat{e}_1\hat{e}_3\hat{e}_3$$

$$\vec{\nabla}\left(T_{12}\hat{e}_1\hat{e}_2\right)=\vec{\nabla}\left(u_{2,1}^{aux}\hat{e}_1\hat{e}_2\right)$$

$$\left(u_{2,1}^{aux}\hat{e}_1\hat{e}_2\right)\otimes\left(\frac{\partial}{\partial\xi_1}\hat{e}_1\right)=u_{2,11}^{aux}\hat{e}_1\hat{e}_2\hat{e}_1+u_{2,1}^{aux}\left[\frac{\partial\hat{e}_1}{\partial\xi_1}\hat{e}_2+\hat{e}_1\frac{\partial\hat{e}_2}{\partial\xi_1}\right]\hat{e}_1=u_{2,11}^{aux}\hat{e}_1\hat{e}_2\hat{e}_1$$

$$\left(u_{2,1}^{aux}\hat{e}_1\hat{e}_2\right)\otimes\left(\frac{\partial}{\partial\xi_2}\hat{e}_2\right)=u_{2,12}^{aux}\hat{e}_1\hat{e}_2\hat{e}_2+u_{2,1}^{aux}\left[\frac{\partial\hat{e}_1}{\partial\xi_2}\hat{e}_2+\hat{e}_1\frac{\partial\hat{e}_2}{\partial\xi_2}\right]\hat{e}_2=u_{2,12}^{aux}\hat{e}_1\hat{e}_2\hat{e}_2 \qquad \text{(B.13)}$$

$$\left(u_{2,1}^{aux}\hat{e}_1\hat{e}_2\right)\otimes\left(\frac{\partial}{\partial\xi_3}\frac{1}{h_3}\hat{e}_3\right)=\frac{1}{h_3}\cancel{u_{2,13}^{aux}}\hat{e}_1\hat{e}_2\hat{e}_3+\frac{1}{h_3}u_{2,1}^{aux}\left[\frac{\partial\hat{e}_1}{\partial\xi_3}\hat{e}_2+\hat{e}_1\frac{\partial\hat{e}_2}{\partial\xi_3}\right]\hat{e}_3$$

$$\left(u_{2,1}^{aux}\hat{e}_1\hat{e}_2\right)\otimes\left(\frac{\partial}{\partial\xi_3}\frac{1}{h_3}\hat{e}_3\right)=\frac{1}{h_3}u_{2,1}^{aux}\left[\frac{\partial h_3}{\partial\xi_1}\hat{e}_3\hat{e}_2\right]\hat{e}_3=\frac{u_{2,1}^{aux}h_{3,1}}{h_3}\hat{e}_3\hat{e}_2\hat{e}_3$$

$$\vec{\nabla}\left(T_{31}\hat{e}_1\hat{e}_3\right)=\vec{\nabla}\left(u_{3,1}^{aux}\hat{e}_1\hat{e}_3\right)$$

$$\left(u_{3,1}^{aux}\hat{e}_1\hat{e}_3\right)\otimes\left(\frac{\partial}{\partial\xi_1}\hat{e}_1\right)=u_{3,11}^{aux}\hat{e}_1\hat{e}_3\hat{e}_1+u_{3,1}^{aux}\left(\frac{\partial\hat{e}_1}{\partial\xi_1}\hat{e}_3+\hat{e}_1\frac{\partial\hat{e}_3}{\partial\xi_1}\right)\hat{e}_1=u_{3,11}^{aux}\hat{e}_1\hat{e}_3\hat{e}_1$$

$$\left(u_{3,1}^{aux}\hat{e}_1\hat{e}_3\right)\otimes\left(\frac{\partial}{\partial\xi_2}\hat{e}_2\right)=u_{3,12}^{aux}\hat{e}_1\hat{e}_3\hat{e}_2+u_{3,1}^{aux}\left(\frac{\partial\hat{e}_1}{\partial\xi_2}\hat{e}_3+\hat{e}_1\frac{\partial\hat{e}_3}{\partial\xi_2}\right)\hat{e}_2=u_{3,12}^{aux}\hat{e}_1\hat{e}_3\hat{e}_2 \qquad \text{(B.14)}$$

$$\left(u_{3,1}^{aux}\hat{e}_1\hat{e}_3\right)\otimes\left(\frac{\partial}{\partial\xi_3}\frac{1}{h_3}\hat{e}_3\right)=\frac{1}{h_3}\cancel{u_{3,13}^{aux}}\hat{e}_1\hat{e}_3\hat{e}_3+\frac{u_{3,1}^{aux}}{h_3}\left(\frac{\partial\hat{e}_1}{\partial\xi_3}\hat{e}_3+\hat{e}_1\frac{\partial\hat{e}_3}{\partial\xi_3}\right)\hat{e}_3$$

$$\left(u_{3,1}^{aux}\hat{e}_1\hat{e}_3\right)\otimes\left(\frac{\partial}{\partial\xi_3}\frac{1}{h_3}\hat{e}_3\right)=\frac{u_{3,1}^{aux}}{h_3}\left(\frac{\partial h_3}{\partial\xi_1}\hat{e}_3\hat{e}_3-\hat{e}_1\frac{\partial h_3}{\partial\xi_1}\hat{e}_1\right)\hat{e}_3=\frac{u_{3,1}^{aux}h_{3,1}}{h_3}\left(\hat{e}_3\hat{e}_3\hat{e}_3-\hat{e}_1\hat{e}_1\hat{e}_3\right)$$

$$\vec{\nabla}\left(T_{21}\hat{e}_2\hat{e}_1\right)=\vec{\nabla}\left(u_{1,2}^{aux}\hat{e}_2\hat{e}_1\right)$$

$$\left(u_{1,2}^{aux}\hat{e}_2\hat{e}_1\right)\otimes\left(\frac{\partial}{\partial\xi_1}\hat{e}_1\right)=u_{1,21}^{aux}\hat{e}_2\hat{e}_1\hat{e}_1+u_{1,2}^{aux}\left[\frac{\partial\hat{e}_2}{\partial\xi_1}\hat{e}_1+\hat{e}_2\frac{\partial\hat{e}_1}{\partial\xi_1}\right]\hat{e}_1=u_{1,21}^{aux}\hat{e}_2\hat{e}_1\hat{e}_1$$

$$\left(u_{1,2}^{aux}\hat{e}_2\hat{e}_1\right)\otimes\left(\frac{\partial}{\partial\xi_2}\hat{e}_2\right)=u_{1,22}^{aux}\hat{e}_2\hat{e}_1\hat{e}_2+u_{1,2}^{aux}\left[\frac{\partial\hat{e}_2}{\partial\xi_2}\hat{e}_1+\hat{e}_2\frac{\partial\hat{e}_1}{\partial\xi_2}\right]\hat{e}_2=u_{1,22}^{aux}\hat{e}_2\hat{e}_1\hat{e}_2 \qquad \text{(B.15)}$$

$$\left(u_{1,2}^{aux}\hat{e}_2\hat{e}_1\right)\otimes\left(\frac{\partial}{\partial\xi_3}\frac{1}{h_3}\hat{e}_3\right)=\frac{1}{h_3}\cancel{u_{1,23}^{aux}}\hat{e}_2\hat{e}_1\hat{e}_3+\frac{1}{h_3}u_{1,2}^{aux}\left[\frac{\partial\hat{e}_2}{\partial\xi_3}\hat{e}_1+\hat{e}_2\frac{\partial\hat{e}_1}{\partial\xi_3}\right]\hat{e}_3$$

$$\left(u_{1,2}^{aux}\hat{e}_2\hat{e}_1\right)\otimes\left(\frac{\partial}{\partial\xi_3}\frac{1}{h_3}\hat{e}_3\right)=\frac{1}{h_3}u_{1,2}^{aux}\left[\frac{\partial h_3}{\partial\xi_1}\hat{e}_2\hat{e}_3\right]\hat{e}_3=\frac{u_{1,2}^{aux}h_{3,1}}{h_3}\hat{e}_2\hat{e}_3\hat{e}_3$$

$$\vec{\nabla}\left(T_{22}\hat{e}_2\hat{e}_2\right)=\vec{\nabla}\left(u^{aux}_{2,2}\hat{e}_2\hat{e}_2\right)$$

$$\left(u^{aux}_{2,2}\hat{e}_2\hat{e}_2\right)\otimes\left(\frac{\partial}{\partial\xi_1}\hat{e}_1\right)=u^{aux}_{2,21}\hat{e}_2\hat{e}_2\hat{e}_1+u^{aux}_{2,2}\left[\frac{\partial\hat{e}_2}{\partial\xi_1}\hat{e}_2+\hat{e}_2\frac{\partial\hat{e}_2}{\partial\xi_1}\right]\hat{e}_1=u^{aux}_{2,21}\hat{e}_2\hat{e}_2\hat{e}_1$$

$$\left(u^{aux}_{2,2}\hat{e}_2\hat{e}_2\right)\otimes\left(\frac{\partial}{\partial\xi_2}\hat{e}_2\right)=u^{aux}_{2,22}\hat{e}_2\hat{e}_2\hat{e}_2+u^{aux}_{2,2}\frac{\partial\hat{e}_2}{\partial\xi_2}\hat{e}_2\hat{e}_2+u^{aux}_{2,2}\hat{e}_2\frac{\partial\hat{e}_2}{\partial\xi_2}\hat{e}_2=u^{aux}_{2,22}\hat{e}_2\hat{e}_2\hat{e}_2 \tag{B.16}$$

$$\left(u^{aux}_{2,2}\hat{e}_2\hat{e}_2\right)\otimes\left(\frac{\partial}{\partial\xi_3}\frac{1}{h_3}\hat{e}_3\right)=\frac{1}{h_3}u^{aux}_{2,23}\hat{e}_2\hat{e}_2\hat{e}_3+\frac{1}{h_3}u^{aux}_{2,2}\left[\frac{\partial\hat{e}_2}{\partial\xi_3}\hat{e}_2+\hat{e}_2\frac{\partial\hat{e}_2}{\partial\xi_3}\right]\hat{e}_3=0$$

$$\vec{\nabla}\left(T_{32}\hat{e}_2\hat{e}_3\right)=\vec{\nabla}\left(u^{aux}_{3,2}\hat{e}_2\hat{e}_3\right)$$

$$\left(u^{aux}_{3,2}\hat{e}_2\hat{e}_3\right)\otimes\left(\frac{\partial}{\partial\xi_1}\hat{e}_1\right)=u^{aux}_{3,21}\hat{e}_2\hat{e}_3\hat{e}_1+u^{aux}_{3,2}\left[\frac{\partial\hat{e}_2}{\partial\xi_1}\hat{e}_3+\hat{e}_2\frac{\partial\hat{e}_3}{\partial\xi_1}\right]\hat{e}_1=u^{aux}_{3,21}\hat{e}_2\hat{e}_3\hat{e}_1$$

$$\left(u^{aux}_{3,2}\hat{e}_2\hat{e}_3\right)\otimes\left(\frac{\partial}{\partial\xi_2}\hat{e}_2\right)=u^{aux}_{3,22}\hat{e}_2\hat{e}_3\hat{e}_2+u^{aux}_{3,2}\left[\frac{\partial\hat{e}_2}{\partial\xi_2}\hat{e}_3+\hat{e}_2\frac{\partial\hat{e}_3}{\partial\xi_2}\right]\hat{e}_2=u^{aux}_{3,22}\hat{e}_2\hat{e}_3\hat{e}_2 \tag{B.17}$$

$$\left(u^{aux}_{3,2}\hat{e}_2\hat{e}_3\right)\otimes\left(\frac{\partial}{\partial\xi_3}\frac{1}{h_3}\hat{e}_3\right)=\frac{1}{h_3}u^{aux}_{3,23}\hat{e}_2\hat{e}_3\hat{e}_3+\frac{1}{h_3}u^{aux}_{3,2}\left[\frac{\partial\hat{e}_2}{\partial\xi_3}\hat{e}_3+\hat{e}_2\frac{\partial\hat{e}_3}{\partial\xi_3}\right]\hat{e}_3$$

$$\left(u^{aux}_{3,2}\hat{e}_2\hat{e}_3\right)\otimes\left(\frac{\partial}{\partial\xi_3}\frac{1}{h_3}\hat{e}_3\right)=\frac{1}{h_3}u^{aux}_{3,2}\left[-\hat{e}_2\frac{\partial h_3}{\partial\xi_1}\hat{e}_1\right]\hat{e}_3=-\frac{u^{aux}_{3,2}h_{3,1}}{h_3}\hat{e}_2\hat{e}_1\hat{e}_3$$

$$\vec{\nabla}\left(T_{31}\hat{e}_3\hat{e}_1\right)=\vec{\nabla}\left(-\frac{u^{aux}_3h_{3,1}}{h_3}\hat{e}_3\hat{e}_1\right)$$

$$\left(-\frac{u^{aux}_3h_{3,1}}{h_3}\hat{e}_3\hat{e}_1\right)\otimes\left(\frac{\partial}{\partial\xi_1}\hat{e}_1\right)=\left[-u^{aux}_{3,1}\frac{h_{3,1}}{h_3}-u^{aux}_3\frac{h_{3,11}}{h_3}-u^{aux}_3h_{3,1}\left(h_3^{-1}\right)_{,1}\right]\hat{e}_3\hat{e}_1\hat{e}_1$$
$$-\frac{u^{aux}_3h_{3,1}}{h_3}\left[\frac{\partial\hat{e}_3}{\partial\xi_1}\hat{e}_1+\hat{e}_3\frac{\partial\hat{e}_1}{\partial\xi_1}\right]\hat{e}_1 \tag{B.18}$$

$$\left(-\frac{u^{aux}_3h_{3,1}}{h_3}\hat{e}_3\hat{e}_1\right)\otimes\left(\frac{\partial}{\partial\xi_1}\hat{e}_1\right)=\left[-\frac{u^{aux}_{3,1}h_{3,1}}{h_3}-\frac{u^{aux}_3h_{3,11}}{h_3}+\frac{u^{aux}_3h^2_{3,1}}{h_3^2}\right]\hat{e}_1\hat{e}_3\hat{e}_1$$

$$\left(-\frac{u_3^{aux}h_{3,1}}{h_3}\hat{e}_3\hat{e}_1\right)\otimes\left(\frac{\partial}{\partial\xi_2}\hat{e}_2\right)=-u_3^{aux}h_{3,1}\cancel{\left(h_3^{-1}\right)_{,2}}\hat{e}_3\hat{e}_3\hat{e}_2$$

$$-\frac{1}{h_3}\left[u_{3,2}^{aux}h_{3,1}\hat{e}_3\hat{e}_1+u_3^{aux}\cancel{h_{3,12}}\hat{e}_3\hat{e}_1+u_3^{aux}h_{3,1}\left(\cancel{\frac{\partial\hat{e}_3}{\partial\xi_2}}\hat{e}_1+\hat{e}_3\cancel{\frac{\partial\hat{e}_1}{\partial\xi_2}}\right)\right]\hat{e}_2$$

$$\left(-\frac{u_3^{aux}h_{3,1}}{h_3}\hat{e}_3\hat{e}_3\right)\otimes\left(\frac{\partial}{\partial\xi_2}\hat{e}_2\right)=-\frac{u_{3,2}^{aux}h_{3,1}}{h_3}\hat{e}_3\hat{e}_1\hat{e}_2$$

$$\left(-\frac{u_3^{aux}h_{3,1}}{h_3}\hat{e}_3\hat{e}_1\right)\otimes\left(\frac{\partial}{\partial\xi_3}\frac{1}{h_3}\hat{e}_3\right)=-\frac{u_3^{aux}h_{3,1}}{h_3}\cancel{\left(h_3^{-1}\right)_{,3}}\hat{e}_3\hat{e}_3\hat{e}_3$$

$$-\frac{1}{h_3^2}\left[\cancel{u_{3,3}^{aux}}h_{3,1}\hat{e}_3\hat{e}_3+u_3^{aux}\cancel{h_{3,13}}\hat{e}_3\hat{e}_3+u_3^{aux}h_{3,1}\left(\frac{\partial\hat{e}_3}{\partial\xi_3}\hat{e}_1+\hat{e}_3\frac{\partial\hat{e}_1}{\partial\xi_3}\right)\right]\hat{e}_3$$

$$\left(-\frac{u_3^{aux}h_{3,1}}{h_3}\hat{e}_3\hat{e}_1\right)\otimes\left(\frac{\partial}{\partial\xi_3}\frac{1}{h_3}\hat{e}_3\right)=\frac{u_3^{aux}h_{3,1}^2}{h_3^2}\hat{e}_1\hat{e}_1\hat{e}_3-\frac{u_3^{aux}h_{3,1}^2}{h_3^2}\hat{e}_3\hat{e}_3\hat{e}_3$$

$$\vec{\nabla}\left(T_{32}\hat{e}_2\hat{e}_3\right)=\vec{\nabla}\left(0\cdot\hat{e}_2\hat{e}_3\right)=0 \tag{B.19}$$

$$\vec{\nabla}\left(T_{33}\hat{e}_3\hat{e}_3\right)=\vec{\nabla}\left(\frac{u_1^{aux}h_{3,1}}{h_3}\hat{e}_3\hat{e}_3\right)$$

$$\left(\frac{u_1^{aux}h_{3,1}}{h_3}\hat{e}_3\hat{e}_3\right)\otimes\left(\frac{\partial}{\partial\xi_1}\hat{e}_1\right)=u_1^{aux}h_{3,1}\left(h_3^{-1}\right)_{,1}\hat{e}_3\hat{e}_3\hat{e}_1$$

$$+\frac{1}{h_3}\left[\left(u_{1,1}^{aux}h_{3,1}+u_1^{aux}h_{3,11}\right)\hat{e}_3\hat{e}_3+u_1^{aux}h_{3,1}\left(\cancel{\frac{\partial\hat{e}_3}{\partial\xi_1}}\hat{e}_3+\hat{e}_3\cancel{\frac{\partial\hat{e}_3}{\partial\xi_1}}\right)\right]\hat{e}_1 \tag{B.20}$$

$$\left(\frac{u_1^{aux}h_{3,1}}{h_3}\hat{e}_3\hat{e}_3\right)\otimes\left(\frac{\partial}{\partial\xi_1}\hat{e}_1\right)=\left[-\frac{u_1^{aux}h_{3,1}^2}{h_3^2}+\frac{u_{1,1}^{aux}h_{3,1}}{h_3}+\frac{u_1^{aux}h_{3,11}}{h_3}\right]\hat{e}_3\hat{e}_3\hat{e}_1$$

$$\left(\frac{u_1^{aux}h_{3,1}}{h_3}\hat{e}_3\hat{e}_3\right)\otimes\left(\frac{\partial}{\partial\xi_2}\hat{e}_2\right)=u_1^{aux}h_{3,1}\cancel{\left(h_3^{-1}\right)_{,2}}\hat{e}_3\hat{e}_3\hat{e}_2$$
$$+\frac{1}{h_3}\left[u_{1,2}^{aux}h_{3,1}\hat{e}_3\hat{e}_3+u_1^{aux}\cancel{h_{3,12}}\hat{e}_3\hat{e}_3+u_1^{aux}h_{3,1}\left(\cancel{\frac{\partial\hat{e}_3}{\partial\xi_2}}\hat{e}_3+\hat{e}_3\cancel{\frac{\partial\hat{e}_3}{\partial\xi_2}}\right)\right]\hat{e}_2$$
$$\left(\frac{u_1^{aux}h_{3,1}}{h_3}\hat{e}_3\hat{e}_3\right)\otimes\left(\frac{\partial}{\partial\xi_2}\hat{e}_2\right)=\frac{u_{1,2}^{aux}h_{3,1}}{h_3}\hat{e}_3\hat{e}_3\hat{e}_2$$
$$\left(\frac{u_1^{aux}h_{3,1}}{h_3}\hat{e}_3\hat{e}_3\right)\otimes\left(\frac{\partial}{\partial\xi_3}\frac{1}{h_3}\hat{e}_3\right)=\frac{u_1^{aux}h_{3,1}}{h_3}\cancel{\left(h_3^{-1}\right)_{,3}}\hat{e}_3\hat{e}_3\hat{e}_3$$
$$+\frac{1}{h_3^2}\left[\cancel{u_{1,3}^{aux}}h_{3,1}\hat{e}_3\hat{e}_3+u_1^{aux}\cancel{h_{3,13}}\hat{e}_3\hat{e}_3+u_1^{aux}h_{3,1}\left(\frac{\partial\hat{e}_3}{\partial\xi_3}\hat{e}_3+\hat{e}_3\frac{\partial\hat{e}_3}{\partial\xi_3}\right)\right]\hat{e}_3$$
$$\left(\frac{u_1^{aux}h_{3,1}}{h_3}\hat{e}_3\hat{e}_3\right)\otimes\left(\frac{\partial}{\partial\xi_3}\frac{1}{h_3}\hat{e}_3\right)=\frac{u_1^{aux}h_{3,1}}{h_3^2}\left(\frac{-\partial h_3}{\partial\xi_1}\hat{e}_1\hat{e}_3+\hat{e}_3\frac{-\partial h_3}{\partial\xi_3}\hat{e}_1\right)\hat{e}_3$$
$$\left(\frac{u_1^{aux}h_{3,1}}{h_3}\hat{e}_3\hat{e}_3\right)\otimes\left(\frac{\partial}{\partial\xi_3}\frac{1}{h_3}\hat{e}_3\right)=\frac{-u_1^{aux}\left(h_{3,1}\right)^2}{h_3^2}\hat{e}_1\hat{e}_3\hat{e}_3+\frac{-u_1^{aux}\left(h_{3,1}\right)^2}{h_3^2}\hat{e}_3\hat{e}_1\hat{e}_3$$

$$\begin{bmatrix}\hat{e}_1\hat{e}_1\hat{e}_1 & \hat{e}_1\hat{e}_2\hat{e}_1 & \hat{e}_1\hat{e}_3\hat{e}_1\\ \hat{e}_2\hat{e}_1\hat{e}_1 & \hat{e}_2\hat{e}_2\hat{e}_1 & \hat{e}_2\hat{e}_3\hat{e}_1\\ \hat{e}_3\hat{e}_1\hat{e}_1 & \hat{e}_3\hat{e}_2\hat{e}_1 & \hat{e}_3\hat{e}_3\hat{e}_1\end{bmatrix}\Rightarrow$$

$$\begin{bmatrix} & u_{1,11}^{aux} & u_{2,11}^{aux} & u_{3,11}^{aux} & \\ & u_{1,21}^{aux} & u_{2,21}^{aux} & u_{3,21}^{aux} & \\ \dfrac{u_3^{aux}h_{3,1}^2}{h_3^2}-\dfrac{u_{3,1}^{aux}h_{3,1}}{h_3}-\dfrac{u_3^{aux}h_{3,11}}{h_3} & & 0 & & \dfrac{u_{1,1}^{aux}h_{3,1}}{h_3}-\dfrac{u_1^{aux}h_{3,1}^2}{h_3^2}+\dfrac{u_1^{aux}h_{3,11}}{h_3}\end{bmatrix} \qquad \text{(B.21)}$$

$$\begin{bmatrix}\hat{e}_1\hat{e}_1\hat{e}_2 & \hat{e}_1\hat{e}_2\hat{e}_2 & \hat{e}_1\hat{e}_3\hat{e}_2\\ \hat{e}_2\hat{e}_1\hat{e}_2 & \hat{e}_2\hat{e}_2\hat{e}_2 & \hat{e}_2\hat{e}_3\hat{e}_2\\ \hat{e}_3\hat{e}_1\hat{e}_2 & \hat{e}_3\hat{e}_2\hat{e}_2 & \hat{e}_3\hat{e}_3\hat{e}_2\end{bmatrix}\Rightarrow\begin{bmatrix} u_{1,12}^{aux} & u_{2,12}^{aux} & u_{3,12}^{aux}\\ u_{1,22}^{aux} & u_{2,22}^{aux} & u_{3,22}^{aux}\\ -\dfrac{u_{3,2}^{aux}h_{3,1}}{h_3} & 0 & \dfrac{u_{1,2}^{aux}h_{3,1}}{h_3}\end{bmatrix} \qquad \text{(B.22)}$$

$$\begin{bmatrix} \hat{e}_1\hat{e}_1\hat{e}_3 & \hat{e}_1\hat{e}_2\hat{e}_3 & \hat{e}_1\hat{e}_3\hat{e}_3 \\ \hat{e}_2\hat{e}_1\hat{e}_3 & \hat{e}_2\hat{e}_2\hat{e}_3 & \hat{e}_2\hat{e}_3\hat{e}_3 \\ \hat{e}_3\hat{e}_1\hat{e}_3 & \hat{e}_3\hat{e}_2\hat{e}_3 & \hat{e}_3\hat{e}_3\hat{e}_3 \end{bmatrix} \Rightarrow$$

$$\frac{1}{h_3^2}\begin{bmatrix} h_{3,1}\left(u_3^{aux}h_{3,1} - u_{3,1}^{aux}h_3\right) & 0 & h_{3,1}\left(u_{1,1}^{aux}h_3 - u_1^{aux}h_{3,1}\right) \\ -u_{3,2}^{aux}h_{3,1}h_3 & 0 & u_{1,2}^{aux}h_{3,1}h_3 \\ h_{3,1}\left(u_{1,1}^{aux}h_3 - u_1^{aux}h_{3,1}\right) & u_{2,1}h_{3,1}h_3 & h_{3,1}\left(u_{3,1}^{aux}h_3 - u_3^{aux}h_{3,1}\right) \end{bmatrix} \tag{B.23}$$

8. Calculation of the physical strain components.

$$\begin{aligned} \varepsilon_{11} &= u_{1,1}^{aux} = u_{1,1}^{aux}\hat{e}_1\hat{e}_1 \\ \varepsilon_{22} &= u_{2,2}^{aux} = u_{2,2}^{aux}\hat{e}_2\hat{e}_2 \\ \varepsilon_{33} &= u_{3,3}^{aux} = 0 \\ \varepsilon_{12} &= \frac{1}{2}\left(u_{1,2}^{aux} + u_{2,1}^{aux}\right) = \frac{1}{2}\left(u_{1,2}^{aux}\hat{e}_2\hat{e}_1 + u_{2,1}^{aux}\hat{e}_1\hat{e}_2\right) \\ \varepsilon_{13} &= \frac{1}{2}\left(\cancel{u_{1,3}^{aux}} + u_{3,1}^{aux}\right) = \frac{1}{2}u_{3,1}^{aux}\hat{e}_3\hat{e}_1 \\ \varepsilon_{23} &= \frac{1}{2}\left(\cancel{u_{2,3}^{aux}} + u_{3,2}^{aux}\right) = \frac{1}{2}u_{3,2}^{aux}\hat{e}_3\hat{e}_2 \end{aligned} \tag{B.24}$$

$$\varepsilon^{aux} = \begin{bmatrix} u_{1,1}^{aux} & \frac{1}{2}\left(u_{1,2}^{aux} + u_{2,1}^{aux}\right) & \frac{1}{2}u_{3,1}^{aux} \\ \frac{1}{2}\left(u_{1,2}^{aux} + u_{2,1}^{aux}\right) & u_{2,2}^{aux} & \frac{1}{2}u_{3,2}^{aux} \\ \frac{1}{2}u_{3,1}^{aux} & \frac{1}{2}u_{3,2}^{aux} & 0 \end{bmatrix} \tag{B.25}$$

9. Calculation of gradient strain $\left(\varepsilon_{mn,j}^{aux}\right)$.

$$\varepsilon_{11}^{aux}\hat{e}_1\hat{e}_1 = u_{1,1}^{aux}\hat{e}_1\hat{e}_1$$

$$\left(u_{1,1}^{aux}\hat{e}_1\hat{e}_1\right)\otimes\left(\frac{\partial}{\partial\xi_1}\hat{e}_1\right) = u_{1,11}^{aux}\hat{e}_1\hat{e}_1\hat{e}_1$$

$$\left(u_{1,1}^{aux}\hat{e}_1\hat{e}_1\right)\otimes\left(\frac{\partial}{\partial\xi_2}\hat{e}_2\right) = u_{1,12}^{aux}\hat{e}_1\hat{e}_1\hat{e}_2$$

$$\left(u_{1,1}^{aux}\hat{e}_1\hat{e}_1\right)\otimes\left(\frac{\partial}{\partial\xi_3}\frac{1}{h_3}\hat{e}_3\right) = \frac{1}{h_3}\left[\cancel{u_{1,13}^{aux}\hat{e}_1\hat{e}_1} + u_{1,1}^{aux}\frac{\partial\hat{e}_1}{\partial\xi_3}\hat{e}_1 + u_{1,1}^{aux}\hat{e}_1\frac{\partial\hat{e}_1}{\partial\xi_3}\right]\hat{e}_3 \qquad \text{(B.26)}$$

$$\left(u_{1,1}^{aux}\hat{e}_1\hat{e}_1\right)\otimes\left(\frac{\partial}{\partial\xi_3}\frac{1}{h_3}\hat{e}_3\right) = \frac{1}{h_3}\left[u_{1,1}^{aux}h_{3,1}\hat{e}_3\hat{e}_1 + u_{1,1}^{aux}h_{3,1}\hat{e}_1\hat{e}_3\right]\hat{e}_3 =$$

$$\left(u_{1,1}^{aux}\hat{e}_1\hat{e}_1\right)\otimes\left(\frac{\partial}{\partial\xi_3}\frac{1}{h_3}\hat{e}_3\right) = \frac{u_{1,1}^{aux}h_{3,1}}{h_3}\hat{e}_3\hat{e}_1\hat{e}_3 + \frac{u_{1,1}^{aux}h_{3,1}}{h_3}\hat{e}_1\hat{e}_3\hat{e}_3$$

$$\varepsilon_{12}^{aux}\hat{e}_1\hat{e}_2 = \frac{1}{2}\left(u_{1,2}^{aux} + u_{2,1}^{aux}\right)\hat{e}_1\hat{e}_2$$

$$\left(\frac{1}{2}\left(u_{1,2}^{aux} + u_{2,1}^{aux}\right)\hat{e}_1\hat{e}_2\right)\otimes\left(\frac{\partial}{\partial\xi_1}\hat{e}_1\right) = \frac{1}{2}\left[u_{1,21}^{aux}\hat{e}_1\hat{e}_2\hat{e}_1 + u_{2,11}^{aux}\hat{e}_1\hat{e}_2\hat{e}_1\right] = \frac{1}{2}\left(u_{1,21}^{aux} + u_{2,11}^{aux}\right)\hat{e}_1\hat{e}_2\hat{e}_1 \qquad \text{(B.27)}$$

$$\left(\frac{1}{2}\left(u_{1,2}^{aux} + u_{2,1}^{aux}\right)\hat{e}_1\hat{e}_2\right)\otimes\left(\frac{\partial}{\partial\xi_2}\hat{e}_2\right) = \frac{1}{2}\left[u_{1,22}^{aux}\hat{e}_1\hat{e}_2\hat{e}_2 + u_{2,12}^{aux}\hat{e}_1\hat{e}_2\hat{e}_2\right] = \frac{1}{2}\left(u_{1,22}^{aux} + u_{2,12}^{aux}\right)\hat{e}_1\hat{e}_2\hat{e}_2$$

$$\left(\frac{1}{2}\left(u_{1,2}^{aux} + u_{2,1}^{aux}\right)\hat{e}_1\hat{e}_2\right)\otimes\left(\frac{\partial}{\partial\xi_3}\frac{1}{h_3}\hat{e}_3\right)$$

$$= \frac{1}{2h_3}\cancel{\left(u_{1,2}^{aux} + u_{2,1}^{aux}\right)_{,3}}\hat{e}_1\hat{e}_2\hat{e}_3 + \frac{1}{2h_3}\left(u_{1,2}^{aux} + u_{2,1}^{aux}\right)\frac{\partial\hat{e}_1}{\partial\xi_3}\hat{e}_2\hat{e}_3 + \frac{1}{2h_3}\left(u_{1,2}^{aux} + u_{2,1}^{aux}\right)\hat{e}_1\cancel{\frac{\partial\hat{e}_2}{\partial\xi_3}}\hat{e}_3 \qquad \text{(B.27 cont.)}$$

$$\left(\varepsilon_{12}^{aux}\hat{e}_1\hat{e}_2\right)\otimes\left(\frac{\partial}{\partial\xi_3}\frac{1}{h_3}\hat{e}_3\right) = \frac{1}{2h_3}\left[\left(u_{1,2}^{aux} + u_{2,1}^{aux}\right)\frac{\partial\hat{e}_1}{\partial\xi_3}\hat{e}_2\right]\hat{e}_3$$

$$\left(\varepsilon_{12}^{aux}\hat{e}_1\hat{e}_2\right)\otimes\left(\frac{\partial}{\partial\xi_3}\frac{1}{h_3}\hat{e}_3\right) = \frac{h_{3,1}}{2h_3}\left(u_{1,2}^{aux} + u_{2,1}^{aux}\right)\hat{e}_3\hat{e}_2\hat{e}_3$$

$$\varepsilon_{21}^{aux}\hat{e}_2\hat{e}_1 = \frac{1}{2}\left(u_{1,2}^{aux} + u_{2,1}^{aux}\right)\hat{e}_2\hat{e}_1$$

$$\left(\frac{1}{2}\left(u_{1,2}^{aux} + u_{2,1}^{aux}\right)\hat{e}_2\hat{e}_1\right)\otimes\left(\frac{\partial}{\partial\xi_1}\hat{e}_1\right) = \frac{1}{2}\left[u_{1,21}^{aux}\hat{e}_2\hat{e}_1\hat{e}_1 + u_{2,11}^{aux}\hat{e}_2\hat{e}_1\hat{e}_1\right] = \frac{1}{2}\left(u_{1,21}^{aux} + u_{2,11}^{aux}\right)\hat{e}_2\hat{e}_1\hat{e}_1 \qquad \text{(B.28)}$$

$$\left(\frac{1}{2}\left(u_{1,2}^{aux} + u_{2,1}^{aux}\right)\hat{e}_2\hat{e}_1\right)\otimes\left(\frac{\partial}{\partial\xi_2}\hat{e}_2\right) = \frac{1}{2}\left[u_{1,22}^{aux}\hat{e}_2\hat{e}_1\hat{e}_2 + u_{2,12}^{aux}\hat{e}_2\hat{e}_1\hat{e}_2\right] = \frac{1}{2}\left(u_{1,22}^{aux} + u_{2,12}^{aux}\right)\hat{e}_2\hat{e}_1\hat{e}_2$$

$$\left(\frac{1}{2}\left(u_{1,2}^{aux}+u_{2,1}^{aux}\right)\hat{e}_2\hat{e}_1\right)\otimes\left(\frac{\partial}{\partial\xi_3}\frac{1}{h_3}\hat{e}_3\right)$$

$$=\frac{1}{2h_3}\cancel{\left(u_{1,2}^{aux}+u_{2,1}^{aux}\right)_{,3}}\hat{e}_2\hat{e}_1\hat{e}_3+\frac{1}{2h_3}\left(u_{1,2}^{aux}+u_{2,1}^{aux}\right)\cancel{\frac{\partial\hat{e}_2}{\partial\xi_3}}\hat{e}_1\hat{e}_3+\frac{1}{2h_3}\left(u_{1,2}^{aux}+u_{2,1}^{aux}\right)\hat{e}_2\frac{\partial\hat{e}_1}{\partial\xi_3}\hat{e}_3$$

$$\left(\varepsilon_{12}^{aux}\hat{e}_1\hat{e}_2\right)\otimes\left(\frac{\partial}{\partial\xi_3}\frac{1}{h_3}\hat{e}_3\right)=\frac{1}{2h_3}\left[\left(u_{1,2}^{aux}+u_{2,1}^{aux}\right)\hat{e}_2\frac{\partial\hat{e}_1}{\partial\xi_3}\right]\hat{e}_3=\frac{h_{3,1}}{2h_3}\left(u_{1,2}^{aux}+u_{2,1}^{aux}\right)\hat{e}_2\hat{e}_3\hat{e}_3$$

$$\varepsilon_{13}^{aux}\hat{e}_1\hat{e}_3=\frac{1}{2}u_{3,1}^{aux}\hat{e}_1\hat{e}_3$$

$$\left(\frac{1}{2}u_{3,1}^{aux}\hat{e}_1\hat{e}_3\right)\otimes\left(\frac{\partial}{\partial\xi_1}\hat{e}_1\right)=\frac{1}{2}u_{3,11}^{aux}\hat{e}_1\hat{e}_3\hat{e}_1$$

$$\left(\frac{1}{2}u_{3,1}^{aux}\hat{e}_1\hat{e}_3\right)\otimes\left(\frac{\partial}{\partial\xi_2}\hat{e}_2\right)=\frac{1}{2}u_{3,12}^{aux}\hat{e}_1\hat{e}_3\hat{e}_2 \qquad \text{(B.29)}$$

$$\left(\frac{1}{2}u_{3,1}^{aux}\hat{e}_1\hat{e}_3\right)\otimes\left(\frac{\partial}{\partial\xi_3}\frac{1}{h_3}\hat{e}_3\right)=\frac{1}{2h_3}\left[\cancel{u_{3,13}^{aux}}\hat{e}_1\hat{e}_3+u_{3,1}^{aux}\frac{\partial\hat{e}_1}{\partial\xi_3}\hat{e}_3+u_{3,1}^{aux}\hat{e}_1\frac{\partial\hat{e}_3}{\partial\xi_3}\right]\hat{e}_3$$

$$\left(\frac{1}{2}u_{3,1}^{aux}\hat{e}_1\hat{e}_3\right)\otimes\left(\frac{\partial}{\partial\xi_3}\frac{1}{h_3}\hat{e}_3\right)=\frac{1}{2h_3}\left[u_{3,1}^{aux}h_{3,1}\hat{e}_3\hat{e}_3-u_{3,1}^{aux}h_{3,1}\hat{e}_1\hat{e}_1\right]\hat{e}_3=\frac{u_{3,1}^{aux}h_{3,1}}{2h_3}\hat{e}_3\hat{e}_3\hat{e}_3-\frac{u_{3,1}^{aux}h_{3,1}}{2h_3}\hat{e}_1\hat{e}_1\hat{e}_3$$

$$\varepsilon_{31}^{aux}\hat{e}_3\hat{e}_1=\frac{1}{2}u_{3,1}^{aux}\hat{e}_3\hat{e}_1$$

$$\left(\frac{1}{2}u_{3,1}^{aux}\hat{e}_3\hat{e}_1\right)\otimes\left(\frac{\partial}{\partial\xi_1}\hat{e}_1\right)=\frac{1}{2}u_{3,11}^{aux}\hat{e}_3\hat{e}_1\hat{e}_1$$

$$\left(\frac{1}{2}u_{3,1}^{aux}\hat{e}_3\hat{e}_1\right)\otimes\left(\frac{\partial}{\partial\xi_2}\hat{e}_2\right)=\frac{1}{2}u_{3,12}^{aux}\hat{e}_3\hat{e}_1\hat{e}_2 \qquad \text{(B.30)}$$

$$\left(\frac{1}{2}u_{3,1}^{aux}\hat{e}_3\hat{e}_1\right)\otimes\left(\frac{\partial}{\partial\xi_3}\frac{1}{h_3}\hat{e}_3\right)=\frac{1}{2h_3}\left[\cancel{u_{3,13}^{aux}}\hat{e}_3\hat{e}_1+u_{3,1}^{aux}\frac{\partial\hat{e}_3}{\partial\xi_3}\hat{e}_1+u_{3,1}^{aux}\hat{e}_3\frac{\partial\hat{e}_1}{\partial\xi_3}\right]\hat{e}_3$$

$$\left(\frac{1}{2}u_{3,1}^{aux}\hat{e}_3\hat{e}_1\right)\otimes\left(\frac{\partial}{\partial\xi_3}\frac{1}{h_3}\hat{e}_3\right)=\frac{1}{2h_3}\left[-u_{3,1}^{aux}h_{3,1}\hat{e}_1\hat{e}_1+u_{3,1}^{aux}h_{3,1}\hat{e}_3\hat{e}_3\right]\hat{e}_3=\frac{u_{3,1}^{aux}h_{3,1}}{2h_3}\hat{e}_3\hat{e}_3\hat{e}_3-\frac{u_{3,1}^{aux}h_{3,1}}{2h_3}\hat{e}_1\hat{e}_1\hat{e}_3$$

$$\varepsilon_{22}^{aux}\hat{e}_2\hat{e}_2=u_{2,2}^{aux}\hat{e}_2\hat{e}_2$$

$$\left(u_{2,2}^{aux}\hat{e}_2\hat{e}_2\right)\otimes\left(\frac{\partial}{\partial\xi_1}\hat{e}_1\right)=u_{2,21}^{aux}\hat{e}_2\hat{e}_2\hat{e}_1$$

$$\left(u_{2,2}^{aux}\hat{e}_2\hat{e}_2\right)\otimes\left(\frac{\partial}{\partial\xi_2}\hat{e}_2\right)=u_{2,22}^{aux}\hat{e}_2\hat{e}_2\hat{e}_2 \qquad \text{(B.31)}$$

$$\left(u_{2,2}^{aux}\hat{e}_2\hat{e}_2\right)\otimes\left(\frac{\partial}{\partial\xi_3}\frac{1}{h_3}\hat{e}_3\right)=\frac{1}{h_3}\left[\cancel{u_{2,23}^{aux}}\hat{e}_2\hat{e}_2+u_{2,2}^{aux}\cancel{\frac{\partial\hat{e}_2}{\partial\xi_3}}\hat{e}_2+u_{2,2}^{aux}\hat{e}_2\cancel{\frac{\partial\hat{e}_2}{\partial\xi_3}}\right]\hat{e}_3=0$$

$$\varepsilon_{23}^{aux}\hat{e}_2\hat{e}_3 = \frac{1}{2}u_{3,2}^{aux}\hat{e}_2\hat{e}_3$$

$$\left(\frac{1}{2}u_{3,2}^{aux}\hat{e}_2\hat{e}_3\right)\otimes\left(\frac{\partial}{\partial\xi_1}\hat{e}_1\right) = \frac{1}{2}u_{3,21}^{aux}\hat{e}_2\hat{e}_3\hat{e}_1$$

$$\left(\frac{1}{2}u_{3,2}^{aux}\hat{e}_2\hat{e}_3\right)\otimes\left(\frac{\partial}{\partial\xi_2}\hat{e}_2\right) = \frac{1}{2}u_{3,22}^{aux}\hat{e}_2\hat{e}_3\hat{e}_2 \qquad \text{(B.32)}$$

$$\left(\frac{1}{2}u_{3,2}^{aux}\hat{e}_2\hat{e}_3\right)\otimes\left(\frac{\partial}{\partial\xi_3}\frac{1}{h_3}\hat{e}_3\right) = \frac{1}{2h_3}\left[\cancel{u_{3,23}^{aux}}\hat{e}_2\hat{e}_3 + u_{3,2}^{aux}\cancel{\frac{\partial\hat{e}_2}{\partial\xi_3}}\hat{e}_3 + u_{3,2}^{aux}\hat{e}_2\frac{\partial\hat{e}_3}{\partial\xi_3}\right]\hat{e}_3$$

$$\left(\frac{1}{2}u_{3,1}^{aux}\hat{e}_1\hat{e}_3\right)\otimes\left(\frac{\partial}{\partial\xi_3}\frac{1}{h_3}\hat{e}_3\right) = -\frac{u_{3,2}^{aux}h_{3,1}}{2h_3}\hat{e}_2\hat{e}_1\hat{e}_3$$

$$\varepsilon_{32}^{aux}\hat{e}_3\hat{e}_2 = \frac{1}{2}u_{3,2}^{aux}\hat{e}_3\hat{e}_2$$

$$\left(\frac{1}{2}u_{3,2}^{aux}\hat{e}_3\hat{e}_2\right)\otimes\left(\frac{\partial}{\partial\xi_1}\hat{e}_1\right) = \frac{1}{2}u_{3,21}^{aux}\hat{e}_3\hat{e}_2\hat{e}_1$$

$$\left(\frac{1}{2}u_{3,2}^{aux}\hat{e}_3\hat{e}_2\right)\otimes\left(\frac{\partial}{\partial\xi_2}\hat{e}_2\right) = \frac{1}{2}u_{3,22}^{aux}\hat{e}_3\hat{e}_2\hat{e}_2 \qquad \text{(B.33)}$$

$$\left(\frac{1}{2}u_{3,2}^{aux}\hat{e}_3\hat{e}_2\right)\otimes\left(\frac{\partial}{\partial\xi_3}\frac{1}{h_3}\hat{e}_3\right) = \frac{1}{2h_3}\left[\cancel{u_{3,23}^{aux}}\hat{e}_3\hat{e}_2 + u_{3,2}^{aux}\hat{e}_3\cancel{\frac{\partial\hat{e}_2}{\partial\xi_3}} + u_{3,2}^{aux}\frac{\partial\hat{e}_3}{\partial\xi_3}\hat{e}_2\right]\hat{e}_3$$

$$\left(\frac{1}{2}u_{3,1}^{aux}\hat{e}_1\hat{e}_3\right)\otimes\left(\frac{\partial}{\partial\xi_3}\frac{1}{h_3}\hat{e}_3\right) = -\frac{u_{3,2}^{aux}h_{3,1}}{2h_3}\hat{e}_1\hat{e}_2\hat{e}_3$$

$$\varepsilon_{33}^{aux}\hat{e}_3\hat{e}_3 = 0\hat{e}_3\hat{e}_3 \qquad \text{(B.34)}$$

$$\begin{bmatrix} \hat{e}_1\hat{e}_1\hat{e}_1 & \hat{e}_1\hat{e}_2\hat{e}_1 & \hat{e}_1\hat{e}_3\hat{e}_1 \\ \hat{e}_2\hat{e}_1\hat{e}_1 & \hat{e}_2\hat{e}_2\hat{e}_1 & \hat{e}_2\hat{e}_3\hat{e}_1 \\ \hat{e}_3\hat{e}_1\hat{e}_1 & \hat{e}_3\hat{e}_2\hat{e}_1 & \hat{e}_3\hat{e}_3\hat{e}_1 \end{bmatrix} \Rightarrow$$

$$\frac{1}{2}\begin{bmatrix} 2u_{1,11}^{aux} & \left(u_{1,21}^{aux}+u_{2,11}^{aux}\right) & u_{3,11}^{aux} \\ \left(u_{1,21}^{aux}+u_{2,11}^{aux}\right) & 2u_{2,21}^{aux} & u_{3,21}^{aux} \\ u_{3,11}^{aux} & u_{3,21}^{aux} & 0 \end{bmatrix} \qquad \text{(B.35)}$$

$$\begin{bmatrix} \hat{e}_1\hat{e}_1\hat{e}_2 & \hat{e}_1\hat{e}_2\hat{e}_2 & \hat{e}_1\hat{e}_3\hat{e}_2 \\ \hat{e}_2\hat{e}_1\hat{e}_2 & \hat{e}_2\hat{e}_2\hat{e}_2 & \hat{e}_2\hat{e}_3\hat{e}_2 \\ \hat{e}_3\hat{e}_1\hat{e}_2 & \hat{e}_3\hat{e}_2\hat{e}_2 & \hat{e}_3\hat{e}_3\hat{e}_2 \end{bmatrix} \Rightarrow$$

$$\frac{1}{2}\begin{bmatrix} 2u_{1,12}^{aux} & \left(u_{1,22}^{aux}+u_{2,12}^{aux}\right) & u_{3,12}^{aux} \\ \left(u_{1,22}^{aux}+u_{2,12}^{aux}\right) & 2u_{2,22}^{aux} & u_{3,22}^{aux} \\ u_{3,12}^{aux} & u_{3,22}^{aux} & 0 \end{bmatrix} \tag{B.36}$$

$$\begin{bmatrix} \hat{e}_1\hat{e}_1\hat{e}_3 & \hat{e}_1\hat{e}_2\hat{e}_3 & \hat{e}_1\hat{e}_3\hat{e}_3 \\ \hat{e}_2\hat{e}_1\hat{e}_3 & \hat{e}_2\hat{e}_2\hat{e}_3 & \hat{e}_2\hat{e}_3\hat{e}_3 \\ \hat{e}_3\hat{e}_1\hat{e}_3 & \hat{e}_3\hat{e}_2\hat{e}_3 & \hat{e}_3\hat{e}_3\hat{e}_3 \end{bmatrix} \Rightarrow$$

$$\begin{bmatrix} -\frac{u_{3,1}^{aux}h_{3,1}}{2h_3} & -\frac{u_{3,2}^{aux}h_{3,1}}{2h_3} & \frac{u_{1,1}^{aux}h_{3,1}}{h_3} \\ -\frac{u_{3,2}^{aux}h_{3,1}}{2h_3} & 0 & \frac{h_{3,1}}{2h_3}\left(u_{1,2}^{aux}+u_{2,1}^{aux}\right) \\ \frac{u_{1,1}^{aux}h_{3,1}}{h_3} & \frac{h_{3,1}}{2h_3}\left(u_{1,2}^{aux}+u_{2,1}^{aux}\right) & \frac{u_{3,1}^{aux}h_{3,1}}{2h_3} \end{bmatrix} \tag{B.37}$$

10. The auxiliary stress $\left(\sigma_{ij}^{aux}\right)$ is calculated as follows:

$$\begin{bmatrix} \sigma_{11}^{aux} \\ \sigma_{22}^{aux} \\ \sigma_{33}^{aux} \\ \sigma_{12}^{aux} \\ \sigma_{13}^{aux} \\ \sigma_{23}^{aux} \end{bmatrix} = \frac{2\mu}{1-2\nu}\begin{bmatrix} 1-\nu & \nu & \nu & 0 & 0 & 0 \\ \nu & 1-\nu & \nu & 0 & 0 & 0 \\ \nu & \nu & 1-\nu & 0 & 0 & 0 \\ 0 & 0 & 0 & 1-2\nu & 0 & 0 \\ 0 & 0 & 0 & 0 & 1-2\nu & 0 \\ 0 & 0 & 0 & 0 & 0 & 1-2\nu \end{bmatrix}\begin{bmatrix} \varepsilon_{11}^{aux} \\ \varepsilon_{22}^{aux} \\ \varepsilon_{33}^{aux} \\ \varepsilon_{12}^{aux} \\ \varepsilon_{13}^{aux} \\ \varepsilon_{23}^{aux} \end{bmatrix} \tag{B.38}$$

11. Divergence of the auxiliary stress is calculated as follows:

$$\left(\vec{\nabla}\bullet\sigma_{i1}\right)=\frac{1}{h_1h_2h_3}\left[\frac{\partial}{\partial\xi_1}\left(h_2h_3\sigma_{11}\right)+\frac{\partial}{\partial\xi_2}\left(h_1h_3\sigma_{21}\right)+\frac{\partial}{\partial\xi_3}\left(h_1h_2\sigma_{31}\right)\right]$$

$$\left(\vec{\nabla}\bullet\sigma_{i1}\right)=\frac{1}{h_3}\left[\frac{\partial}{\partial\xi_1}\left(h_3\sigma_{11}\right)+\frac{\partial}{\partial\xi_2}\left(h_3\sigma_{21}\right)+\cancel{\frac{\partial}{\partial\xi_3}\left(\sigma_{31}\right)}\right]$$

$$\left(\vec{\nabla}\bullet\sigma_{i1}\right)=\frac{1}{h_3}\left[\sigma_{11}\frac{\partial h_3}{\partial\xi_1}+h_3\frac{\partial\sigma_{11}}{\partial\xi_1}+\sigma_{12}\cancel{\frac{\partial h_3}{\partial\xi_2}}+h_3\frac{\partial\sigma_{21}}{\partial\xi_2}\right] \qquad \text{(B.39)}$$

$$\sigma_{i1,i}=\left[\frac{\sigma_{11}}{h_3}\frac{\partial h_3}{\partial\xi_1}+\frac{\partial\sigma_{11}}{\partial\xi_1}+\frac{\partial\sigma_{21}}{\partial\xi_2}\right]$$

$$\left(\vec{\nabla}\bullet\sigma_{i2}\right)=\frac{1}{h_1h_2h_3}\left[\frac{\partial}{\partial\xi_1}\left(h_2h_3\sigma_{12}\right)+\frac{\partial}{\partial\xi_2}\left(h_1h_3\sigma_{22}\right)+\frac{\partial}{\partial\xi_3}\left(h_1h_2\sigma_{32}\right)\right]$$

$$\left(\vec{\nabla}\bullet\sigma_{i2}\right)=\frac{1}{h_3}\left[\frac{\partial}{\partial\xi_1}\left(h_3\sigma_{12}\right)+\frac{\partial}{\partial\xi_2}\left(h_3\sigma_{22}\right)+\cancel{\frac{\partial}{\partial\xi_3}\left(\sigma_{32}\right)}\right]$$

$$\left(\vec{\nabla}\bullet\sigma_{i2}\right)=\frac{1}{h_3}\left[\sigma_{12}\frac{\partial h_3}{\partial\xi_1}+h_3\frac{\partial\sigma_{12}}{\partial\xi_1}+\sigma_{22}\cancel{\frac{\partial h_3}{\partial\xi_2}}+h_3\frac{\partial\sigma_{22}}{\partial\xi_2}\right] \qquad \text{(B.40)}$$

$$\sigma_{i2,i}=\left[\frac{\sigma_{12}}{h_3}\frac{\partial h_3}{\partial\xi_1}+\frac{\partial\sigma_{12}}{\partial\xi_1}+\frac{\partial\sigma_{22}}{\partial\xi_2}\right]$$

$$\left(\vec{\nabla}\bullet\sigma_{i3}\right)=\frac{1}{h_1h_2h_3}\left[\frac{\partial}{\partial\xi_1}\left(h_2h_3\cancel{\sigma_{13}}\right)+\frac{\partial}{\partial\xi_2}\left(h_1h_3\cancel{\sigma_{23}}\right)+\frac{\partial}{\partial\xi_3}\left(h_1h_2\sigma_{33}\right)\right] \qquad \text{(B.41)}$$

$$\sigma_{i3,i}=\frac{1}{h_3}\left[\cancel{\frac{\partial\sigma_{33}}{\partial\xi_3}}\right]=0$$

APPENDIX C. CONTOUR PLOTS

The following section provides contour plots for the three dimensional finite element models. Each model analyzed has a plot of the deformed shape, Sigma x, and Sigma xy. A sigma x contour plot of the volume surrounding the crack tip is also included. The most refined mesh used is shown for each model.

List of Contour Plots

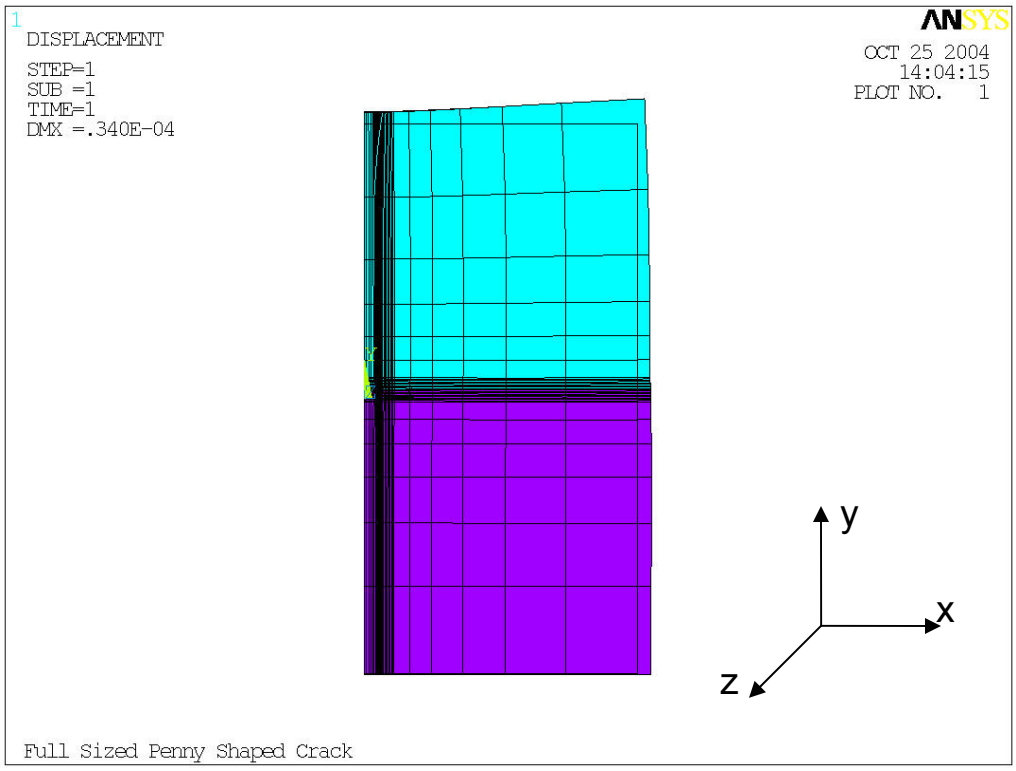

Figure C-1: Deformed shape of bimaterial mechanical stress penny shaped crack.

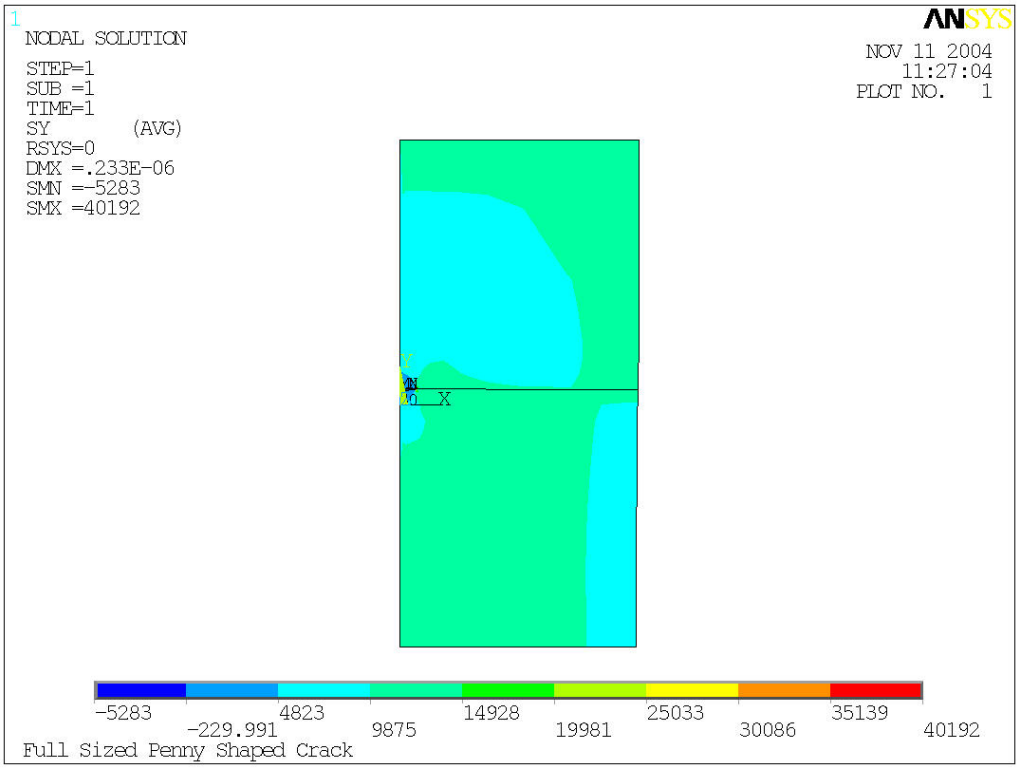

Figure C-2: Sigma y (MPa) of bimaterial mechanical stress penny shaped crack.

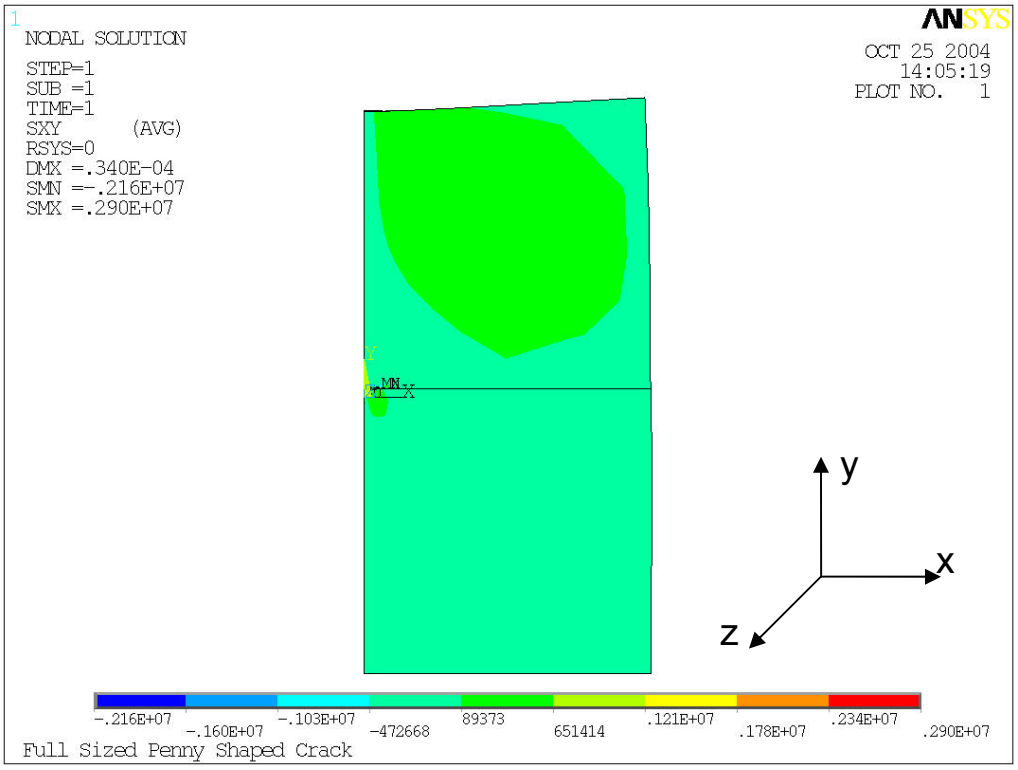

Figure C-3: Sigma xy (MPa) of bimaterial mechanical stress penny shaped crack.

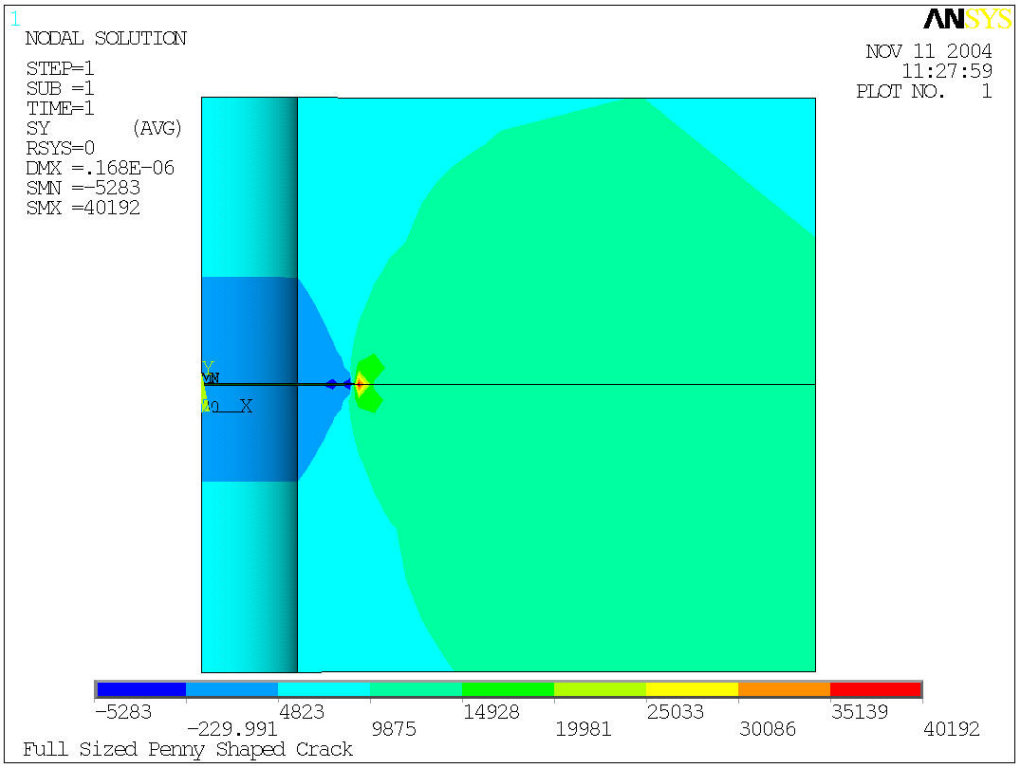

Figure C-4: Sigma y (MPa) of volume surrounding penny shaped crack.

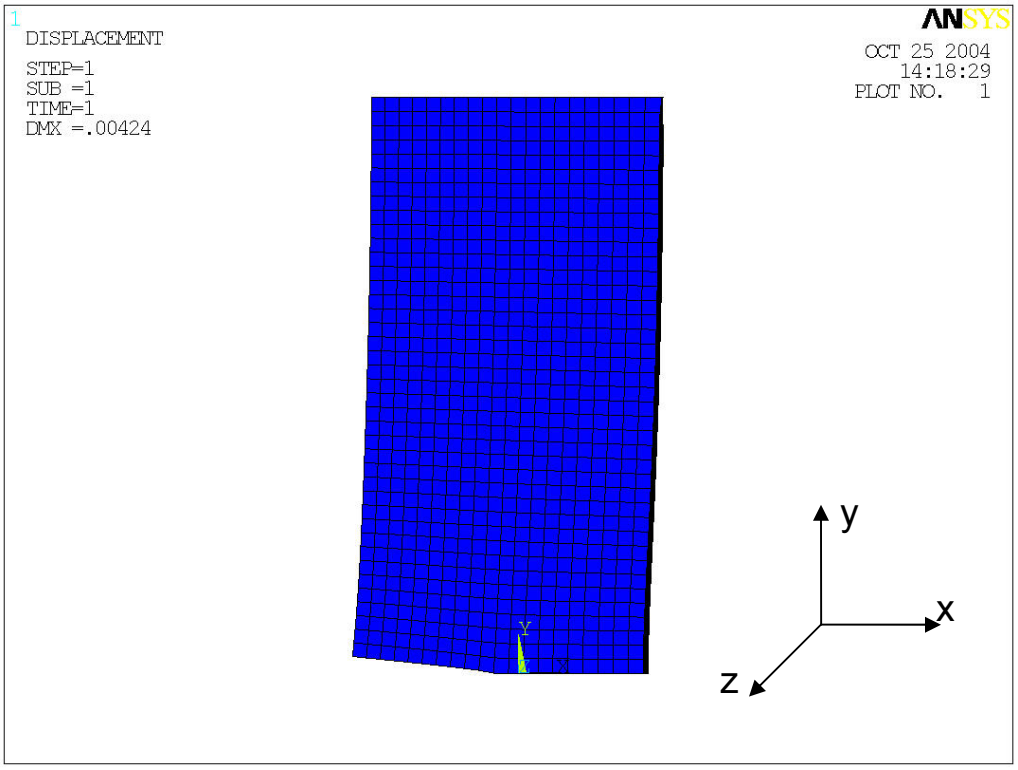

Figure C-5: Deformed shape of homogenous plane strain thermal crack.

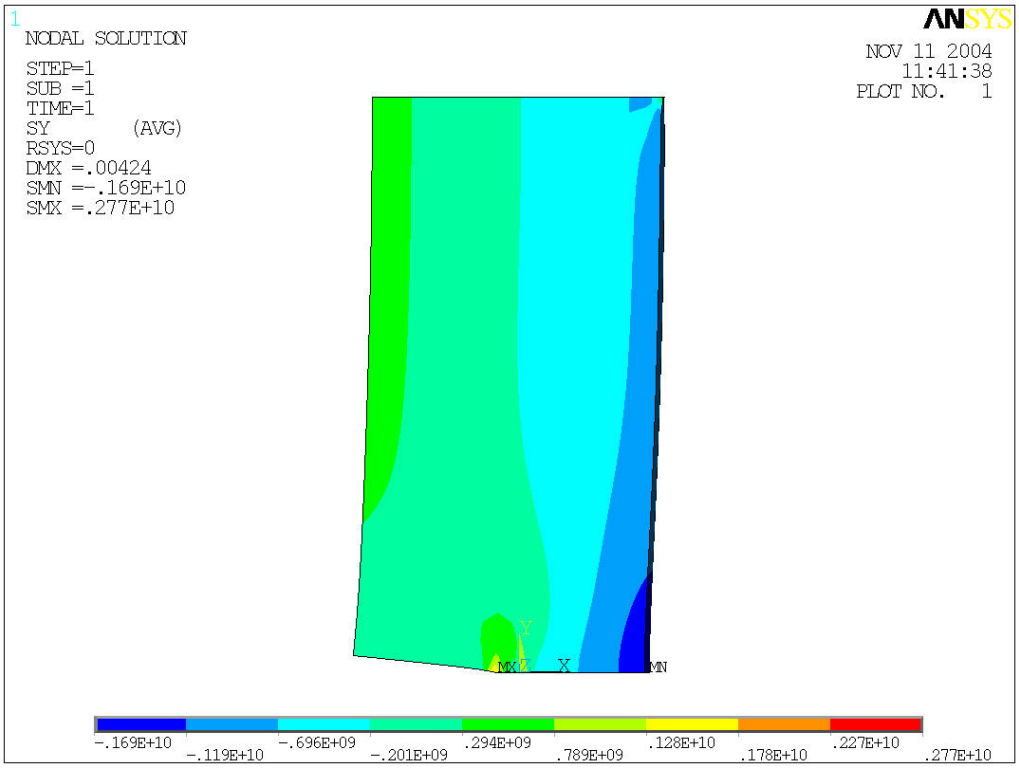

Figure C-6: Sigma y (MPa) of homogenous plane strain thermal crack.

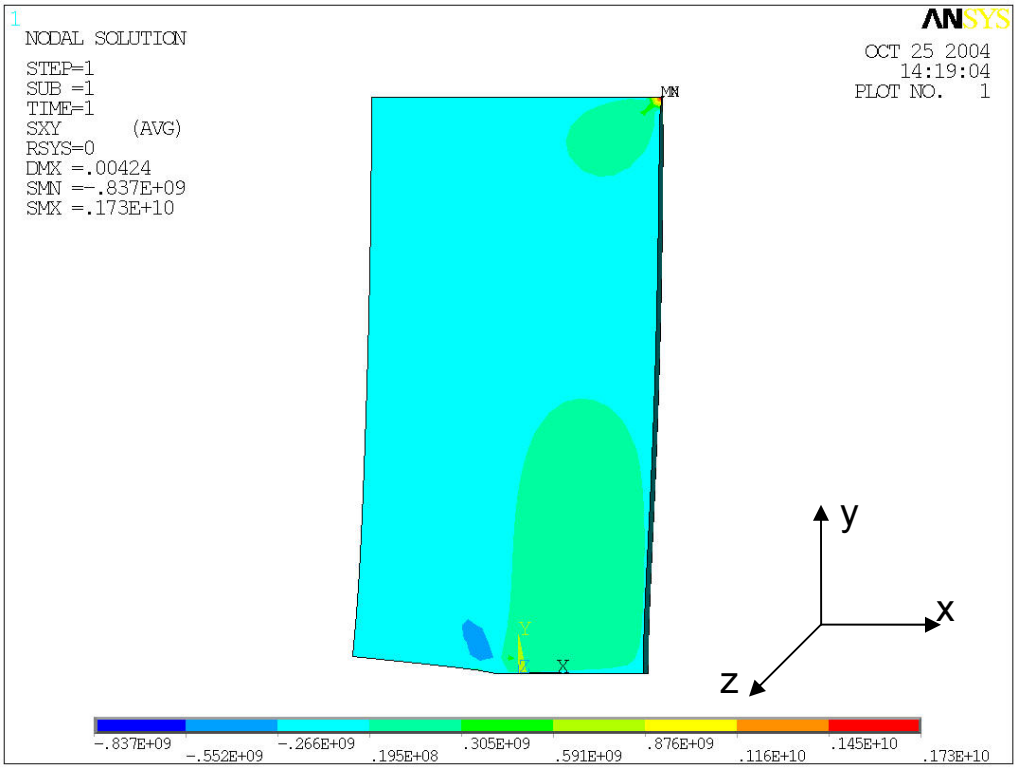

Figure C-7: Sigma xy (MPa) of homogenous plane strain thermal crack.

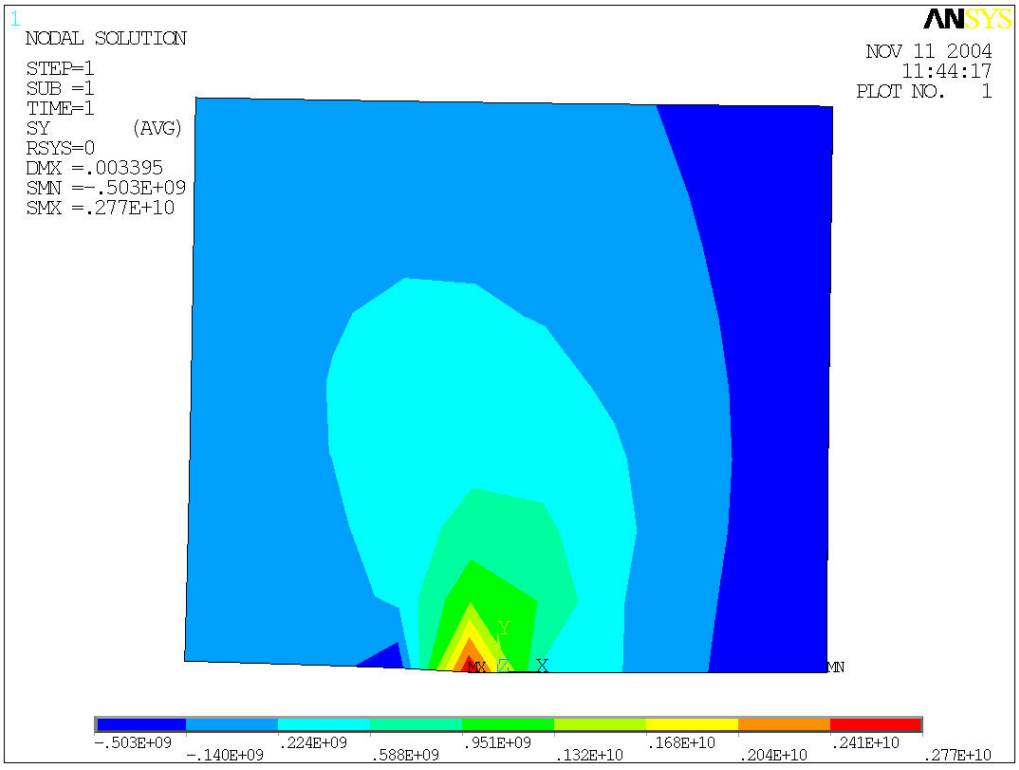

Figure C-8: Sigma y (MPa) of volume near crack tip.

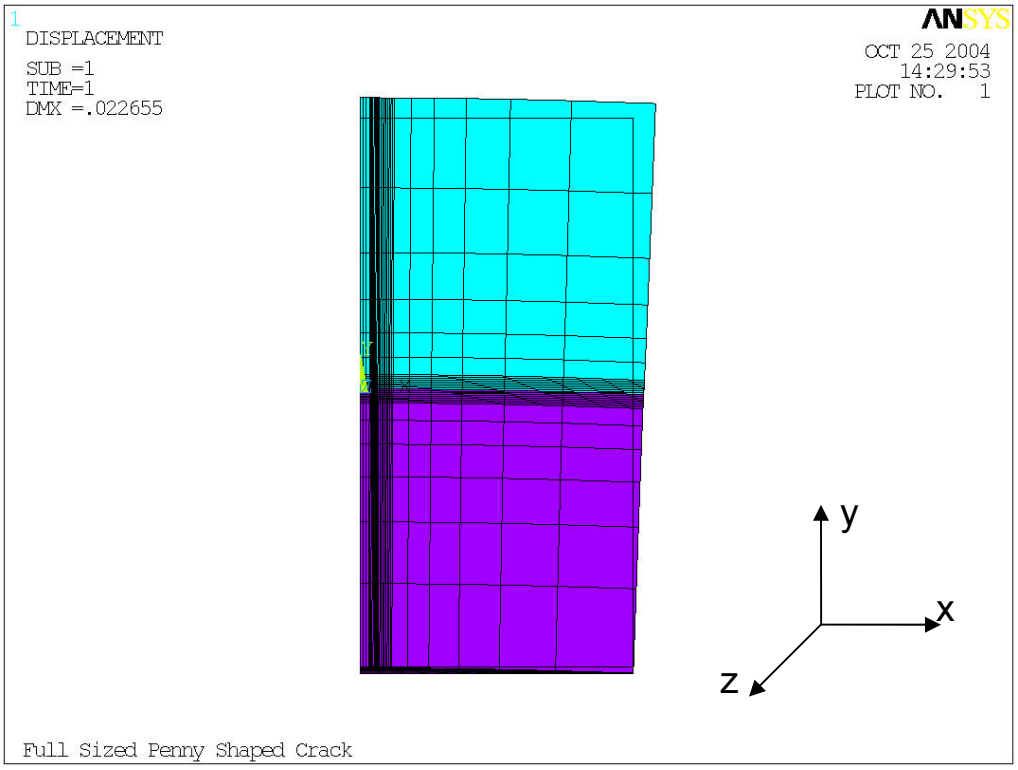

Figure C-9: The deformed shape of an orthogonal temperature gradient.

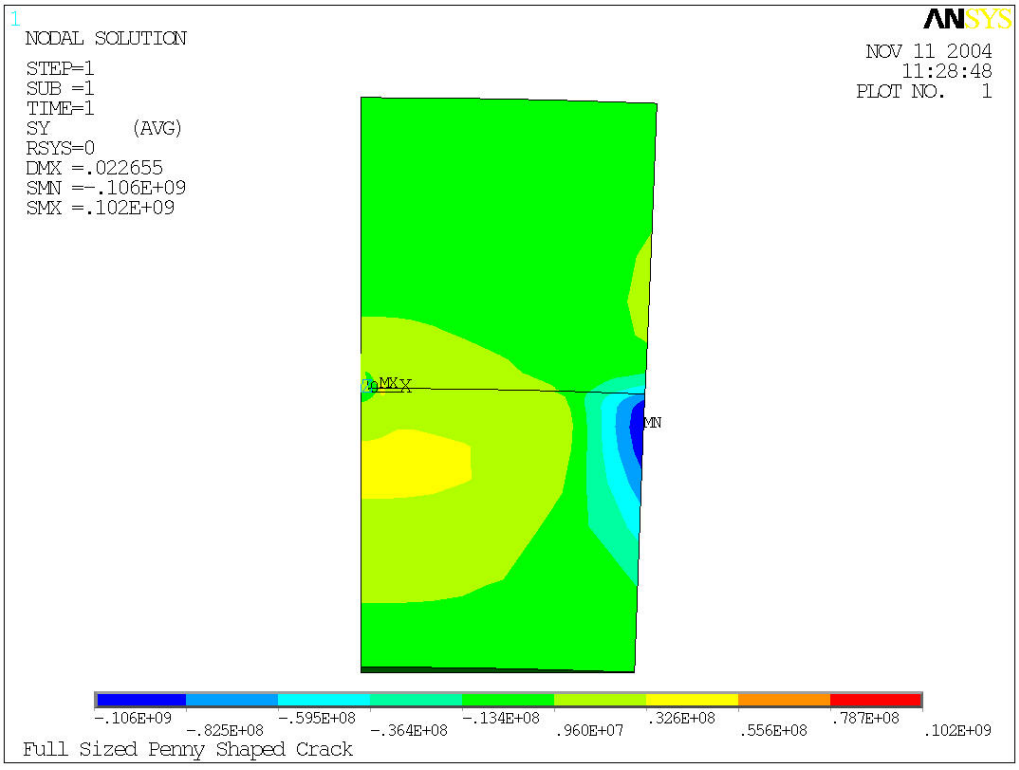

Figure C-10: Sigma y (MPa) of an orthogonal temperature gradient to the crack.

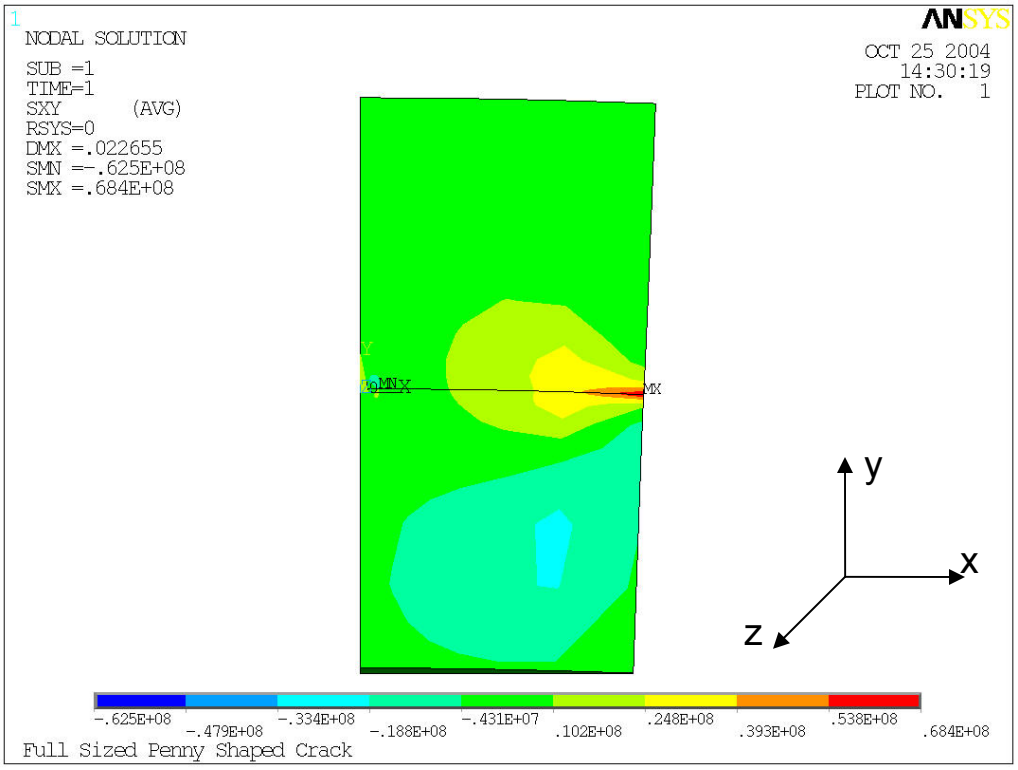

Figure C-11: Sigma xy (MPa) of an orthogonal temperature gradient to the crack.

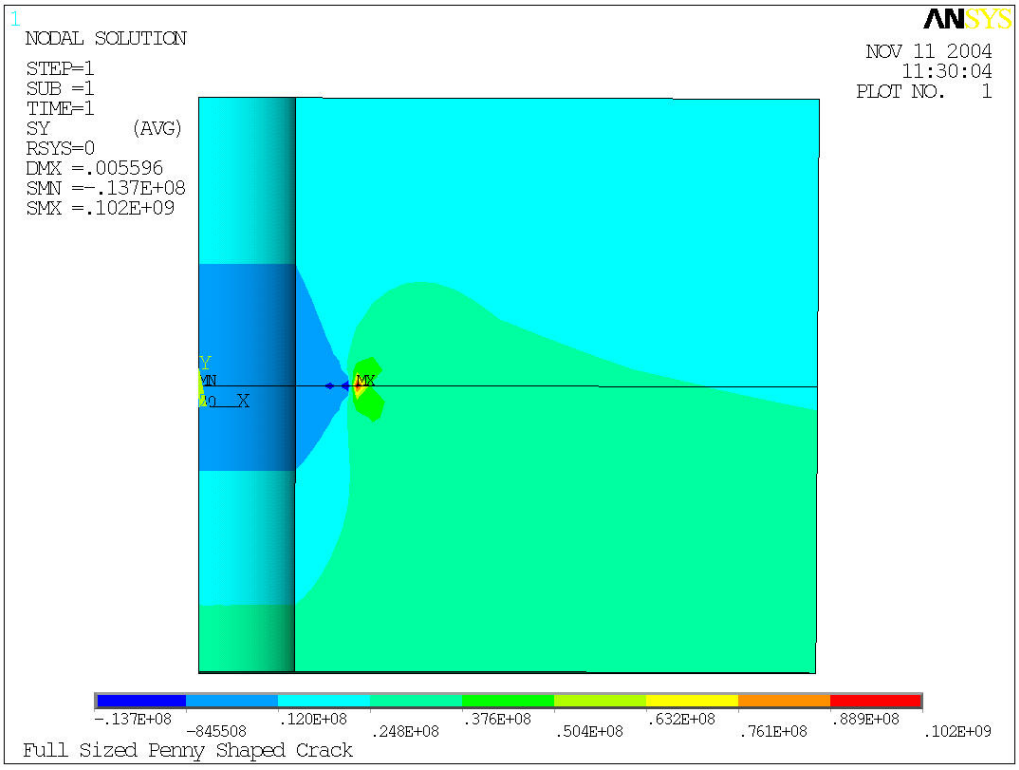

Figure C-12: Sigma y (MPa) near a crack with an orthogonal temperature gradient.

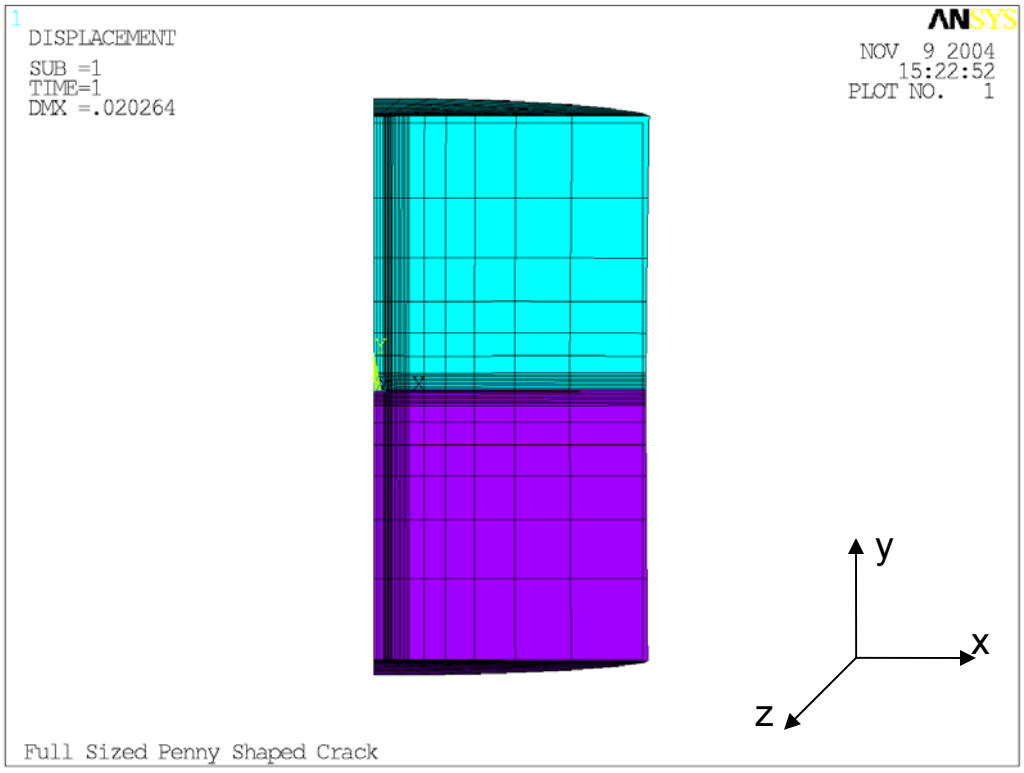

Figure C- 13: The deformed shape with parallel thermal gradient to crack plane.

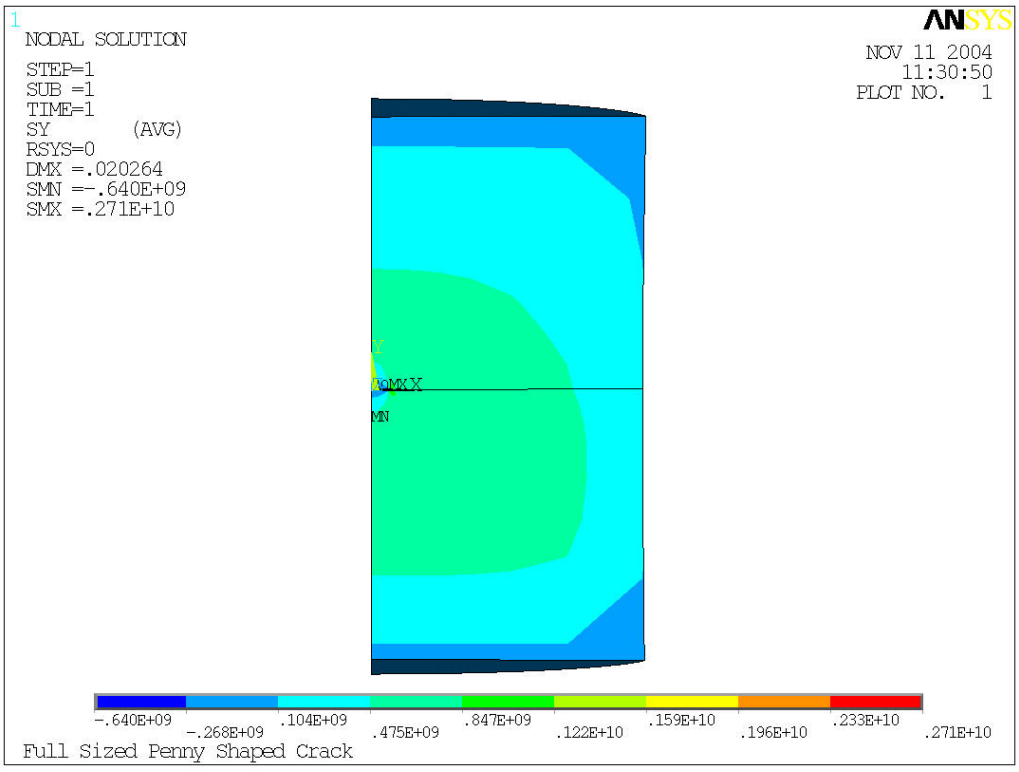

Figure C- 14: Sigma y (MPa) of crack with parallel temperature gradient.

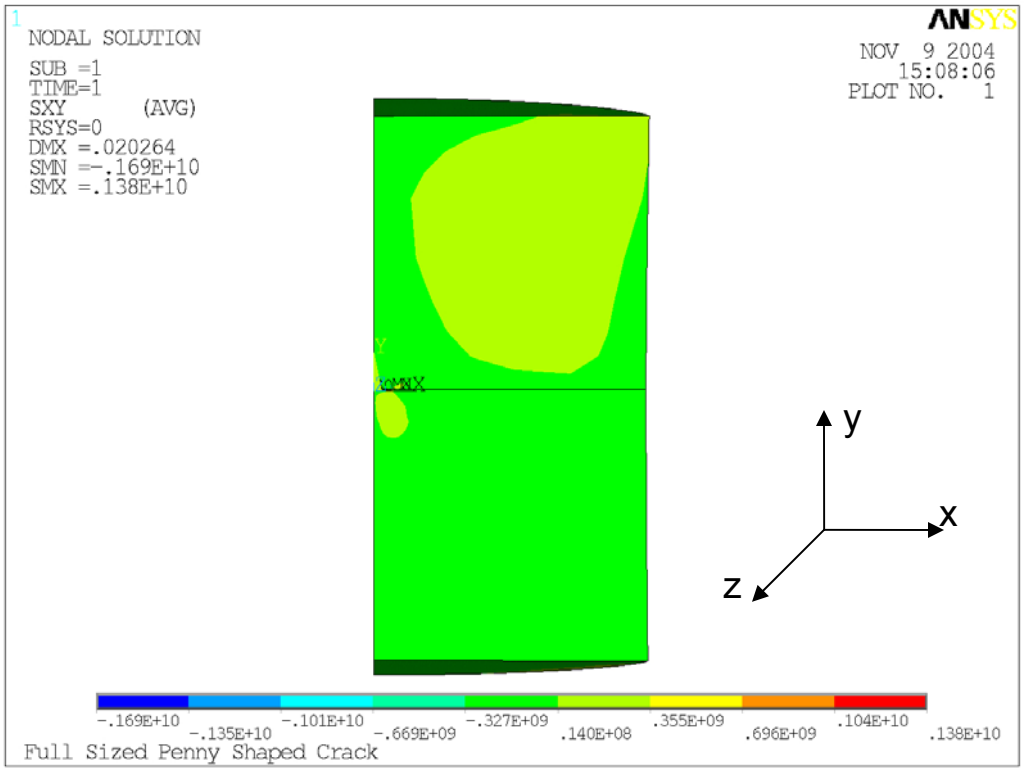

Figure C- 15: Sigma xy (MPa) of crack with parallel temperature gradient.

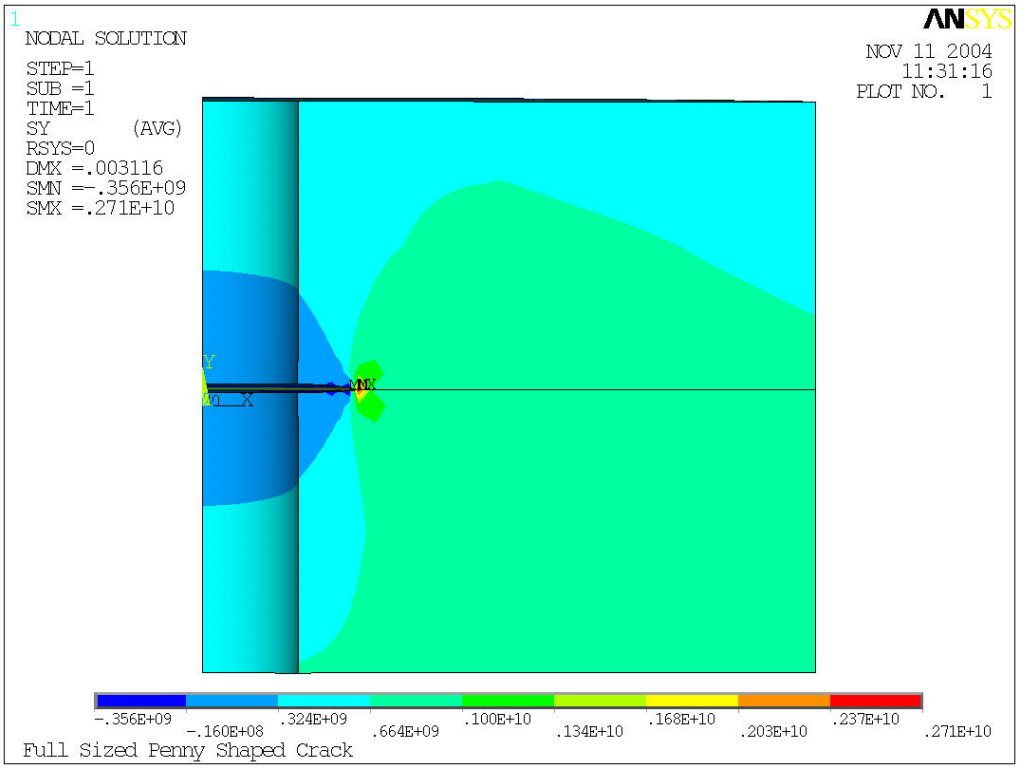

Figure C- 16: Sigma y (MPa) near the crack for a parallel temperature gradient.

REFERENCES

Anderson, T. L. (1995). Fracture Mechanics: Fundamentals and Applications, CRC Press.

Ansys (2003). Ansys 7.1 Documentaton.

Busso, E. P., Y. Tkach, et al. (2001). "Thermally induced failure of multilayer ceramic structures." Philosophical Magazine a-Physics of Condensed Matter Structure Defects and Mechanical Properties **81**(8): 1979-1995.

Busso, E. P., R. P. Travis, et al. (1998). Residual stress generation during constrained sintering of layers ceramic thin film structures. Mat. Res. Soc. Symp. Proc.

Cai, P. Z., D. J. Green, et al. (1997). "Constrained densification of alumina/zirconia hybrid laminates .1. Experimental observations of processing defects." Journal of the American Ceramic Society **80**(8): 1929-1939.

Chiu, C. C. and Y. Liou (1995). "Residual stresses and stress-induced cracks in coated components." Thin Solid Films **268**(1-2): 91-97.

Delorenzi, H. G. (1985). "Energy Release Rate Calculations by the Finite Element Method." Engineering Fracture Mechanics **21**(1): 129-143.

EG&G Services, P. I., Science Applications International (2000). Fuel Cell Handbook. Morgantown, West Virginia, US Department of Energy.

Evans, A. G., M. D. Drory, et al. (1988). "The Cracking and Decohesion of Thin-Films." Journal of Materials Research **3**(5): 1043-1049.

Gosz, M. a. M., B. (2002). "An interaction energy integral method for computation of mixed-mode stress intensity facotrs along non-planer crack fronts in three dimensions." Engineering Fracture Mechanics **69**: 299-319.

Gosz, M. D., J., and Moran, B. (1998). "Domain Integral Formulation for Stress Intensity Facotr Computation Along Curved Three-Dimensional Interface Cracks." International Journal of Solids and Structures **35**(15): 1763-1783.

He, M. Y., A. Bartlett, et al. (1991). "Kinking of a Crack out of an Interface - Role of Inplane Stress." Journal of the American Ceramic Society **74**(4): 767-771.

He, M. Y., A. G. Evans, et al. (1998). "Effects of morphology on the decohesion of compressed thin films." Materials Science and Engineering a-Structural Materials Properties Microstructure and Processing **245**(2): 168-181.

He, M. Y., C. H. Hsueh, et al. (2000). "Deflection versus penetration of a wedge-loaded crack: effects of branch-crack length and penetrated-layer width." Composites Part B-Engineering **31**(4): 299-308.

Hutchinson, J. W. and Z. Suo (1992). "Mixed-Mode Cracking in Layered Materials." Advances in Applied Mechanics, Vol 29 **29**: 63-191.

Kassir, M. K. and A. M. Bregman (1972). "Stress-Intensity Factor for a Penny-Shaped Crack between 2 Dissimilar Materials." Journal of Applied Mechanics **39**(1): 308-&.

Kumar, A. N. and B. F. Sorensen (2002). "Fracture energy and crack growth in surface treated Yttria stabilized Zirconia for SOFC applications." Materials Science and Engineering a-Structural Materials Properties Microstructure and Processing **333**(1-2): 380-389.

Li, F. Z. S., C.F.; Needleman, A. (1985). "A comparison of methods for calculating energy release rates." Engineering Fracture Mechanics **21**(2): 405-21.

Lowrie, F. L. a. R., R.D. (2000). "Room and high temperature failure mechanicsms in solid oxide fuel cell electrolytes." Journal of the European Ceramics Society **20**: 751-760.

Nahta, R. M., B. (1993). "Domain integrals for axisymmetric interface crack problems." International Journal of Solids and Structures **30**(15): 2027-40.

Nakamura, T. (1991). "Three-dimensional stress fields of elastic interface cracks." Transactions of the ASME. Journal of Applied Mechanics **58**(4): 939-46.

Recknagle, K. P., R. E. Williford, et al. (2003). "Three-dimensional thermo-fluid electrochemical modeling of planar SOFC stacks." Journal of Power Sources **113**(1): 109-114.

Rice, J. R. (1968). "A path independent integral and the approximate analysis of strain concentration by notches and cracks." Journal of Applied Mechanics **35**: 379-386.

Rice, J. R., Z. Suo, et al. (1990). Mechanics and thermodynamics of brittle interfacial failure in bimaterial systems. Metal-Ceramic Interfaces. M. Ruhle, A. G. Evans, M. F. Ashby and J. P. Hirth. New York, Pergamon Press**:** 269-294.

Selcuk, A. and A. Atkinson (1997). "Elastic properties of ceramic oxides used in solid oxide fuel cells (SOFC)." Journal of the European Ceramic Society **17**(12): 1523-1532.

Shigley, J. E. and C. R. Mischke (1989). Mechanical Engineering Design, McGraw-Hill inc.

Shih, C. F. and R. J. Asaro (1988). "Elastic-Plastic Analysis of Cracks on Bimaterial Interfaces .1. Small-Scale Yielding." Journal of Applied Mechanics-Transactions of the Asme **55**(2): 299-316.

Shih, C. F. M., B.; Nakamura, T. (1986). "Energy release rate along a three-dimensional crack front in a thermally stressed body." International Journal of Fracture **30**(2): 79-102.

Singhal, S. C. and K. Kendall (2002). High-temperature solid oxide fuel cells : fundamentals, design, and applicatons. New York, Elsevier Advanced Technology.

Sorensen, B. F. and S. Primdahl (1998). "Relationship between strength and failure mode of ceramic multilayers." Journal of Materials Science **33**(22): 5291-5300.

Tada, H., P. C. Paris, et al. (2000). The Stress Analysis of Cracks Handbook. New York, ASME Press.

Wilson, W. K. and I. W. Yu (1979). "Use of the J-Integral in Thermal-Stress Crack Problems." International Journal of Fracture **15**(4): 377-387.

Yakabe, H., Y. Baba, et al. (2001). X-Ray stress Measurements For Anode-Supported Planar SOFC. Electrochemical Society Proceedings.

Yakabe, H., Ogiwara, and Yasuda, I. (2001). 3D model calculation for the planar SOFC using multi-channel and stack models. Electrochemical Society Proceedings.

Yakabe, H., Ogiwara, T., Hishinuma, M. and Yasuda, I. (2001). "3-D model calculation for planar SOFC." Journal of Power Sources **102**: 144-154.